# BIFUNCTIONAL CATALYSIS OF SOME METAL CHALCOGENIDES IN HYDROGEN AND OXYGEN EVOLUTION REACTIONS

**THESIS SUBMITTED FOR THE DEGREE OF DOCTOR**

**OF PHILOSOPHY (SCIENCE)**

**OF**

**JADAVPUR UNIVERSITY**

**By**

**Mousumi Mondal**

**PHYSICAL CHEMISTRY SECTION**
**DEPARTMENT OF CHEMISTRY**
**JADAVPUR UNIVERSITY**
**KOLKATA -700032**
**INDIA**

**JULY 2024**

**Dr. Sujit Kumar Ghosh**
**Alexander-von-Humboldt Fellow**
**Associate Professor**
**Physical Chemistry Section**
**Department of Chemistry**
**Jadavpur University**
**Kolkata –700032, India**

**Telephone: 91 33 2457 2770 (Office)**
**+91 9475740794 (Mobile)**
**Facsimile : +91 33 2414 6223**
**E mail: skghosh.chemistry@jadavpuruniversity.in**

Date: 15th July, 2024

## CERTIFICATE FROM THE SUPERVISOR

This is to certify that the thesis entitled "**Bifunctional Catalysis of Some Metal Chalcogenides in Hydrogen and Oxygen Evolution Reactions**" Submitted by **Ms. Mousumi Mondal** who got her name registered on 27.08.2019 for the award of Ph. D. (Science) Degree of Jadavpur University, is absolutely based upon her own work under the supervision of **Dr. Sujit Kumar Ghosh** and that neither this thesis nor any part of it has been submitted for either any degree/diploma or any other academic award anywhere before.

(Signature of the Supervisor Date with Official Seal)

**Dr. SUJIT KUMAR GHOSH**
**Associate Professor**
**Department of Chemistry**
Jadavpur University
Kolkata-700032

**Index No:** 47/19/chem/26

## DECLARATION OF THE SCHOLAR

I, hereby, declare that the work presented in the thesis has been carried out by me, under the supervision of Dr. Sujit Kumar Ghosh, Associate Professor, Physical Chemistry Section, Department of Chemistry, Jadavpur University, Kolkata. Neither this thesis nor any part of it has been submitted for any degree/diploma or other academic award anywhere before.

Date: 15.07.2024

Mousumi Mondal

DEDICATD

TO MY

PARENTS

# ACKNOWLEDGEMENTS

The thesis entitled is my research work under the guidance of Dr. Sujit Kumar Ghosh, Physical Chemistry Section, Department of Chemistry, Jadavpur University, Kolkata.

I, express my regard and gratitude to Prof. Swapan Kumar Bhattacharya for his guidance, inspiration and constant encouragement throughout my whole research work.

I would like to express my gratitude to Prof. Arup Gayen, In-Charge, Physical Chemistry Section, Department of Chemistry, Prof. Ambikesh Mahapatra, Dr. Asamanjoy Bhunia, Dr. Rituparna Mondal for their constant inspiration and providing instrumental facilities to carry out the research works.

I would like to thank Dr. Kamal Kanti Bera, Anirban Ghosh, Arijit Maity, Abhimanyu Sarkar and other scholars of the Department of Chemistry for their valuable help and constant support during my work.

I am grateful to the Department of Chemistry, Jadavpur University for provide me necessary infrastructural facilities. I would like to thank Dean of the Faculty of Science, Head of the Department of Chemistry for providing me labortary facilities during my research works.

I would like to express my gratitude to my father Sukumar Mondal, mother Rita Mondal and my brother Supriyo Mondal for their inspiration and support.

Mousumi Mondal

# CONTENTS

Page No.

## ABSTRACT

## Introduction

1.1. General background……………………………………………………..1-5
  1.1.1. Oxygen evolution reaction (OER)……………………………………2-4
  1.1.2. Hydrogenevlution reaction (HER)......................................................4-5
1.2. Applications of water splitting reaction…………………………………5-6
1.3. Types of water splitting reactions………………………………………..7-8
  1.3.1. Photocatalytic water splitting…………………………………………...7
  1.3.2. Electrocatalytic water splitting………………………………………7-8
  1.3.3. Photoelectrocatalytic water splitting……………………………………8
1.4. Literature review…………………………………………………….8-12
1.5. Objectives of the present work………………………………………..12-13
1.6. Transition metals……………………………………………………13-14
1.7. Heterogeneous catalysts……………………………………………14-15
1.8. Photocatalysts………………………………………………………..15
1.9. Scope and objectives………………………………………………..16-17
  1.9.1. Choice of medium……………………………………………………...16
  1.9.2. Choice of catalysts…………………………………………………16-17
1.10. Characterization techniques………………………………………......17-22
  1.10.1. X-ray diffraction (XRD)……………………………………………...17-18
  1.10.2. Fourier transform infrared (FTIR) spectroscopy……………..……18-19
  1.10.3. Scanning electron microscopy (SEM)……………………………..19-20
  1.10.4. Transmission electron microscopy (TEM)………………………...20-21
  1.10.5. Energy-dispersive X-ray spectroscopy (EDX)……………………...21
  1.10.6. X-ray photoelectron spectroscopy (XPS)………………………….21-22
1.11. Techniques employed for electrocatalytic study………………………22-24
  1.11.1. Potentiodynamic technique: Cyclic voltammetry (CV)…………….22-23
  1.11.2. Linear sweep voltammetry (LSV)……………………………………..23
  1.11.3. Controlled current technique: Chronoamperometry (CA)…………23-24
1.12. Parameters for the evaluation of electrochemical water splitting……...24-31
  1.12.1. Overpotential……………………………………………………24-25

1.12.2. Concentration overpotential……………………………………………25
1.12.3. Turnover frequency (TOF)…………………………………………25-27
1.12.4. Electrochemical active surface area (ECSA)………………………….27
1.12.5. Electrochemical impedence spectroscopy (EIS)…………………...27-29
1.12.6. Butler-Volmer equation…………………………………………….29-31
1.12.7. Stability………………………………………………………………...31
1.13. References………………………………………………………………..31-45

## CHAPTER 1

## Bifunctional catalysis on water splitting reaction by graphitic carbon supported NiO, NiS and NiSe nanoparticles

2.1. Introduction………………………………………………………….......49-50
2.2. Experimental……………………………………………………………50-52
2.2.1. Reagents and instruments………………………………………………50
2.2.2. Syntheses of NiO, NiS and NiSe nanoparticles……………………..50-51
2.2.3. Electrochemical measurements…………………………………….51-52
2.3.Results and discussion……………………………………………………...52-65
2.3.1. Structural characterization………………………………………….52-56
2.3.2. Electrochemical studies…………………………………………….56-65
2.4. Conclusions……………………………………………………………………65
References…………………………………………………………….65-73

## CHAPTER 2

## Superiority of CuSe as a non-noble electrocatalyst among copper chalcogens for overall water splitting reactions

3.1. Introduction………………………………………………………….......77-78
3.2. Experimental section……………………………………………………78-79
3.2.1. Chemicals…………………………………………………………………...78
3.2.2. Synthesis of copper oxide, sulphide and selenid nanoparticles…………78

3.2.3. Structure characterization……………………………………………..78-79
3.2.4. Electrochemical characterization………………………………………79
3.3. Results and discussion……………………………………………………......80-91
3.3.1. XRD analysis………………………………………………………80-81
3.3.2. FTIR analysis………………………………………………………81-82
3.3.3. FESEM and TEM analysis…………………………………………83
3.3.4. XPS analysis…………………………………………………………..84
3.4. Electrochemical results…………………………………………......85-91
3.5.Conclusions…………………………………………………………………..91-92
References……………………………………………………………………92-96

## CHAPTER 3

## Water splitting reaction on nickel sulphide, molebdenium sulphide, nickel molybdenium sulphide electrocatalysts

4.1. Introduction………………………………………………………………99-100
4.2. Experimental section……………………………………………………………100
4.2.1. Material…………………………………………………………………100
4.2.2. Synthesis……………………………………………………………...100
4.2.3. Characterization of materials…………………………………………100
4.2.4. Electrochemical performance……………………………………100-101
4.3.Results and discussion…………………………………………………...102-111
4.3.1. XRD analysis……………………………………………………102-103
4.3.2. SEM analysis…………………………………………………………103
4.3.3. TEM analysis…………………………………………………………104
4.3.4. XPS analysis…………………………………………………..104-105
4.3.5. Electrochemical studies…………………………………………105-111
4.4. Conclusions……………………………………………………………………..111
4.5. References……………………………………………………………112-115

## CHAPTER 4

## Hydrothermally synthesized nickel selenide, molybdenium diselenide and nickel molybdenium selenide as cost effective and bifunctional electrocatalysts for water splitting reaction

5.1. Introduction……………………………………………………………………..119
5.2. Experimental section…………………………………………………………...119
  5.2.1. Reagents……………………………………………………………119-120
  5.2.2. Instrumentation……………………………………………………………120
  5.2.3. Synthesis of the electrocatalysts……………………………………..120
5.3.Characterization of the materials……………………………………………120
  5.3.1. Electrochemical performance…………………………………………120
5.4. Results and discussion…………………………………………………..121-132
  5.4.1. Structural characterization……………………………………….121-126
  5.4.2. Electrochemical studies…………………………………………….126-132
5.5.Conclusions………………………………………………………………………...132
  References……………………………………………………………………132-139

Conclusions……………………………………………………………………………...140

Future aspects…………………………………………………………………………...141

# ABSTRACT

**Index No: 47/19/chem/26**

## Title: BIFUNCTIONAL CATALYSIS OF SOME METAL CHALCOGENIDES IN HYDROGEN AND OXYGEN EVOLUTION REACTIONS

### Submitted by: Mousumi Mondal

In the vanguard of the 21st century, the quest for renewable and eco-friendly energy sources stands as a paramount scientific and technological endeavor. The escalating energy deficit and ecological ramifications stemming from the heightened reliance on and depletion of conventional fossil fuels have catalyzed the advancement of innovative energy transmutation technologies, including electrocatalysis and photocatalysis, alongside energy retention mechanisms such as supercapacitors and batteries.

Hydrogen, hailed as the fuel of tomorrow, boasts a superior gravimetric energy quotient of 120 MJ $kg^{-1}$ eclipsing that of gasoline at 44 MJ $kg^{-1}$ in addition to unmatched energy transformation proficiency, ecological harmony, and the virtue of emitting solely water as a byproduct, thus ensuring zero carbon dioxide release. Furthermore, the application spectrum of hydrogen extends to the production of ammonia via the Haber process, methanol creation, the hydrocracking of crude oil, hydrochloric acid manufacturing, and the hydrogenation of oils and fats. Given the absence of naturally occurring hydrogen on our planet, its current production predominantly transpires through the steam reforming of hydrocarbons under elevated temperatures and pressures. This process not only consumes our finite fossil fuel reserves but also contributes to carbon dioxide emissions. Additionally, the hydrogen procured through this method is often tainted with oxides of carbon, nitrogen, and sulfur, which detrimentally affect the surface of the catalysts and diminish its lifespan. Hydrogen, as the exemplary sustainable energy vector, that is distinguished by environmental congeniality, high energy density, and efficient conversion capabilities. It is anticipated to facilitate the seamless integration of diverse energy networks, and thereby fulfilling the fundamental energy requisites of the future.

The pursuit of pristine and inexhaustible energy reserves is a cornerstone of modern scientific innovation. Electrochemical water splitting, energized by sustainable power sources like solar, wind, and hydroelectricity, stands as a beacon of hope for the generation of high-fidelity hydrogen ($H_2$). This technique, colloquially termed as “water splitting”, has garnered significant attention over the previous decade as a captivating solution to transmute renewable electric currents into a reservoir of chemical energy. This energy is encapsulated in the form of hydrogen and oxygen, harvested at the anode and cathode of the apparatus, respectively. There has been a burgeoning advancement in this sector of energy capture technology.

Harnessing solar energy through nanoparticulate photocatalysts for the photocatalytic division of water is at the forefront of sustainable, low-carbon hydrogen ($H_2$) production. This process, a non-spontaneous chemical reaction, necessitates the transfer of four electrons from a minimum of two water molecules to facilitate the oxidation of water into oxygen ($O_2$). The theoretical threshold energy to spark this reaction stands at 1.23 eV. Yet, the evolution of $O_2$ from water is marred by slow kinetics and substantial

kinetic overpotentials, necessitating the use of sacrificial agents to donate electrons for efficient photocatalytic $H_2$ generation. Notably, the oxygen evolution reaction (OER) suffers from overpotential losses up to 30%, leading to considerable energy dissipation. Moreover, the absence of efficient techniques to segregate the resultant $O_2$ and $H_2$ gases poses a significant hurdle for the practical deployment of photocatalytic water splitting. These impediments have shifted the focus towards novel alternatives to the OER, which promise to bolster the burgeoning global hydrogen economy.

The process of overall water splitting reaction can be characterized by two different half-cell reactions at two different electrodes: at cathode, the hydrogen evolution reaction (HER) and at anode, the oxygen evolution reaction (OER). The thermodynamic potential for this process is ~1.23 V that is equivalent to the minimum energy requirement of the process, $\Delta G=237.1$ kJ/mol under standard conditions. The anodic OER is notably more complex than the HER, involving four synchronized proton-electron transfer steps and the generation of various oxygenated intermediates, such as HO*, O*, and HOO*. This complexity accounts for approximately 80% of the total energy consumption in the water electrolyzer. Furthermore, despite significant progress and innovations in crafting high-efficiency OER electrocatalysts, the journey towards optimal performance continues. In this study cost-effective non noble metal-based catalysts, nanoparticles of some transitional metal chalcogenides like CuSe, CuS, NiS, NiSe, etc. are synthesized by similar hydrothermal methods, characterized and their electro catalytic performances are compared and analyzed by varying the chalcogens, e. g., oxygen, sulphur, and selenium. The synthesized metal nanoparticles have been characterized by microscopic (FE-SEM, HR-TEM), X-ray photoelectron spectroscopy (XPS), X-ray diffraction (XRD), Energy dispersive X-ray spectroscopy (EDX), cyclic voltammetry and chronoamperometry techniques. The study provides a comparison on the effects of various transition metals regarding the catalytic activity of the corresponding chalcogenides and composites. In addition, it may help to get the better catalyst for synthesis of green energy source, hydrogen and understanding the mechanism of the reactions.

To surmount the prevailing challenges, a triad of strategies is commonly employed to enhance the electrochemical efficacy of catalysts. Initially, the fundamental reactivity of the active sites of the catalysts can be markedly augmented through diverse electronic structure optimization techniques, encompassing strategies like doping with cations or anions, defect engineering, manipulation of crystal phases and facets, as well as the alteration of surface strain. Subsequently, the accessibility of these active sites can be significantly expanded through innovative designs in catalyst morphology. Lastly, the proficiency of charge transfer can be elevated by the strategic deposition of catalysts onto structured conductive supports. In this scenario, the vanguard of advanced materials is poised to revolutionize the electrocatalyst design landscape, paving the way for effective and durable water splitting methodologies.

# INTRODUCTION

## 1.1. General background

Electrochemical water splitting, propelled by electric power derived from renewable resources, emerges as an exemplary method for the eco-conscious production of hydrogen ($H_2$). This process is distinguished by its singular by product oxygen ($O_2$) and the notable absence of carbon emissions throughout its entirety. This discourse sheds light on the scientific hurdles that currently impede the progress of hybrid water electrolysis methods, with the aspiration of sparking continued ingenuity within this swiftly evolving domain. Photocatalysis, propelled by light, orchestrates oxidation-reduction reactions via generation of electrons and holes upon interaction with electromagnetic radiation. The photocatalytic water splitting can occur under the condition that the minimum of the conduction band should be more negative compared to the corresponding reduction potential for the conversion of $H^+$ to $H_2$ and the maximum of the valence band should overcome the oxidation potential for the conversion of $H_2O$ to $O_2$.

The electrolytic cell was first projected in 1789 and collected of three parts: cathode, anode and an electrolyte [1]. The reaction involved in electrochemical water splitting reaction,

$$H_2O\ (l) \rightarrow H_2\ (g) + 1/2O_2\ (g) \qquad (1.1)$$

$\Delta G_0 = +237.32\ \text{kJ mol}^{-1}$, $\Delta E_0 = 1.23\ V$ *vs.* RHE.

Two half-cell reactions–oxidation and reduction–is associated with the process of overall water splitting reaction. The reduction of protons at the cathode can be assigned as the hydrogen evolution reaction (HER)

$$2H^+\ (aq) + 2e^- \rightarrow H_2\ (g) \qquad (1.2)$$

and oxygen evolution reaction (OER) is oxidation of water [2].

$$2H_2O\ (l) \rightarrow O_2\ (g) + 4H^+\ (aq) + 4e^- \qquad (1.3)$$

Molecular water is extremely stable and bears a low conductivity. To increase the conductivity, electrolytes, such as sulphuric acid, sodium hydroxide, potassium hydroxide, and potassium phosphate buffers can be added, resulting in an acidic, basic, and neutral medium [3–4].

In acidic medium [5],

$$\text{Cathode: } 4H^+ + 4e^- \rightarrow 2H_2,\ E° = 0.0\ V \tag{1.4}$$

$$\text{Anode: } 2H_2O \rightarrow O_2 + 4H^+ + 4e^-,\ E° = +1.23\ V \tag{1.5}$$

In basic medium,

$$\text{Cathode: } 4H_2O + 4e^- \rightarrow 2H_2 + 4OH^-,\ E° = -0.828\ V \tag{1.6}$$

$$\text{Anode: } 4OH^- \rightarrow O_2 + 2H_2O + 4e^-,\ E° = +0.401\ V \tag{1.7}$$

In neutral medium,

$$\text{Cathode: } 4H_2O + 4e^- \rightarrow 2H_2 + 4OH^-,\ E° = +0.413\ V \tag{1.8}$$

$$\text{Anode: } 2H_2O \rightarrow O_2 + 4H^+ + 4e^-,\ E° = +0.817\ V \tag{1.9}$$

### *1.1.1. Oxygen evolution reaction (OER)*

While the hydroxyl ions in the alkaline or neutral electrolyte are oxidized into oxygen and water, the $H_2O$ in the acidic electrolyte is prone to be oxidized to hydrogen and oxygen. The oxygen evolution reactioncan be catalyzed more effectively by transition metal-based catalysts, such as iron (Fe), nickel (Ni), and cobalt (Co), in alkaline media [6–7]. However, in both basic and acidic environments, catalysts based on Fe and Ru have been demonstrated to exhibit increased efficiency in OER processes. Matsumoto and Sato [8] summarized the process in detail in 1986. This study covered the well-known electrochemical oxide pathway as well as the pathways proposed by Yeager and Wade, KrasilShchkov, Bockris [9], and Hackerman [10] pathways. All the proposed mechanisms in the basic medium begin with the coordination of hydroxide ions to active sites as the elementary step that follows through a series of stages. Because of the kinetic barriers at different stages of the reaction mechanism, the overpotential becomes higher [11].

**OER in alkaline media**

**1. Electrochemical oxide path**

$$* + OH^- \rightarrow *OH + e^- \tag{1.10}$$

$$*OH + OH^-(aq) \rightarrow *O + H_2O + e^- \tag{1.11}$$

$$2*O \rightarrow 2* + O_2\,(g) \tag{1.12}$$

**2. Oxide path**

$$* + OH^-(aq) \rightarrow *OH + e^- \tag{1.13}$$

$$2{*}OH \rightarrow {*}O + {*} + H_2O \tag{1.14}$$

$$2{*}O \rightarrow 2{*} + O_2\,(g) \tag{1.15}$$

### 3. Krasil’shchkov path

$${*} + OH^{-}\,(aq) \rightarrow {*}OH + e^{-} \tag{1.16}$$

$${*}OH + OH^{-}(aq) \rightarrow {*}O^{-} + H_2O \tag{1.17}$$

$${*}O^{-} \rightarrow {*}O + e^{-} \tag{1.18}$$

$${*}O + {*}O \rightarrow 2{*} + O_2\,(g) \tag{1.19}$$

### 4. Yeager path

$${*} + OH^{-}(aq) \rightarrow {*}OH + e^{-} \tag{1.20}$$

$${*}^{z}OH \rightarrow {*}^{z+1}OH^{-} + {*} + e^{-} \tag{1.21}$$

$$2^{*z+1}OH + 2OH^{-}(aq) \rightarrow 2{*} + 2H_2O + O_2\,(g) \tag{1.22}$$

### 5. Bockris path

$${*} + OH\,(aq) \rightarrow {*}OH + e^{-} \tag{1.23}$$

$${*}OH + OH^{-}\,(aq) \rightarrow {*}H_2O_2 + e^{-} \tag{1.24}$$

$${*}H_2O_2 + OH^{-}\,(aq) \rightarrow {*}OOH^{-} + H_2O \tag{1.25}$$

$${*}H_2O_2 + {*}OOH^{-} \rightarrow 2{*} + OH^{-}\,(aq) + O_2\,(g) \tag{1.26}$$

### OER in acidic media

### 1. Electrochemical oxide path

$${*} + H_2O \rightarrow {*}OH + H^{+} + e^{-} \tag{1.27}$$

$${*}OH \rightarrow {*}O + H^{+} + e^{-} \tag{1.28}$$

$${*}O + H_2O \rightarrow OOH{*} + H^{+} + e^{-} \tag{1.29}$$

$${*}O_2 \rightarrow {*} + O_2 \tag{1.30}$$

### 2. Oxide path

$${*} + H_2O \rightarrow {*}OH + H^{+}\,(aq) + e^{-} \tag{1.31}$$

$$2{*}OH \rightarrow {*}O + {*} + H_2O \tag{1.32}$$

$$2{*}O \rightarrow 2{*} + O_2\,(g) \tag{1.33}$$

### 3. Krasil'shchkov path

$${*} + H_2O \rightarrow {*}OH + H^{+}\,(aq) + e^{-} \tag{1.34}$$

$$*OH \rightarrow S–O^{-} + H^{+} (aq) \quad (1.35)$$

$$*O^{-} \rightarrow *O + e^{-} \quad (1.36)$$

$$2*O \rightarrow 2* + O_2 (g) \quad (1.37)$$

### 4. Wade and Hackerman path

$$2* + 2H_2O \rightarrow *O + *H_2O + 2H^{+} (aq) + 2e^{-} \quad (1.38)$$

$$*O + 2*OH \rightarrow *H_2O + 2* + O_2 (g) + 2e^{-} \quad (1.39)$$

These are the potential OER processes; the mechanism acts as the rate-determining step, and the synthesis of intermediates, O*, OH*, and OOH* on the electrocatalyst surface is a prerequisite [12].

### *1.1.2. Hydrogen evlution reaction (HER)*

The first stage in the multistep hydrogen evolution reaction is the protons being discharged and the hydrogen being adsorbed on the electrode surface that has been assigned as the Volmer. The desorption of $H_2$ ions from the cathode via an electrochemical pathway (Heyrovsky step) or a chemical method (Tafel step) is the second stage of the reaction mechanism [13–16].

**HER in alkaline media**

$$H_2O + e^{-} \rightarrow H* + OH^{-} \text{(Volmer)} \quad (1.40)$$

$$H_2O + e^{-} \rightarrow H_2 + OH^{-} \text{(Heyrovsky)} \quad (1.41)$$

$$\text{(or) } 2H* \rightarrow H_2 \text{(Tafel)} \quad (1.42)$$

**HER in acidic media**

$$H^{+} + e^{-} \rightarrow H* \text{ (Volmer)} \quad (1.43)$$

$$H^{+} + e^{-} + H* \rightarrow H_2 \text{(Heyrovsky)} \quad (1.44)$$

$$\text{(or) } 2H* \rightarrow H_2 \text{(Tafel)} \quad (1.45)$$

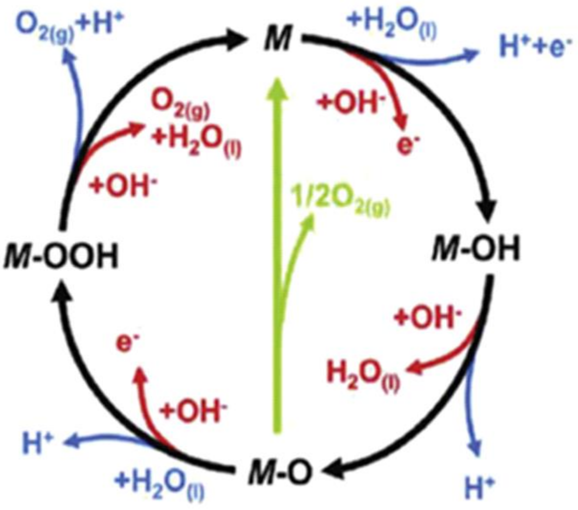

**Fig. 1.1.** Schematic presentation of oxygen evolution reaction in acidic and alkaline electrolytes

The oxygen evolution reaction in alkaline (blue line) and in acidic (blue line) electrolytes is predicted by the processes as has been shown in Fig. 1.1. The two plausible intermediates, M–OOH and M–O, are shown by the ensuing black and green lines.

## 1.2. Applications of water splitting reaction

In many technological applications, such as solar energy production and catalytic fuel cells, water splitting is an essential process. This procedure makes it possible to directly decompose water and produce hydrogen. The energy required to cleave hydrogen bonds can be supplied from a variety of sources, including light, electricity, and heat. Coal gasification and natural gas replication are the foundations of industrial hydrogen production. However, these procedures need a lot of energy [1–10]. Electrical current when passed over water causes electrolytic water splitting. At the electrode-solution interface, charge transfer reactions within a unit cell, referred to as an electrolyser, transform electrical energy into chemical energy [11–18]. In industrial applications, less energy-intensive and more sustainable technologies seem to be extremely appealing for utilizing renewable feedstocks (biomass, water, and alcohols) and renewable primary energy sources (sunlight, wind, wave, and hydropower). The development of novel technologies based on non-fossil based pathways for the production of hydrogen is at varying stages of upgradation. However, every process has its own advantages, difficulties, and possibilities [18–20].

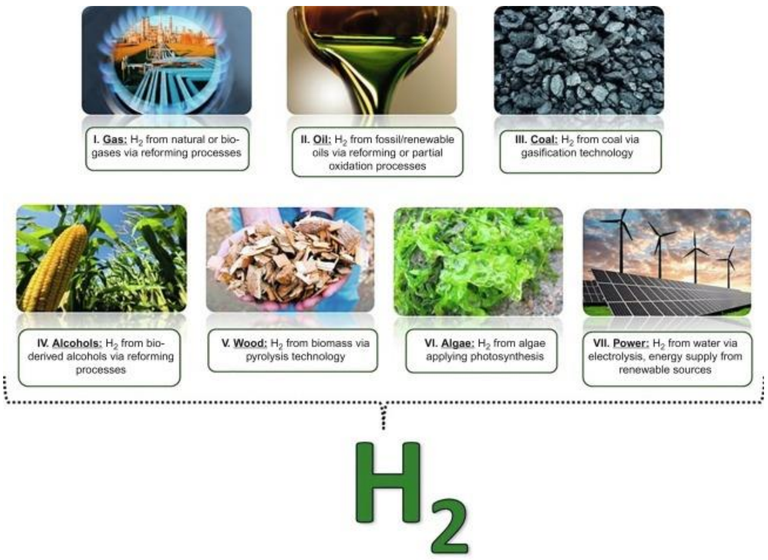

**Fig. 1.2.** An overview of the several feedstocks and process options for producing $H_2$. This text was adapted from Hydrogen Production and Storage; R&D Priorities and Gaps, OECD/IEA, Paris 2006 by T. Riis, E. F. Hagen, J. S. Vie, P. J. S. Vie, Ø. Ulleberg, and G. Sandrock.

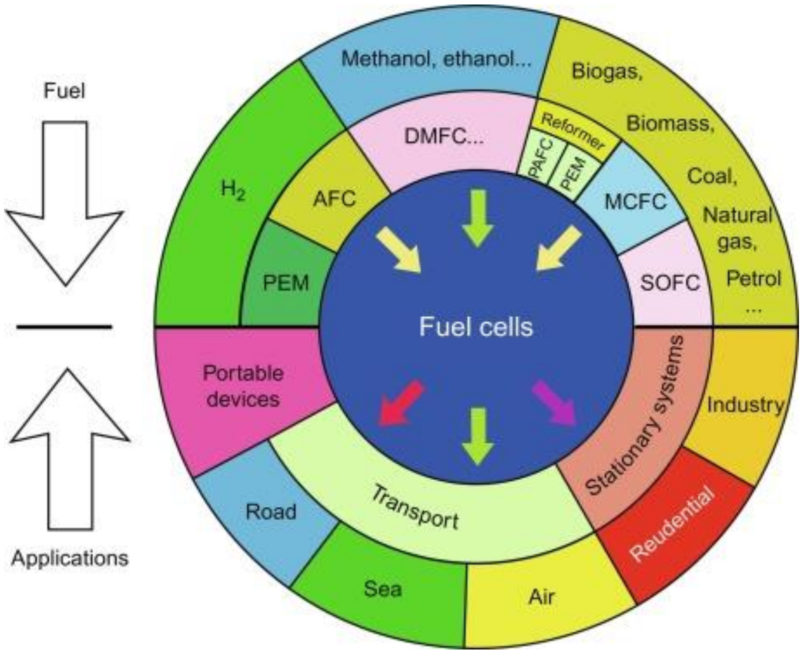

**Fig. 1.1**. Lower segment: main application of the fuel cell technology; Upper segment: fuel and fuel cell types. AFC, alkaline (especially in the space sector); DMFC, direct membrane; MCFC, molten carbonate; PAFC, phosphoric acid; PEMFC, polymer exchange membrane; SOFC, solid oxide.

## 1.3. Types of water splitting reactions

Numerous methods, including photocatalytic, electrocatalytic and photoelectrocatalytic, can be used to carry out a water splitting reaction.

**1.3.1.** ***Photocatalytic water splitting:*** The process of water splitting reaction is driven by the generation of excitons upon absorption of photons. Over this process, the bandgap of the materials under consideration is crucial. The energy of the incident photon energy is dependent on the choice of materials. A band gap greater than 3.0 eV becomes necessary when excited with ultraviolet radiation. Photocatalysts that possess a bandgap of 1.23 eV, which is greater than the free energy of water splitting reaction can be considered as ideal. The choice of photocatalysts is limited by the conditions that the energy of valence and conduction bands should be lower than the potential for water oxidation, greater than the potential for hydrogen reduction, and inherit a low rate of electron-hole pair recombination. By reducing charge recombination to increase the amount of visible light under experimental conditions, carbon-based nanomaterials, such as carbon nanotubes, carbon quantum dots, graphene and graphitic-carbon nitride have been used that can improve the performance of photocatalytic water splitting reaction [21–22].

**1.3.2**. ***Electrocatalytic water splitting:*** Another way to split water is an electrochemical approach by using an electrocatalysts in the process. In electrocatalytic water splitting reaction, hydrogen evolution reaction occurs at the cathode and oxygen evolution reaction occursat the anode. Under the benchmarked circumstances, the energy needed for the reaction of water splitting is 237 kJ mol$^{-1}$. In this process, for the transfer of electrons, a potential of ~1.23 V potential is indispensable [23].

**Total reaction:** $H_2 + O_2 \rightarrow H_2O$ (1.46)

In acidic medium,

**Cathode:** $2H^+ + 2e^- \rightarrow H_2$ (1.47)

**Anode:** $H_2O \rightarrow 2H^+ + 12O_2 + 2e^-$ (1.48)

In alkaline medium,

**Cathode:** $2H_2O + 2e^- \rightarrow H_2 + 2OH^-$ (1.49)

**Anode:** $2OH^- \rightarrow H_2O + 12O_2 + 2e^-$ (1.50)

The three phases of the HER method-the Volmer type reaction (hydrogen adsorption reaction), the Heyrovsky type reaction (electrochemical hydrogen desorption reaction), and the Tafel type reaction (chemical desorption reaction)-can be applied to both acidic and alkaline conditions [24].

**1.3.3.** ***Photoelectrocatalytic water splitting:*** The process of water splitting can also be performed using a combination of photocatalytic and electrocatalytic processes. A conducting electrode is coated with the samples in the photoelectrocatalytic water splitting reaction. This approach that is associated with the presence of light, the applied potential can lead to the occurance of the hydrogen evolution reaction. However, if the electrodes are suitably modified, the needed potential to be applied becomes shifted to lower levels. The anode receives the photogenerated holes, which oxidize the $OH^-$. In this process, since the two electrodes, or reaction sites, are separated spatially and therefore, the products as hydrogen and oxygen can be collected separately [25].

## 1.4. Literature review

In the issue of performing electrochemical reactions, electrocatalysts play a vital role. The composition of the created electrocatalysts Ruthenium oxide and platinum are optimum for oxygen and hydrogen evolution reactions. Some improvements are needed to address cost-effectiveness issues of the catalysts. Therefore, the production of inexpensive, highly active, stable electrocatalysts is being given top priority in research efforts to execute water splitting processes.

Researchers have developed a novel molecular HER electrocatalysts based on a molybdenum selenium clusters **(**$Mo_3Se_{13}$) [26–30]. Precisely substituting the sulphur molecule at the molecular level, these particles can improve the HER activity [31–36]. The dispersion of microflowers through drop casting method comprised of interconnected **NiO nanowalls** decorated with very small amount of **platinum nanoparticles** onto graphene paper offers cost-effective approach for the development of HER electrodes [37–42]. The composite electrodes, under alkaline conditions, exhibits an overpotential of **66 mV** when the current density is at **10 mA cm$^{-2}$** and lower Tafel slope of nearly **82 mV dec$^{-1}$** and the high turnover frequency as 2.07 s$^{-1}$ corresponding to Pt loading of **11.2 mg cm$^{-2}$** [43–45]. Furthermore, researchers explored the characteristic values of **ruthenium (Ru)-based oxygen evolutionreaction (OER)** catalysts, including the OER mechanism, intrinsic activity, and stability issues. By introducing strain through laser ablation in liquid, the grain boundaries have been generated in Ru OER catalysts, resulting in significantly lower overpotential **(202 mV**) for the OER in acidic media compared to commercial $RuO_2$ **(302 mV**). In the **$Ni_xSe_y$** system, nickel plays a vital role as the main catalytic activity site. Its unique valence electron configuration (**$3d^8 4s^2$)** contributes to its effectiveness as an OER catalyst. In comparison with the same group elements like oxygen (O) and sulfur (S), selenium (Se) possesses same number of valence electrons and the oxidation number and exhibit inherent metal properties that render to exhibit better electrical conductivity and the electrocatalytic activity [46–47].

Researchers have also identified promising electrocatalysts to enhance hydrogen and oxygen evolution reactions. First, **1T′-$MoS_2$** has been emerged to act as viable substitutes for platinum as electrocatalysts towards hydrogen evolution reaction. These materials are advantageous as these possess low charge transfer resistance, low overpotential, and impressive durability, achieving an efficiency of **75%** at **$1.0\ A\ cm^{-2}$** and **1.94 V**. Second, novel NiMo-based nanorods synthesized via thermal ammonolysis exhibit extraordinary performance for both the OER and HER. These materials can achieve small overpotentials of **252 mV** and **103 mV** to attain a current density of **$10\ mA\ cm^{-2}$** in **1.0 M KOH solution.** Lastly, when the metals are doped in two-dimensional nanomaterials, specifically $MoS_2$ and NiMoS, deposited onto the free-standing graphene paper, serves as effective counter electrodes in quasi solid-state at a dye-sensitized solar cells, benefiting from high electrical conductivity and electrocatalytic activity [48–51].

Copper (Cu) plays a vital role in living systems, where maintaining an optimum copper level is essential. Deviations from this balance can lead to metabolic disturbances and unhealthy conditions. Researchers have extensively studied the impact of copper on cellular cycles, emphasizing its significance as a redox-active transition metal. Meanwhile, hydrogen ($H_2$) holds immense promise as an energy transporter for the future. $H_2$ production through water splitting offers a renewable and clean energy option. Since, we seek sustainable replacement of conventional fossil fuels, efficient and abundant catalysts become crucial for enhancing the water splitting process. Although Cu-based materials exhibit high conductivity and abundant reserves, they have not received as much research attention for electrode designs compared to Fe/Co/Ni-based compounds. Recent progress has focused on Cu foam-derived materials, leveraging their three-dimensional network structures [52–53]. These materials demonstrate efficiency in both pure water electrolysis and hybrid water electrolysis. The advantages of Cu foam-derived materials include structural porosity, low cost, and operational durability [54–55].

The sharp edges of the molybdenum sulfide catalysts, the crystalline phase of $MoS_2$ and amorphous phase of $MoS_x$ structure, and the molecular clusters, play a pivotal role in water splitting. These catalysts share similar active sites and turnover frequencies, emphasizing that total electrode activity of primarily hinges on the number of nearby active sites for each geometric electrode area. Researchers have also explored metal phosphates, such as Co-phosphate (CoPO), Ni-phosphate (NiPO), and Ni-Co-phosphate (NiCoPO), synthesized without structure-directing agents. These materials exhibit high surface area, good interparticle porosity, and transition metals within their frameworks, making them promising candidates for electrocatalytic OER. As an alternative to the platinum (Pt), noble-metal-free electrocatalysts are gaining attraction, with novel preparation methods in focus. In addition, a NiMoSe/NF-2 heteronanostructures at the interface can be synthesized by annealing a hybrid of the crystalline NiSe and the amorphous $MoSe_x$ (NiMoSe/NF-1) [56–57]. This structure exhibited superior performance in both HER and OER mechanism, with lower overpotentials and favorable Tafel slopes. Lastly, the combination of nickel selenide molecules with molybdenum-based materials accelerates reaction rates for both electrodes, leveraging unique electron configuration of metal nickel and the significant reactivity of molybdenum for proton desorption [58–59].

**Gibbs free energy and Sabatier principle:** In accordance with the Sabatier principle, the optimal Gibbs free energy for different for intermediates in the process of HER is 0 eV. For the efficient hydrogen adsorption-desorption processes, the attainment of right balance in Gibbs free energy is obvious. Molybdenum at the +4-valence state, exhibits excellent ability of hydrogen desorption but limits the dissociation of water during the entire course of the Volmer step [60].

**Alkaline media and strong H-OH covalent bonds:** The splitting of the strong H–OH covalent bond with high energy barrier becomes the ratedetermining step under alkalike conditions for hydrogen evolution reaction. Nanosheets of 1T-$MoSe_2$ have been anchored on NiSe nanowires to fabricate 1T-$MoSe_2$/NiSe heterostructuresthat exhibit remarkable properties towards the electrocatalytic dissociation of water. The Se sulfides are electrochemically grown on fluorine-doped tin oxide substrates, serve as highly active and stable in the HER electrocatalysts. Among them, $Ni_{0.96}Mo_{0.04}S$ stands out exhibiting capable to HER activity with the lowest Tafel slope, the value of slope is 46 mV dec$^{-1}$. The HER activity of Ni containing binary alloys follows the sequence: Ni-Mo > Ni-Zn > Ni-Co > Ni-W > Ni-Fe > Ni-Cr. Synthesis of the heterogeneous catalysts containing Ni-Mo alloy is also important. Such a catalyst optimizes the interface between the metal and metal oxide or hydroxide, effectively lowering the dissociation kinetic energy barrier. Non-metallic elements (e. g., carbon, nitrogen, sulphur, oxygen, phosporus, boron, etc.) can exist exploration for incorporation into nickel molybdenium system. These elements change the free energy of adsorption of the produced intermediates and support for fast water dissociation. While platinum remains for the best electrocatalysts with a $\Delta G^{\#}*$ value of -0.09 eV (i. e., -0.33 eV of $\Delta E^{\#}$), Ni forms the strong hydrogen bonds with a $\Delta G^{\#}*$ value of -0.27 eV (i. e., -0.51 eV of $\Delta E^{\#}$). The weak desorption capability of the $OH^-$ species on nickel surfaces leads to essential irreversible reactions and water dissociation by formation of the oxides and hydroxide phases [61].

**Electrochemical impedance spectroscopy and slow electron transport:** Electrochemical impedance spectroscopy has revealed the slow movement of electrons in the hydrogen evolution reaction in the presence of unstructured molybdenum sulphides as catalysts on a glassy carbon electrodes. While metallic HER catalysts typically exhibit rapid electron transport due to their good electronic conductivity, electrodes made of an assembly of nanoparticles–especially non-metallic nanoparticles–can experience bottlenecks in electron transport. This phenomenon is observed with molybdenum sulphides [62].

**Catalytic activity of β-Ni(OH)$_2$ superstructures:** Three dimensional hierarchical petal-like nanosheets decorated with β-Ni(OH)$_2$ nanoburls have been synthesized through solvothermal method [63]. These materials upon activation with the oxyhydroxide formed at the facets exhibits a relatively low overpotential of 0.300 ± 0.003 V at current density of 10 mA cm$^{-2}$, low value of the Tafel slope *ca.* 0.043 V dec$^{-1}$ and very high turn-over frequency of 47.14 s$^{-1}$ at 1.53 V *vs.* RHE and increased faradaic efficiency. It has been seen that metallic platinum can act as efficient electrocatalysts in hydrogen evolution reaction where a low overpotential close to zero and Tafel slope of 30 mV dec$^{-1}$ have been achieved.

**Transition-metal electrocatalysts:** The transition metals, such as, Fe, Co, Ni and Cu are promising cost-effective electrocatalysts for cathodic reactions because of their earth abundance and high electrical conductivity. Transition metal electrocatalysts are, sometimes, shared with anions that broadens *d*-bands of the parent metalsupon hybridization with the corresponding *s*-orbitals [64].

## 1.5. Objectives of the present work

Based on these backgrounds, the objectives of the present work have been formulated. The nanoparticles have been synthesised through wet chemical techniques. The chemically synthesized metal alloy nanoparticles have been characterized by spectroscopic, microscopic and electrochemical studies. The morphology of the nanoparticles has been investigated by using transmission electron microscopy, high resolution transmission electron microscopy and selected area electron diffraction patterns. The morphology of the electrode surface has been investigated with scanning electron microscopy. The field emission scanning electron microscopy measures the shape and size of the particles. The elemental composition of the particles can be determined by using energy dispersive X-ray spectroscopy. X-ray diffraction provides the crystalline structures and phase purity of the metallic nanocomposites. The experiments of the present thesis work have been organized into four chapters:

**Chapter 1:** This chapter describes the hydrothermal synthesis of nickel containing nanoparticles. The electrocatalytic activities of the synthesized catalysts have been explored in reference to alkaline and acidic oxidation for the water splitting reaction. The morphology and surface ligand characteristics of the as-synthesized nanoparticles have been probed by using scanning electron microscopy, transmission electron microscopy, powder X-ray diffraction technique and Fourier transform infrared spectroscopy. These three types of nanoparticles have been employed as electrocatalysts towards the water oxidation reaction. The best electrocatalysts, NiSe provide a current density of 10 mA $cm^{-2}$ at 259.0 mV overpotential while for OER in 1.0 M KOH, which is superior to state-of-the-art catalysts $RuO_2$ in the same environment. For HER the best electrocatalyst, NiSe provides a current density of 10 mA $cm^{-2}$ at 49.5 mV overpotential in 0.5 M $H_2SO_4$, which is again superior to Pt wire electrode.

**Chapter 2:** The hydrothermal synthesis of Cu-based nanoparticles and their electrocatalytic activity have been covered in this chapter. Copper is one of the most inexpensive, readily available elements on Earth that can improve electrocatalytic activity amongst the transition metal elements. CuSe nanoparticles have been employed as highly effective bifunctional electrocatalysts in the water splitting reaction. Water oxidation performance of electrocatalysis has been studied in an alkaline solution containing 0.5 M $H_2SO_4$ solution for HER and 1.0 M KOH solution for OER. The electrocatalysts have an overpotential of 343 mV for OER and 126 mV for HER, respectively, to achieve a current density of 10 mA $cm^{-2}$.

**Chapter 3:** This chapter deals with the hydrothermal synthesis of NiS, MoS, and NiMoS nanoparticles and observing their electrocatalytic properties in reference to OER under alkaline condition. It shows an overpotential of 124 mV (10 mA $cm^{-2}$) and Tafel slope of 41.6 mV $dec^{-1}$ in 1.0 M KOH for NiMoS nanostructures. The values of double layer capacitance of NiS, MoS and NiMoS electrocatalysts have been calculated to be 3.72, 1.20 and 2.23 mF $cm^{-2}$.

**Chapter 4:** This chapter deals with the hydrothermal synthesis of nickel selenide, molybdenium diselenide and nickel molybdenium selenide nanoparticles. The electrocatalytic water splitting towards OER overpotential with respect to RHE is 165 mV with a lower Tafel slope 83 mV $dec^{-1}$. The double layer capacitance of the catalyst is 9.5 mF $cm^{-2}$ and electrocatalytic active surface area is 9.5 $cm^{-2}$.

## 1.6. Transition metals

A variety of the transition metals, as well as iron, cobalt, and nickel along with their corresponding oxides, phosphides, and sulfides, have been the subject of extensive research interest due to their role as catalysts in the splitting of water molecules. These elements are capable of facilitating both the HER and OER, which represent the two complementary processes of water splitting reaction. A revolutionary advancement in this domain is the creation of a single catalyst that combines the functions of HER and OER, offering multiple benefits. This innovation simplifies the architecture of electrochemical cells and diminishes the financial outlay associated with the water splitting operation. Typically, this is achieved using bifunctional catalysts. These catalysts can be adopted at functioning under uniform conditions, which consolidates the operational procedure and bolsters the robustness of the system. Bifunctional catalysts are intricately designed substances capable of concurrently promoting both HER and OER tasks that were previously assigned to distinct materials. Their dual-capability streamlines the water splitting apparatus and fosters the economic and efficiency gains. Predominantly, these bifunctional catalysts also consist of transition metals, such as nickel (Ni), iron (Fe), and cobalt (Co), which are often amalgamated with non-metallic elements, like phosphorus (P) or sulfur (S), resulting in the formation of compounds, such as $Ni_3FeOx$ nanoparticles. These compounds are distinguished by their remarkable catalytic processes and durability, rendering them ideal for enduring water electrolysis applications.

Bifunctional catalysts are at the forefront of innovation, yet they face hurdles in achieving optimal performance, especially concerning their enduring stability and reactivity across different pH levels. The focus of ongoing research is to refine the effectiveness of these catalysts by employing methods, such as nanostructuring, alloying, and modifying the surface properties.

## 1.7. Heterogeneous catalysts

In the realm of bifunctional catalysts, recent advancements have led to the creation of both homogeneous and heterogeneous types. Homogeneous catalysts are characterized by their soluble complexes that possess varied functionalities and catalytic actions, linked either through covalent bonds or electrostatic interactions. Conversely, heterogeneous catalysts feature active sites on the exterior of solid substances or on supporting materials. These active sites may be closely packed at a molecular scale or spaced more broadly at a mesoscopic level, as seen when various nanoparticles are anchored onto supports. The proximity of active sites is advantageous, potentially expediting subsequent reactions due to the concentrated presence of the initial product of the catalysts. However, negative outcomes may arise if the product from the first catalyst hinders the second, or if the catalytic substances interact detrimentally, leading to inactivation. Therefore, an ideal balance must be struck, necessitating precise adjustment of the spacing of the active sites during the formation of the catalysts.

The field of transition metal electrocatalysts, the process of nanostructure inaugmention of the surface area of the catalysts has recently seen notable advancements, and thereby, unveiling a greater number of active sites in the reaction. Significant research has been invested in incorporating nonmetal elements, such as boron, carbon, nitrogen, phosphorus, sulfur, and halides into these nanocatalysts. These elements act as acceptor states above the valence band, markedly enhancing light absorption and charge transportation capabilities of the catalysts. Employing novel approaches, such as introducing different elemental dopants or engineering distinct crystal facets, has resulted in catalysts with superior performance and increased stability. However, the quest for catalysts that exhibit robust performance across a broad pH spectrum and under substantial current densities for industrial use continues. Researchers are diligently working to surmount these challenges by fine-tuning the electronic structure and physical form of transition metal catalysts.

## 1.8. Photocatalysts

Photocatalytic water splitting necessitates specific characteristics in photocatalysts, particularly concerning their band gaps and energy levels. Photocatalysts are typically semiconductors in powdered or colloidal forms, which may be combined with dopants or cocatalysts to boost their performance. Upon exposure to photons with energy at or above band gap of the semiconductor and photogenerated electrons and holes within the valence and conduction bands respectively can initiate redox reactions. If these charges are conveyed to water molecules, they can facilitate water splitting, with electrons generating hydrogen and holes producing oxygen. It is key to note that recombination of charges can occur, notably diminishing the efficiency of water splitting. The band structure along with other bulk and surface attributes of the semiconductors profoundly influence the recombination of photogenerated charges. Crystalline photocatalysts with fewer defects are preferable for water splitting as defects can serve as sites for the recombination of electrons and holes in the photogenerative pathway, and reducing catalytic efficiency.

For water reduction reaction to occur, the conduction band of the photocatalysts must possess a potential below 0 V versus the NHE ($H^+/H_2$), as the valence band should have the potential greater than 1.23 V, equivalent to electromagnetic radiation of wavelength *ca.*1008 nm. Photocatalysts based on ultraviolet (UV) light, which has a higher energy per photon compared to visible light, are more efficient for hydrogen generation through solar water splitting. However, most existing photocatalysts are activated only by UV light, which represents a mere 4% of solar spectrum, while visible with 400 to 800 nm and infrared (>800 nm) light energy make up 53% and 43%, respectively. Given the limited share of UV light during the solar energy, it is crucial to develop photocatalysts that are not only responding to a broader spectrum, including visible and infrared light, but also enhances their solar to hydrogen conversion efficiency.

## 1.9. Scope and Objectives

### *1.9.1. Choice of medium*

The kinetic parameters in a reaction, including Gibbs free energy ($\Delta G^{\#}$) and enthalpy ($\Delta H^{\#}$) of activation, free energy of the activation ($\Delta G^{\#}$), and pre-exponential factor (A), are determined by using the Arrhenius and the Eyring relations. These parameters also play a vital role to understand the reaction kinetics on catalyst surfaces.

Specifically, for HER, the activation enthalpy ($\Delta H^{\#}$) strongly depends on overpotential that the potential difference between actual and thermodynamic potential. This behavior holds true for both platinum (Pt) and palladium (Pd) catalysts. Additionally, when using nafion as a binder in the coating slurry, it is essential to strike the right balance. Using too much nafion can lead to the formation of a thicker layer resulting in additional mass transmit resistance within nafion layer. However, the diffusion resistance of a nafion film remains insignificant and therefore, optimizing the additive amount of nafion is crucial.

### *1.9.2. Choice of catalysts*

Electrocatalysts based on platinum metals have been well-recognized as efficient electrocatalysts for the hydrogen evolution reaction during the process of water splitting. The use in electrocatalysts remains enormously low, primarily because active sites are confined to surface of the catalyst particles.

In the pursuit of sustainable hydrogen production, researchers have explored various alternatives to platinum-based catalysts. These alternatives include:

1. **Metal-Free Elemental Photocatalysts**: These include materials, like boron, carbon, phosphorus, sulfur, silicon, selenium, and others.
2. **Binary Photocatalysts**: Examples, include $BC_3$, $B_4C$, $C_xNy$, h-BN, and similar compounds.
3. **Ternary Photocatalysts**: BCN-based materials and their heterojunction counterparts fall into this category.
4. **Organic Photocatalysts**: These encompass linear organic frameworks, covalent organic frameworks, microporous polymers, and other organic compounds.

Among these, graphitic carbon nitride (g-$C_3N_4$) has garnered significant attention. This polymeric material, composed of a triazine-based pattern, exhibits a C/N ratio of 3/4 and contains a small amount of hydrogen. The synthesis of g-$C_3N_4$ typically involves thermal polymerization of precursors, such as dicyandiamide, cyanamide, urea, melamine, or thiourea at temperatures ranging from 450 °C to 650 °C.

**Key features of g-$C_3N_4$**:

- **Metal-Free**: It lacks any metal components.
- **Photocatalytic Activity**: g-$C_3N_4$ serves as a promising catalyst for removing $CO_2$ from the atmosphere.
- **Energy Conversion**: It can be utilized for energy conversion.
- **Wastewater Remediation**: g-$C_3N_4$ contributes to waste water treatment.
- **Organic Synthesis**: It finds applications in organic synthesis.

In summary, g-$C_3N_4$ holds great potential as metal free photocatalyst for the HER in water splitting reaction.

## 1.10. Characterization techniques

### *1.10.1. X-Ray diffraction (XRD)*

To determine the physical characteristics, crystallographic formation of nanostructured based materials, X-Ray diffraction (XRD) method can be performed. The diffraction experiments are based on the scattered intensity, which is confirmed by the incident and scattered angles by wavelength and energy after an X-ray strikes a sample [65].

For X-ray diffraction study, single crystals and powder samples both are used [66]. XRD is an analytical technique which is employed for phase recognition of a crystalline material. It provides the information on structural phases, crystalline orientations and other structural parameters. XRD peaks are formed by productive interference of a monochromatic X-rays scattered beam at a specific angle from each plane in a sample. The peak intensities result by the sharing of atoms within the lattice.

An X-ray beam is diffracted when it is obstructed by a sample. Then, we use Bragg’s law to calculate the distances between the atomic planes that make up the sample. This formula is $n\lambda = 2d \sin\theta$, where $\lambda$ is an integer, n the order of the diffracted beam, d the distance between the adjacent atomic planes, and $\theta$ the angle between the incidence of the X-ray beam. Diffraction occurs when an X-ray beam is hit by a sample. Next, Bragg's law can be utilized to calculate the distances between the atomic planes present in the sample. This formula is as follows: $n\lambda = 2d\sin\theta$, where $\lambda$ is an integer, n is the diffracted beam order, d is the distance between the adjacent atom planes, and is the angle between the X-ray beam's incidence [67-69]. From peak width in the diffraction patterns, the average crystallite size of nanoparticles can be enumerated by using Debye-Scherrer equation: $D = 0.9\lambda/\beta\cos\theta$, where D is the average size (nm) of nanocrystallites, $\lambda$ the wavelength of the X-ray, $\beta$ the full-width at half maximum (FWHM) and $\theta$ is the Bragg's angle. By measuring the values of $\theta$, we can calculate *d*-spacing values. A distinct "fingerprint" of the components or materials contained in the samples can be obtained from the properties of d-spacings produced during an X-ray scan. The "fingerprint" allows for material identification when the beams are correctly understood, by comparison with the usual reference patterns & parameters. The features of the d-spacings produced during an X-ray scan offer a distinct "fingerprint" of the constituents or substances found in the specimens. A "fingerprint" of a material can be used for identification when the beams are correctly interpreted and compared to the standard patterns and measurements as the references.

A proceeding sample platform, an X-ray source, and an X-ray detector attached to computer-controlled electronics comprise of a modern powder X-ray diffractometer. The sample is placed into a quartz substrate or packed into a shallow cup bent holder. In order to minimize sample heating during the experiment, the sample holder is slowly spined. The platform containing the sample rotates at an angle of $2\theta$ with respect to the fixed X-ray beam. The detector is oriented at $2\theta$ angle with respect to the received X-ray beam and rotates twice as fast as the sample. In the tube, a high voltage of 15–60 kV is applied. High voltage accelerates the electrons as they strike the target, which is often constructed of copper. X-rays are released when the electrons strike the object. The properties of the target can be reflected in the X-ray wavelengths. After the X-ray signal is detected by the detector, it is converted by microprocessor into a readable form or electronically converts the signal count to rate. An X-ray scan occurs when the angle between the X-ray source and the detector is altered at a regulated pace between the predetermined limits. The sample platform revolves around the fixed X-ray beam at an angle of $\theta$. The detector rotates at an angle of $2^{o}$ with respect to the incoming X-ray beam and rotates at a pace twice that of the sample. On the Bruker D8 Advance X-ray diffractometer equipped with a $CuK_{\alpha}$ radiation source ($\lambda$=1.5418 $A^{o}$ generated at 40 KV and 40 mA), the XRD patterns for all the samples have been recorded.

### 1.10.2. Fourier transform infrared (FTIR) spectroscopy

An infrared spectrum of absorption or emission of a sample either in the solid, liquid, or gas phase can be obtained using the FTIR technique. Over a broad spectrum range, data with high spectral resolution can be simultaneously collected using an FTIR spectrometer. The data in the FTIR spectrum is recorded between 4000 and 400 cm$^{-1}$ which represents molecular fingerprint of the samples. It identifies the presence of organic and inorganic compounds in the samples. The spectra can be used to identify and characterize foreign materials, find additives, identify decomposition and oxidation, and detect any contaminants. The components of an FTIR spectrometer are a computer, amplifier, sample cell, detector, source, and A/D converter.

Initially, the signal is enhanced before being converted to a digital signal through the use of an A/D converter and amplifier [70]. Then, the signal is sent to the infrared radiation is passed through a sample; some of the radiation is absorbed while some passes through. The absorbed radiation is converted by the sample into vibrational or rotational energy. The resulting signal obtained by the detector is a spectrum typically ranging from 4000 to 400 cm$^{-2}$.

Afterwards, the signal is sent to the computer and processed through Fourier transformation.A small amount of the sample is taken and finely ground with KBr salt, and this powdered mixture is then pressed to form a pellet. For the characterization of the samples, infrared spectra were collected using Perkin Elmer Spectrum RX1 FTIR spectrometer with resolution 4 cm$^{-1}$.

### 1.10.3. Scanning electron microscopy (SEM)

The surface analysis of a sample is usually performed by an electron beam in the scanning electron microscopy (SEM). This method is employed to look into the discrete morphology and structure of materials. A persistent electron beam strikes the sample and scans transversely a rectangular area in a standard SEM. Electrons hit a sample either be directly backscattered or by re-emitted as secondary electrons, the frequencies of which fall in the X-ray region of the electromagnetic spectrum. SEM images are formed by the energy loss of secondary electrons. It is capable to imaging of bulk samples and also to produce the 3-D shape of a sample. During this process of image analysis, firstly, the sample is reserved on a metal stab and set with the conductive metal paste. The sample should be conductive to permit electron interactions. For most of the samples, usually platinum or gold metals, are predicted to coat the samples. The SEM images help to determine the morphological structures and chemical composition of the materials under different operating conditions.

The SEM has many advantages than other traditional microscopes. The device has a generous depth of field, enabling a larger portion of the specimen to b e in focus simultaneously. The comprehensible images makes the SEM instrument as one of the most useful techniques in the research today. All the morphological studies of the as-synthesized electrocatalysts were performed on field emission scanning electron microscopy (FESEM, INSPECT F50 FEI)

**Fig.1.2**. Digital camera photograph of a scanning electron microscope

### *1.10.4. Transmission electron microscopy (TEM)*

The TEM is an instrument which is used for high magnification studies of nanoparticles. The HRTEM is an extremely complex device with several programmable features. It is used with energy dispersive X-ray spectroscopy (EDS), which is a crucial tool for characterizing the composition of the materials. The accelerate voltage in the HRTEM instrument is exceptionally steady within the one part per million (ppm) or more range. The operating current of the device has a great deal of sensitivity. It operates at a steady current, and the lens current needs to be monitored at all times. When the sample is tilted or an additional field of view is chosen, the height of the specimen needs to be appropriately changed in accordance with the change in lens current. Direct image of the atomic structure of a sample is made possible by this process. Currently, the HRTEM instrument achieves a point resolution of up to 0.05 nm possessing a power to resolve imperfections of individual crystal atoms. In order to create a 3D map of three-dimensional crystals, it is necessary to merge many views obtained from various angles using the process called electron tomography. During the experiments, the sample grids are prepared by drop casting method on carbon coated copper grids having the mess size of 200-300. Small quantity of powder sample is dissolved in the solvent of methanol, ethanol or isopropanol and it is sonicated to obtain the fine dispersion of powder sample. Minimal one drop of this disseminated solutions are placed on the grid and then, dried at room temperature under vacuum. In this way, the sample is made ready for the electron microscope chamber [72].

The interference in the wave plane of the electrons itself causes the contrast in the HRTEM image. Transmission electron micrographs of all the materials throughout my research period were imaged using a JEOL JEM 2010 transmission electron microscope with an operating voltage in the range from 100 to 200 kV.

### *1.10.5. Energy-dispersive X-ray spectroscopy (EDX or EDS)*

Energy-dispersive X-ray spectroscopy (EDX) is an elemental composition analysis technique. This is, basically, a kind of X-ray fluorescence spectroscopy that depends on using the light-matter interactions to investigate a sample. Moseley’s law, which reads as, $\nu = \alpha\ (Z-\beta)^2$, can be used to explain X-ray emission of an atom. In this equation, $\nu$ represents the frequency of the emitted X-ray line, Z the atomic number of the element, and $\alpha$ and $\beta$ are the line constants [73].

### *1.10.6. X-ray photoelectron spectroscopy (XPS)*

The surface chemistry of the catalysts can be examined by using X-ray photoelectron spectroscopy (XPS). Finding the chemical state of the atoms and elemental composition is the main goal of this experiment. XPS is a powerful technique for probe deep into surface chemistry and can provide valuable information about a material. It is surface sensitive and non-destructive technique which can be used to analyze the outermost *10 m (~30 atomic layers) of natural and synthesized materials. The kinetic energy and the quantity of electrons that emerges from 0-10 nm of the surface can be determined by measuring the surface atoms of the solid catalysts under the X-ray beam. In the spectra, the *y*-axis represents the surface intensity of the materials, which shows the amount of a given element present on the surface, while the *x*-axis displayed the elemental and chemical compositions based on the position of the peaks. The relative number of electrons with a certain binding energy is indicated as peaks in the XPS spectra. The photoelectric effect, which is the basis of XPS, a surface-sensitive quantitative spectroscopic technique, allows one to determine the elements present in a material, their chemical state, its overall electronic structure, and the density of electronic states in the material. Because it may reveal both the elements that are present and the other elements to which they are linked, XPS is a highly effective measurement method. It is frequently used to investigate chemical reactions in materials either in their raw form or following cleavage, scraping, heating, exposure to reactive gases or solutions, UV radiation, or ion implantation. The energy of each peak is unique to the particular element that is present in the sample [74-75]. A Thermo Fisher Scientific Multilab 2000 spectrometer operating at 150 W (12 kV, 12.5 mA) was used to capture XPS during my research work. The non-monochromatic $AlK_a$ radiation (1486.6 eV) was used as the X-ray source.

## 1.11. Techniques employed for electrocatalytic study

Electrochemical measurements were performed using $Ag/AgCl/Cl^-$ as the reference electrode (RE), metal oxides/sulphides/selenides served as the working electrode (WE), and Pt wire served as the counter electrode (CE) to complete the circuit. Electrochemical measurements were performed in three electrode cells. In this technique, the parameters, like potential (V), current (mA) and time (s) is used. In voltammetry, potential and current are measured and in chronopotentiometry or chronoamperometry potential or current is measured with time. The data obtained from these techniques assist to recognize the catalytic behaviour of an electrode

### *1.11.1. Potentiodynamic technique: Cyclic voltammetry (CV)*

An electrochemical technique called cyclic voltage monitoring measures the current that results from cycling the working electrode. From an initial value, also known as the initial potential ($E_i$), to the final potential ($E_f$), and back to the initial potential, the potential is swept linearly with time (t). The system comprises as a working electrode, reference electrode, and counter electrode in a three-electrode system. It can be used to investigate the range of redox processes in order to ascertain the reversibility of an electrochemical reaction and the stability of reaction products as well as the reversibility of a reaction, the electron transfer kinetics [76], the presence of intermediates in redox reactions [77], and the stability of reaction products to assess the stability of reaction products in the presence of intermediates in redox reactions [78]. ]. The stoichiometry, the diffusion coefficient of the analytes, and the formal reduction potential can be determined using the cyclic voltammetry measurements. In a reversible technique, the concentration is proportionate to the current. From the calibration curve of current *vs.* concentration, the concentration of an unknown solution can be determined [79]. It is employed in organo-metallic chemistry to assess redox processes [80]. In addition, a number of requirements can also be explained for the redox processes, such as, choice of solvents [81]. The analyte needs to be dissolved into the solvent, having a high concentration of the supporting electrolyte, and remain stable in the potential window of the measurements.

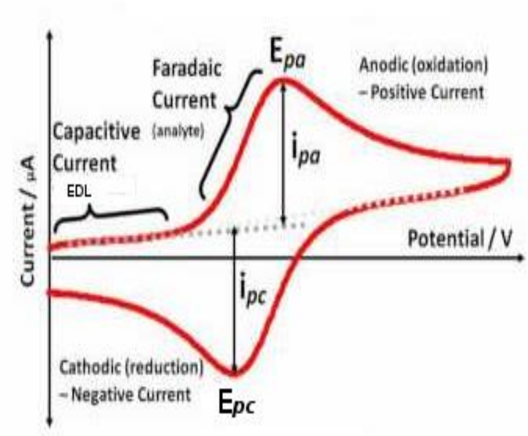

**Fig.1. 3**. Current-potential responses of triangular potential sweep experiment and salient features.

### *1.11.2. Linear sweep voltammetry (LSV)*

When the potential between the working and reference electrodes is swept linearly as a function of time, the current in a working electrode can be measured using linear sweep voltammetry (LSV) [82-83]. At a particular potential, the oxidation or reduction peak starts to occur. A potentiostat and a three-electrode setup are used in the LSV experiment to generate a potential in solution, which is, then, converted to the current. The reference, auxiliary, and three electrodes set up is operational. The scan rate, which varies in the range of 1.0 mV s$^{-1}$ to 10$^{6}$ Vs$^{-1}$, is the slope of potential *vs.* time curve [84]. It could not be stated whether any further data can be provided in specific situations where the reaction is irreversible in the cyclic voltammetry.

### *1.11.3. Controlled current technique: Chronoamperometry (CA)*

The time-dependent technique known as chronoamperometry involves applying a set of voltages to the working electrode. A square wave potential can be provided to the working electrode in this time-dependent approach. It is employed to quantify the temporal dependence of the diffusion processes. The controlled processes occur at an electrode where the time dependence in the diffusion of the analytes from the bulk solution to the electrode surface can be determined. Measuring the electroactive species in a solution is simple when the electrode area is known. The technique is employed to investigate the adsorption, diffusion, and reaction kinetics. The two types of chronoamperometry are known, i. e., controlled-potential and controlled-current. The equation in chronoamperometry is the Cottrell equation, which describes the experimental current at a time for a large forward potential in a reversible reaction as the function of $t_{1/2}$. The Cottrell equation is known by the equation,

$$i_d(t) = \frac{nFAD_o^{1/2}C_o}{(\pi t)^{1/2}} \tag{1.51}$$

where Cottrell current is denoted by $i_d$ (t), t the time (s), A the area of the electrode ($cm^2$), F the Faraday constant (96,485 C $mol^{-1}$), I current (A), n the number of electrons being transferred in the half reaction, $D_A$ the diffusion coefficients ($cm^2$ $s^{-1}$), and $C_A$ the initial (bulk) concentration of electroactive species (mol $cm^{-3}$)[85].The Cottrell equation can be used to determine the coefficient of the electroactive species when the current is regulated by diffusion.

## 1.12. Parameters for the evaluation ofelectrochemical water splitting

To study the electrochemical water splitting reaction, important parameters, *viz.*, overpotential (η) at different current densities (j), Tafel slope, turnover frequency (TOF), electrochemical active surface area (ECSA), exchange current density are determined.

### *1.12.1. Overpotential*

In electrochemistry studies, the overpotential is a measure of the potential difference between the thermodynamic reduction potential and the particular potential where the redox reaction occurs [86]. In electrolytic cell, the overpotential implies that the cell requires an additional energy to drive the chemical reaction. There exist three main types of overpotential, *viz.*, activation, resistance and concentration [87]. The potential difference between the equilibrium value that is required to generate a current dependent on the activation energy of a redox process is known as the activation overpotential that has also been coined as electron transfer overpotential. The Cottrell equation partially explains the phenomenon of polarization overpotential, which is a component of cyclic voltammetry measurements.

### *1.12.2. Concentration overpotential*

Similar to the "polarization overpotential", the "diffusion overpotential" can be thought of as a concentration overpotential caused by a slow diffusion of charges. The peak current is insufficient due to analyte diffusion, but the overpotential can be computed using the activation overpotential.

The variations in charge carrier concentration between the bulk solution and the entire electrode surface causes the potential difference. The ability of the charge carriers to reach the electrode surface determines the rate of reaction. Another parameter called "junction overpotentials", which happen at the electrode surfaces and electrolyte membrane interfaces, are included in resistance overpotentials. These may consist of the diffusion of electrolytes, surface polarization (capacitance), and other causes of generating electromotive forces.

Although it is not an ideal practice, the overpotential at 10 mA $cm^{-2}$ has been implied in the OER and the HER [88-89]. The overpotential, which is the resultant overpotential denoted as $\eta$, is well known and is necessary to overcome the kinetic interference in electrochemical water splitting reactions (in both HER and OER) [90]. For electrocatalysts operating at varying pH levels, the standard current density for OER and HER is 10 mA $cm^{-2}$.

The processes of HER and OER bear the respective thermodynamic potentials of 0 and 1.23 V. The following equations provide the overpotential at the respective current density without any compensation of iR:

$$\eta_{HER} = E_{RHE} - 0 \text{ V and}$$

$$\eta_{OER} = E_{RHE} - 1.23 \text{ V [70–72]} \qquad (1.52)$$

### *1.12.3. Turnover frequency (TOF)*

The calculation of turnover frequency is the simplest and most effective way to figure out the active sites of the catalysts. However, one important limitation of the method of incorporation of redox maximum to its applicability to monometallic catalysts (e. g., Cu, Ni, Pt, Fe, Co, Mn, Ru and Ir) with a redox couple inside the potential range of the electrolytic process catalyzed by the metal surface.

Oxidative splitting of water is often caused by transition metal-based OER electrocatalysts, which undergo unique self-oxidation to a higher valence state. To prevent a significant loss in efficiency, tiny molecules are electrochemically transferred into fuels and products in electrolysers using materials with energy of connections [91–92]. Although TOF is dependent on high coverage and bears a linear relationship, is not affected by mass loading of the catalysts [93-94]. As the catalyst is better, the higher the turnover frequency. The definition of turnover frequency is given by,

$$\mathrm{TOF} = j \times N_A \Gamma \qquad (1.53)$$

where, n is the number of electrons being transferred (two for HER and four for OER), j is the current density (A $cm^{-2}$), G is the total/surface concentration of the active sites of the catalysts or the number of participating atoms in the electrocatalyst material, $N_A$ is the Avogadro number, and F is the Faraday constant. The TOF can be computed by taking into account the number of electrons that correspond to one turnover ($n = 2$), the conversion factor of the time unit for turnover frequency (1 h or 3600 s) over the $C_A$, and the duration of the experiment, t.

The TOF can be calculated as,

$$\mathrm{TOF} = (Q_T - Q_A) \times 3600/(Q_A - Q_B) \times n \times t \qquad (1.54)$$

The calculated value of TOF has a unit of one hour ($h^{-1}$). To show how the addition of base affects reaction kinetics, voltametric and chronoamperometric analyses were carried out under neutral reaction conditions.

The formula can be used to determine the corresponding turnover frequency values from the Tafel plots regarding galvanostatic experiment [95],

$$\mathrm{TOF} = I/2mF \qquad (1.55)$$

where the current values are obtained from the chronoamperometry electrolysis and are denoted by the numbers I, n, which stand for the number of active sites (mol), F, which stands for the Faraday constant (C $mol^{-1}$), and 2 for the number of electrons required. The value of m is given by,

$$m = Q/nF \qquad (1.56)$$

where Q can be derived by integrating the current *vs.* time plot produced from the trace of the cyclic voltammogram.

$$\begin{aligned} TOF &= I/2 \times F \times Q/n \times F \\ &= n \times I/2 \times Q \qquad (1.57) \end{aligned}$$

The method adopted for TOF calculation should be appropriate depending on the nature of the catalysts [96].

### *1.12.4. Electrochemical active surface area (ECSA)*

Electrochemical active surface area (ECSA) and the mass are the parameters that should be taken into consideration to normalize the specific activity and mass activity of the loaded catalysts [97–98]. The area of the electrode material close to the electrolyte solution is represented by ECSA that can be utilized to determine the ability for charge transfer and storage. The double layer capacitance ($C_{dl}$) of the electrodes can be measured by using cyclic voltammetry in the possible window from 150-300 mV that belongs to the non-Faradaic region. In this process, an electrocatalytic reaction is studied as a function of scan rate [99]. Plotting the current of charging/discharging at varying scan rate yields linear plots and the values of $C_{dl}$ can be calculated from the slope of the curves. The non-Faradaic current obtained from the cathodic sweep is subtracted from the anodic sweep to yield both the currents. The subtraction expressed as, ($\Delta j = j_a - j_c$) against the scan rates to obtain $2C_{dl}$, from which the value of $C_{dl}$ can be enumerated [100]. The formula for estimating the non-Faradic current density is ECSA = $C_{dl}/C_s$, where $C_s$ is the specific capacitance. Studies using the same chemical but with varied surface characteristics and environments, such as pH, electrolytes, and so on-modify $C_s$ values [101]. The McCrory specific capacitance average of 40 µF $cm^{-2}$ in the alkaline solution has widely been used in the publications [102–104].

In either acidic or alkaline solution, individual current densities can be computed to provide a standardized value for specific capacitance [106–110]. Additional values of 80 or 20 are often employed, for the specified capacitance [111–113]. Assuming the $C_{dl}$ of electrode considering as a substrate with a smooth surface area of 1 $cm^2$, the value of ECSA can be computed.

### *1.12.5. Electrochemical impedence spectroscopy (EIS)*

Electrochemical impedance spectroscopy (EIS) provides kinetic and mechanistic information about the electrochemical systems and is commonly utilized to determine semiconductor characteristics, corrosion studies, energy conversion and storage technologies, chemical sensing and last but not the least non-invasive diagnostics. The foundation of electrochemical impedence spectroscopy (EIS) system is based upon the perturbation which disturbs the electrochemical system either in steady state or in equilibrium to generate a sinusoidal signal from the system [114].

Impedance means effective resistance to a discontinuous current circuit. It is considered by an AC potential applied to an electrochemical cell. An electrochemical cell reaction is uttered by equivalent circuit and consists of, capacitor C, resistor R, and inductor, I. The ideal resistance is autonomous of frequency, maintains Ohm's law and current and voltage are in one phase.

The excitation signal in the impedance is expressed as a function of time, $E = E_0 \sin(\omega t)$, where $E_0$, is the amplitude of the signal and $\omega$ is the radial frequency ($2\pi f$), and E is the potential at the time t. Phase shift $\varphi$ occurs in the response signal (frequency dependent current I).

Impedance of the system is,

$$Z = E/I$$

$$= E_0 \sin(\omega t) / I_0 \sin(\omega t + \phi)$$

$$= Z_0 \sin(\omega t) / \sin(\omega t + \phi)$$

$$= Z_0 \exp(i\phi)$$

$$= Z_0 (\cos\phi + i\sin\phi) \qquad (1.58)$$

From the above expression, it is seen that Z consists of both real and imaginary parts.

**Nyquist plot**

Corresponding to an automated control as well as signal processing, a parametric plot of a frequency is called a Nyquist plot. The real portion on the *x*-axis and the imaginary portion on the *y*-axis of the function in the Cartesian coordinates, gives the desired plot. The shape corresponding to the transfer function can be determined using the Nyquist plot. A corroding system can be thought of as having solution resistance when it is comprised of a resistor and a capacitor, which stand for polarization resistance and double layer capacitance, respectively. The stability of the electrochemical system against time, the limitation of the instrument that is available, and the connected wiring of the system with the instrument - all have an impact on the frequency range. Most of the electrochemical analyzers that are available commercially have a frequency range of 10 µHz to 1 MHz.

Thus, the electrochemical impedance spectroscopy (EIS) analyzes electrical resistance and inform the capacitative behavior of a system and the corresponding Nyquist plot have been presented in Fig. 1.6.

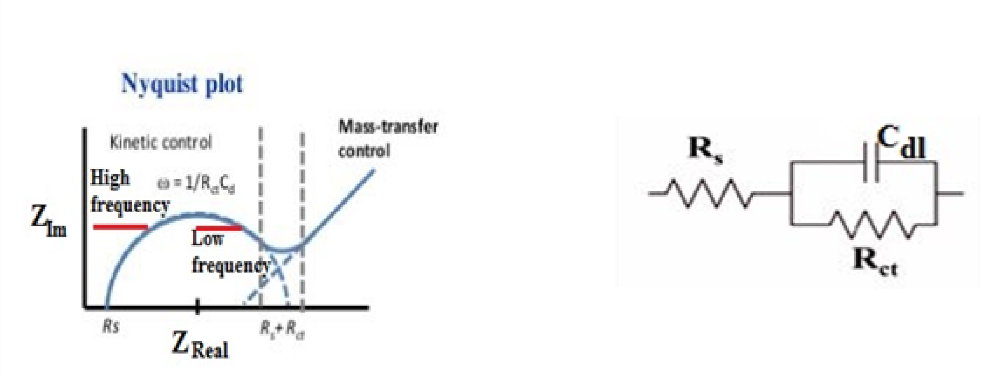

(a)

(b)

**Fig. 1.6.** (a) A typical Nyquist diagram and (b) equivalent circuit in electrochemical impedence spectroscopy

### *1.12.6. Butler-Volmer equation*

The rate constants of $\overleftarrow{k}$ and $\overrightarrow{k}$ depends on Gibbs energy of activation, $\Delta G_{act}$ by the subsequent equation,

$$k \alpha \exp(-\frac{\Delta G_{act}}{RT}) \qquad (1.59)$$

where $k = \overleftarrow{k}$ or $\overrightarrow{k}$ corresponding to $\Delta\overleftarrow{G}_{act}$ or $\Delta\overrightarrow{G}_{act}$.

The exact current density for oxidation is the net current density given by, $i = \overleftarrow{i} - \overrightarrow{i}$ where $\overleftarrow{i}$ is the backward current and $\overrightarrow{i}$ is the forward current. The net current density can also be expressed in the form,

$$i = F(\overleftarrow{k}C_R - \overrightarrow{k}C_O) \qquad (1.60)$$

where F is the Faraday constant.

The equation for net current density can be written as,

$$i = F[\overleftarrow{k}^0 C_R \exp\{\frac{(1-\beta)\phi F}{RT}\} - \overrightarrow{k}^0 C_O \exp\{-\frac{\beta\phi F}{RT}\}] \qquad (1.61)$$

where $\phi$ is metal and solution potential difference, $C_O$ and $C_R$ are concentrations of oxidised and reduced species, and $\overrightarrow{k}^0$ and $\overleftarrow{k}^0$ are the rate constants of the forward and reverse reactions in the absence of a metal solution potential difference. The parameter, $\beta$ is referred to the 'symmetry factor' which is correlated to symmetry of potential energy barrier involves in the activation controlled reaction, R is the universal gas constant and T is the temperature in Kelvin.

The rapidity of forward and backward reaction at the equilibrium is called **exchange current density** ($i_0$) is expressed as,

$$i_0 = F\overrightarrow{k}^0 C_O \exp(-\frac{\beta\phi_r F}{RT}) = F\overleftarrow{k}^0 C_R \exp[\frac{(1-\beta)\phi_r F}{RT}]. \qquad (1.62)$$

where $i_0$ is the kinetic properties of the particular interfacial system and it can vary from one reaction to another reaction and still from one electrode material to another. $i_0$ is dependent on the electrocatalytic activity of a catalyst of particular reaction and the concentration of reactant and often pH of the solution. Here, $\phi_r$ is the potential difference at the metal-solution interface at equilibrium.

Overpotential is the difference between the observable potential ($\phi$) and the net current flowing during the electrode ($\phi_r$) at the potential at the interface of equilibrium, that is, when no current flows during the electrode is called overpotential ($\eta$) and it is given by,

$$\eta = \phi - \phi_r \qquad (1.63)$$

Therefore, from the equations (1.62) and (1.63),

$$\frac{i}{i_o} = \exp[\frac{(1-\beta)\eta F}{RT}] - \exp[-\frac{\beta\eta F}{RT}] \tag{1.64}$$

The equation is well-known as simple Butler-Volmer equation.

When applying the high field approximation, i. e., when the $\eta$ value is very large,

$$\eta = -\frac{2.303RT}{(1-\beta)F}\log i_o + \frac{2.303RT}{(1-\beta)F}\log i \tag{1.65}$$

or, $\eta = a + b\log i$

The simple Butler-Volmer equation is the well-known name equation. When using the high field approximation, the standards values represent the distinctive feature of the electrode reaction, and ‘a’ and ‘b’ represent the Tafel intercept and slope, respectively. The data comes from η *vs.* log j plot. The Tafel slope, or ‘b’ of an electrochemical reaction should yield the same result for the same reaction mechanism. The value of the exchange current density at an equilibrium state is shown by the intercept ‘a’.

### *1.12.7. Stability*

The accelerated squalor test, also known as prolonged potentiostatic or galvanostatic electrolysis measurements, and the cycling of the catalysts within the potential window using two techniques - cyclic voltammetry (CV) or linear sweep voltammogram (LSV) at the higher scanrates - can be used to calculate the stability of HER and OER [66]. For both the OER and HER mechanisms, the number of cycles during the process impacts the stability of the catalysts. In HER, it can be recognized that the polarization curve begins at 0 V *vs.* NHE and continues for thousands of cycles [115].

## REFERENCES

[1] Y. Yan, B. Y. Xia, B. Zhao and X. Wang, A review on noble-metal-free bifunctional heterogeneous catalysts for overall electrochemical water splitting, J. Mater. Chem. A 4 (2016) 17587–17603.

[2] C. G. Morales-Guio, L. A. Stern, X. Hu, Nanostructured hydrotreating catalysts for electrochemical hydrogen evolution, Chem. Soc. Rev. 43 (2014) 6555–6569.

[3] X. Zou, Y. Zhang, Noble metal-free hydrogen evolution catalysts for water splitting, Chem. Soc. Rev. 44 (2015) 5148–5180.

[4] S. Kumar, R. Kaur, S. Sharma, Recent reports on hydrogen evolution reactions and catalysis, Results in Chemistry 4 (2022), 100613 1–11.

[5] Y. Shi and B. Zhang, Recent advances in transition metal phosphide nanomaterials: synthesis and applications in hydrogen evolution reaction, Chem. Soc. Rev. 45 (2016) 1529–1541.

[6] Y. Zhan, M. Lu, S. Yang, C. Xu, Z. Liu and J. Y. Lee, Activity of transition-metal (manganese, iron, cobalt, and nickel) phosphates for oxygen electrocatalysis in alkaline solution, ChemCatChem 8 (2016) 372–379.

[7] H. Osgood, S. V. Devaguptapu, H. Xu, J. Cho and G. Wu, Transition metal (Fe, Co, Ni, and Mn) oxides for oxygen reduction and evolution bifunctional catalysts in alkaline media, Nano Today 11 (2016) 601–625.

[8] E. Fabbri, A. Habereder, K. Waltar, R. Kötz, T. J. Schmidt, Developments and perspectives of oxide-based catalysts for the oxygen evolution reaction, Catal. Sci. Technol. 4 (2014) 3800–3821.

[9] I. C. Man, H. Y. Su, F. Calle-Vallejo, H. A. Hansen, J. I. Martı́nez, N. G. Inoglu, J. Kitchin, T. F. Jaramillo, J. K. Nørskov, J. Rossmeisl, Universality in oxygen evolution electrocatalysis on oxide surfaces, ChemCatChem 3 (2011) 1159–1165.

[10] A. Raveendran, M. Chandran, R. Dhanusuraman, A comprehensive review on the electrochemical parameters and recent material development of electrochemical water splitting electrocatalysts, RSC Adv. 13 (2023) 3843–3876.

[11] O. Vozniuk, N. Tanchoux, J. M. Millet, S. Albonetti, F. D. Renzo, F. Cavani, Spinel mixed oxides for chemical-loop reforming: From solid state to potential application studies in surface science and catalysis, Studies in Surf. Sci. Catal. 178 (2019) 281–302.

[12] Q. Qian, Y. Zhu, N. Ahmad, Y. Feng, H. Zhang, M. Cheng, H. Liu, C. Xiao, G. Zhang, Y. Xie, Recent advancements in electrochemical hydrogen production via hybrid water splitting, Adv. Mater. 36 (2023) 2306108 1–45.

[13] S. Y. Tee, K. Y. Win, W. S. Teo, L. -D. Koh, S. Liu, C. P. Teng, M. -Y. Han, Recent progress in energy-driven water splitting, Adv. Sci. 4 (2017) 1600337 1–61.

[14] Y. Wu, T. Sakurai, T. Adachia, Q. Wang, Alternatives to water oxidation in the photocatalytic water splitting reaction for solar hydrogen production, Nanoscale, 15 (2023) 6521–6535.

[15] Y. Liu, Y. Guo, Y. Liu, Z. Wei, K. Wang, Z. Shi, A mini review on transition metal chalcogenides for electrocatalytic water splitting: Bridging material design and practical application, Energy Fuels 37 (2023) 2608−2630.

[16] S.Li, E. Li, X. An, X. Hao, Z. Jiang, G. Guan, Transition metal-based catalysts for electrochemical water splitting at high current density:current status and perspectives, Nanoscale 13 (2021) 12788−12817.

[17] C. C. L. McCrory, S. Jung, J. C. Peters, T. F. Jaramillo, Benchmarking heterogeneous electrocatalysts for the oxygen evolution reaction, J. Am. Chem. Soc. 135 (2013) 16977−16987.

[18] S. L. Goes, M. N. Mayer, J. E. Nutting, L. E. Hoober-Burkhardt, S. S. Stahl, M. Rafiee, Nanostructured catalysts for electrochemical water splitting: current state and prospects, J. Mater. Chem. A 4 (2016) 11973−12000

[19] Y. Zhao, D. P. A. Saseendran, C. Huang, C. A. Triana, W. R. Marks, H. Chen, H. Zhao, G. R. Patzke, Oxygen evolution/reduction reaction catalysts: from in situ monitoring and reaction mechanisms to rational design, Chem. Rev. 123 (2023) 6257–6358.

[20] S. Anantharaj, K. Karthick and S. Kundu, Evolution of layered double hydroxides (LDH) as high performance water oxidation electrocatalysts: A review with insights on structureactivity and mechanism, Mater. Today Energy 6 (2017) 1–26.

[21] L. D. S. Munoz, A. Bergel, D. Fèron, R. Basseguy, Hydrogen production by electrolysis of a phosphate solution on a stainless steel cathode, Int. J. Hydrogen Energy 35 (2010) 8561–8568.

[22] H. Vrubel, T. Moehl, M. Grätzel, X. Hu, Revealing and accelerating slow electron transport in amorphous molybdenum sulphide particles forhydrogen evolution reaction, Chem. Commun. 49 (2013) 8985–8987.

[23] S. Anantharaj, P. Karthik and S. Kundu, Self-assembled $IrO_2$ nanoparticles on a DNA scaffold with enhanced catalytic and oxygen evolution reaction (OER) activities, J. Mater. Chem. A 3 (2015) 24463–24478.

[24] S. Anantharaj, P. Karthik and S. Kundu, Petal-like hierarchical array of ultrathin $Ni(OH)_2$ nanosheets decorated with $Ni(OH)_2$ nanoburls: A highly efficient OER electrocatalyst, Catal. Sci. Technol. 7 (2017) 882–893.

[25] S. L. Goes, M. N. Mayer, J. E. Nutting, L. E. Hoober-Burkhardt, S. S. Stahl, M. Rafiee, Deriving the turnover frequency of aminoxyl-catalyzed alcohol oxidation by chronoamperometry: An introduction to organic electrocatalysis, J. Chem. Ed. 98 (2021) 600−606.

[26] A. P. Garci, D. Perivoliotis, X. Wu, E. Gracia-Espino, Benchmarking molybdenum-based materials as cathode electrocatalysts for proton exchange

membrane water electrolysis: Can these compete with Pt?, ACS Sustainable Chem. Eng. 11 (2023) 7641−7654

[27] J. Zhu, Y. Ni, Phase-controlled synthesis and the phase dependent HER and OER performances of nickel selenide nanosheets prepared by an electrochemical deposition route, CrystEngComm 20 (2018) 3344−3352.

[28] Y. Gong, Y. Zhi, Y. Lin, T. Zhou, J. Li, F. Jiaoa, W. Wanga, Controlled synthesis of bifunctional particle-likeMo/Mn-$Ni_xS_y$/NF electrocatalyst for highly efficient overall water splitting, Dalton Trans. 48 (2019) 6718−6729.

[29] R. Karthick, A. Arulraj, M. Ramesh, M. Selvaraj Free-standing graphene/NiMoS paper as cathode for quasi-solid state dye-sensitized solar cells, J. Colloid Interface Sci. 530 (2018) 179–188.

[30] L. Bruno, S. Battiato, M. Scuderi, F. Priolo, A. Terrasi, S. Mirabella, Physical insights into alkaline overall watersplitting with NiO microflowers electrodes with ultra-low amount of Pt catalyst, I. J. Hydrogen Energy 47 (2022) 33988−33998.

[31] R. Q. Li, S. Li, M. Lu, Y. Shi, K. Qu, Y. Zhu, Energy-efficient hydrogen production over a high-performance bifunctional NiMo-based nanorods electrode, J. Colloid Interface Sci. 571 (2020) 48–54.

[32] S. K. Mustafa, M. A. A. Sharif, Copper (Cu) an essential redox-active transition metal in living system−A review article, Am. J. Anal. Chem. 9 (2018) 15−26.

[33] A. S. Sabir, E. Pervaiz, R. Khosa, U.Sohail, An inclusive review and perspective on Cu-based materials for electrochemical water splitting, RSC Adv. 13 (2023) 4963−4993.

[34] H. Sun, H. Kim, S. Song, W. C. Jung, Copper foam-derived electrodes as efficient electrocatalysts for conventionaland hybrid water electrolysis, Mater. Rep. Energy 2 (2022) 100092−100109

[35] Y. W. Dong, B. Y. Guo, Q. W. Chen, B. Dong, Preparation of molybdenum doped nickel sulfides supported on nickel foam via two-step electro deposition for oxygen evolution reaction, Int. J. Electrochem. Sci., 15 (2020) 5529–5539.

[36] J. D. Benck, T. R. Hellstern, J. Kibsgaard, P. Chakthranont, T. F. Jaramillo, Catalyzing the hydrogen evolution reaction (HER) with molybdenum sulfide anomaterials, ACS Catal. 4 (2014) 3957−3971.

[37] A. Sajeev, V. K. Mariappan, D. Kesavan, K. Krishnamoorthy, S. J. Kim, Efficient electrochemical water splitting using copper molybdenum sulfide anchored Ni foamas a high-performance bifunctional catalys, Mater. Adv. 2 (2021) 455−463.

[38] J. Ying, J. B. Chen, Y. X. Xiao, S. I. C. Torresi, K. I. Ozoemena, X. Y. Yang, Recent advances in Ru-based electrocatalysts for oxygen evolution reaction, J. Mater. Chem. A 11(2023) 1634−1650.

[39] C. Yang, Y. Lu, W. Duan, Z. Kong, Z. Huang, T. Yang, Y. Zou, R. Chen, S. Wang, Recent progress and prospective of nickel selenide-based electrocatalysts for water splitting, Energy Fuels 35 (2021) 14283−14303.

[40] X. L. Wang, C. Xue, N. Kong, Z. Wu, J. Zhang, X. Wang, R. Zhou, H. Lin, Y. Li, D. S. Li, T. Wu, Molecular modulation of a molybdenum−selenium cluster bysulfur substitution to enhance the hydrogen evolution reaction, Inorg. Chem. 58 (2019) 12415−12421.

[41] J. Q. Wang, C. Xi, M. Wang, L. Shang, J. Mao, C. -K. Dong, H. Liu, S. A. Kulinich, X. W. Du, Laser-Generated grain boundaries in ruthenium nanoparticles for boosting oxygen evolution reaction, ACS Catal. 10 (2020) 12575–12581

[42] J. N. Hansen, H. Prats, K. K. Toudahl, N. M. Secher, K. Chan, J. Kibsgaard, I. ChorkendorffIs, There anything better than Pt for HER?, ACS Energy Lett. 6 (2021) 1175−1180.

[43] N. E. Sahin, W. J. Pech-Rodríguez, P. C. Meléndez-González, J. L. Hernández, E. Rocha-Rangel, Water splitting as an alternative for electrochemical hydrogen oxygen generation: Current status, trends, and challenges, Energies 16 (2023) 5078−5103.

[44] W. Feng, M. Bu, S. Kan, X. Gao, A. Guo, H. Liu, L. Deng, W. Chen, Interfacial hetero-phase construction in nickel/molybdenum selenide hybrids to promote the water splitting performance, Appl. Mater. Today 25 (2021) 101175−101186.

[45] S. Ram, T. Dusan, S. Dusan, C. Kee-Chul, U. Masanobu, P. P. Arvydas, S. Vojislav, M. M. Nenad, Enhancing hydrogen evolution activity in water splitting by tailoring $Li^+$-$Ni(OH)_2$-Pt interfaces, Science 334 (2011) 1256–1260 .

[46] H. Y. Li, S. M. Chen, X. F. Jia, B. Xu, H. F. Lin, H. Z. Yang, L. Song, X. Wang, Amorphous nickel-cobalt complexes hybridized with 1T-phase molybdenum disulfide *via* hydrazine-induced phase transformation for water splitting, Nat. Commun. 8 (2017) 15377−15387

[47] H. Q. Zhou, F. Yu, Y. F. Huang, J. Y. Sun, Z. Zhu, R. J. Nielsen, R. He, J. M. Bao, W. A. Goddard, S. Chen, Z. F. Ren, Efficient hydrogen evolution by ternary molybdenum sulfoselenide particles on self-standing porous nickel diselenide foam, Nat. Commun. 7 (2016) 12765−12771.

[48] J. K. Norskov, T. Bligaard, J. Rossmeisl, C. H. Christensen, Towards the computational design of solid catalysts, Nat. Chem. 1 (2009) 37–46.

[49] W. Feng, W. Pang, Y. Xu, A. Guo, X. Gao, X. Qiu, W. Chen, Transition metal selenides for electrocatalytic hydrogen evolution reaction, ChemElectroChem 7 (2019) 31–54.

[50] H. Zhou, Y. Wang, R. He, F. Yu, J. Sun, F. Wang, Y. Lan, Z. Ren, S. Chen, One-step synthesisof self-supported porous $NiSe_2$/Ni hybrid foam: an efficient 3D electrode for hydrogen evolution reaction, Nano Energy 20 (2016) 29–36.

[51] L. Zhang, T. Wang, L. Sun, Y. Sun, T. Hu, K. Xu, F. Ma, Hydrothermal synthesis of 3D hierarchical $MoSe_2$ /$NiSe_2$ composite nanowires on carbon fiber paper and their enhanced electrocatalytic activity for the hydrogen evolution reaction, J. Mater. Chem. A 5 (2017) 19752–19759.

[52] X. Zhang, Y. Y. Zhang, Y. Zhang, W. J. Jiang, Q. H. Zhang, Y. G. Yang, L. Gu, J. S. Hu, L. J. Wan, Phase-controlled synthesis of 1T-$MoSe_2$ /NiSe heterostructure nanowire arrays via electronic injection for synergistically enhanced hydrogen evolution, Small 3 (2019) 1800317−11800322.

[53] A. P. Murthy, J. Theerthagiri, K. Premnath, J. Madhavan, K. Murugan, Single-Step electrodeposited molybdenum incorporated nickelsulfide thin films from low-cost precursors as highly efficienthydrogen evolution electrocatalysts in acid medium, J. Phys. Chem. C 121 (2017) 11108−11116.

[54] I. A. Raj, Nickel-basedbinary-composite electrocatalysts for the cathodes in the energy-efficient industrial production of hydrogen from alkaline-water electrolytic cells, J. Mater. Sci. 28 (1993) 4375–4382

[55] M. Gong, D. -Y. Wang, C. -C. Chen, B. -J. Hwang, H. Dai, A mini review on nickel-based electrocatalysts for alkaline hydrogen evolution reaction, Nano Res. 9 (2016) 28–46.

[56] L. Yu, I. K. Mishra, Y. Xie, H. Zhou, J. Sun, J. Zhoua, Y. Ni, D. Luo, F. Yu, Y. Yu, S. Chen, Z. Ren, Ternary $Ni_{2(1-x)}Mo_{2x}P$ nanowire arrays toward efficient and stable hydrogen evolution electrocatalysis under large-current-density, Nano Energy 53 (2018) 492–500.

[57] N. Mahmood, Y. Yao, J. -W. Zhang, L. Pan, X. Zhang, J. J. Zou, Electrocatalysts for hydrogen evolution in alkaline electrolytes: mechanisms, challenges, and prospective solutions, Adv. Sci. 5 (2018) 1700464–1700486.

[58] Y. Zheng, Y. Jiao, M. Jaroniec, S.Z. Qiao, Advancing the electrochemistry of the hydrogen-evolution reaction through combining experiment and theory, Angew. Chem. Int. Ed. 54 (2015) 52–65.

[59] H. E. G. Rommal, P. J. Moran, The role of absorbed hydrogen on the voltage-time behavior of nickel cathodes in hydrogen evolution, J. Electrochem. Soc. 135 (1988) 343–346.

[60] D. M. Soares, O. Teschke, I. Torriani, Hydride effect on the kinetics of the hydrogen evolution reaction on nickel cathodes in alkaline media, J. Electrochem. Soc. 139 (1992) 98–105.

[61] J. K. Nørskov, T. Bligaard, A. Logadottir, J. R. Kitchin, J. G. Chen, S. Pandelov, U. Stimming, Trends in the exchange current for hydrogen evolution, J. Electrochem. Soc. 152 (2005) J23–J26.

[62] B. Hammer, J. K. Nørskov, Why gold is the noblest of all the metals, Nature 376 (1995) 238–240.

[63] A. C. Lazanas, M. I. Prodromidis, Electrochemical impedance spectroscopy – A tutorial, ACS Meas. Sci. Au 3 (2023) 162–193

[64] X. Zou, Y. Zhang, Noble metal-free hydrogen evolution catalysts for water splitting, Chem. Soc. Rev. 44 (2015) 5148–5180.

[65] C. Giacovazzo, Fundaments of crystallography, Oxford University Press, UK, 1992.

[66] M. F. C. Ladd, R. A. Palmer, Structure determination by X-ray crystallography, Plenum, New York, 1985**.**

[67] A. L. Patterson, The Scherrer formula for X-ray particle size determination, Phys. Rev. 56 (1939) 978–982.

[68] A. A. Bunaciu, E. G. UdriŞTioiu, H. Y. Aboul-Enein, X-ray diffraction: instrumentation and applications, Critical Rev. Anal. Chem. 45 (2015) 289–299.

[69] D. M. Moore, Jr. R. C. Reynolds, X-Ray diffraction and the identification and analysis of clay minerals, 2nd ed., Oxford University, New York, 1989.

[70] H. Günzler, H. U. Gremlich, I R spectroscopy: An introduction, Wiley-VHC, Germany, 2002.

[71] P. R. Griffiths, J. A. de Haseth, Fourier Transform Infrared Spectrometry, Wiley, New York, 1986.

[72] D. Williams, C. B. Carter, Transmission Electron Microscopy; Springer: New York, 2009, 3−22.

[73] J. Goodge, Energy Dispersive X-ray Spectroscopy (EDS), University of Minnesota, Duluth, 2011.

[74] C. D. Wagner, W. M. Riggs, L. E. Davis, J. F. Moulder, G. E. Muilenberg, Handbook of X-ray Photoelectron Spectroscopy, Perkin-Elmer Corporation, Physical Electronics Division, 1979.

[75] J. F. Moulder, Handbook of X-ray photoelectron spectroscopy: A reference book of standard spectra for identification and interpretation of XPS data, Perkin-Elmer Corporation: Eden Prairie, 1992.

[76] R. S. Nicholson, Theory and application of cyclic voltammetry for measurement of electrode reaction kinetics, Anal. Chem. 37 (1965) 1351−1355.

[77] S. H. Duvall, R. L. McCreery, Control of catechol and hydroquinone electron – transfer kinetics on native and modified glassy carbon electrodes, Anal. Chem. 71 (1999) 4594−4602.

[78] A. M. Bond, S. W. Feldberg, Analysis of simulated reversible cyclic voltammetric responces for a charged redox species in the absence of added electrolyte, J.Phys.Chem. B 102 (1998) 9966−9974.

[79] G. A. Carriedo, The use of cyclic voltammetry in the study of the chemistry of metal carbonyls: An introductory experiment, J. Chem. Ed. 65 (1998) 1020−1022.

[80] W. E. Geiger, Reflections on future directions in organometallic electrochemistry, Organometallics 30 (2011) 28−31.

[81] A Practical Beginner's Guide to Cyclic Voltammetry, N. Elgrishi, K. J. Rountree, B. D. McCarthy, E. S. Rountree, T. T. Eisenhart, J. L. Dempsey, J. Chem. Ed. 95 (2018) 197−206.

[82] T. M. Nahir, R. A. Clark, E. F. Bowden, Linear-Sweep Voltammetry of irreversible electron transfer in surface confined species using the marcus theory, Anal. Chem. 66 (1994) 2595−2598.

[83] B. M. Tissue, Linear sweep voltammetry, CHP, 2013.

[84] Instrumentation, Pine Research, Linear sweep voltammetry, CHP, 2008.

[85] L. R. Faulkner, A. J. Brad, Electrochemical Methods: Fundamentals and applications, (2000).

[86] G. D. Short, E. Bishop, Concentration overpotentials on antimony electrodes in different electrolytic potentiometry, Anal. Chem. 37 (1965) 962–967.

[87] S. Anantharaj, S. R. Ede, K. Karthick, S. Sam Sankar, K. Sangeetha, E. K. Pitchiah, S. Kundu, Precision and correctness in the evaluation of electrocatalytic water splitting: revisiting activity parameters with a critical assessment, Energy Environ. Sci.11 (2018) 744–771.

[88] S. Anantharaj, S. Kundu, Do the evaluation parameters reflect intrinsic activity of electrocatalysts in electrochemical water splitting? ACS Energy Lett. 4 (2019) 1260–1264.

[89] S. Anantharaj, S. Noda, Amorphous catalysts and electrochemical water splitting: An untold story of harmony, Small 16 (2020) 1905779–1905803.

[90] S. Anantharaj, S. Noda, V. R. Jothi, S. C. Yi, M. Driess, P. W. Menezes, Strategies and perspectives to catch the missing pieces in energy-efficient hydrogen evolution reaction in alkaline media, Angew. Chem. Int. Ed. 60 (2021) 18981–19006.

[91] M. Boudart, Turnover rates in heterogeneous catalysis, Chem.Rev. 95 (1995) 661−666.

[92] K. Klingan, F. Ringleb, I. Zaharieva, J. Heidkamp, P. Chernev, D. Gonzalez-Flores, M. Risch, A. Fischer, H. Dau, Water oxidation by amorphous cobalt-based oxides: Volume activity and proton transfer to electrolyte bases, ChemSusChem 7 (2014) 1301–1310.

[93] S. Mulkapuri, A. Ravi, R. Nasani, S. K. Kurapati, S. K. Das, Barrel-shaped-polyoxometalates exhibiting electrocatalytic water reduction at neutral pH: A synergy effect, Inorg. Chem. 61 (2022) 13868–13882.

[94] B. Xiong, L. Chen, J. Shi, Anion-containing noble-metal-free bifunctional electrocatalysts for overall water splitting, ACS Catal. 8 (2018) 3688–3707.

[95] S. Anantharaj, H. Sugime, B. Chen, N. Akagi, S. Noda, Achieving increased electrochemical accessibility and lowered oxygen evolution reaction activation energy for Co $^{2+}$ sites with a simple anion preoxidation, J. Phys. Chem. C 124 (2020) 9673–9684.

[96] S. Anantharaj, H. Sugime, S. Yamaoka, S. Noda, Pushing the limits of rapid anodic growth of $CuO/Cu(OH)_2$ nanoneedles on Cu for the methanol oxidation reaction: Anodization pH is the game changer, ACS Appl. Energy Mater. 4 (2021) 899–912.

[97] S. Anantharaj, H. Sugime, S. Noda, Surface amorphized nickel hydroxy sulphide for efficient hydrogen evolution reaction in alkaline medium, Chem. Eng. J. 408 (2021) 127275–127288.

[98] L. Yua, S. Suna, H. Li, Z. J. Xua, Effects of catalyst mass loading on electrocatalytic activity: An example of oxygen evolution reaction, Fundamental Research 1 (2021) 448–452.

[99] S. Anantharaj, P. E. Karthik, S. Noda, The significance of properly reporting turnover frequency in electrocatalysis research, Angew. Chem. Int. Ed. 60 (2021) 23051–23067.

[100] J. Zhu, L. Hu, P. Zhao, L. Y. S. Lee, K.Y. Wong, Recent advances in electrocatalytic hydrogen evolution using nanoparticles, Chem. Rev. 2(2020), 851–918

[101] M. P. Browne, H. Nolan, G. S. Duesberg, P. E. Colavita, M. E. G. Lyons, Low-overpotential high-activity mixed manganese and ruthenium oxide electrocatalysts for oxygen evolution reaction in alkaline media, ACS Catal. 6 (2016) 2408–2415.

[102] H. Han, Y. R. Hong, J. Woo, S. Mhin, K. M. Kim, J. Kwon, H. Choi, Y. C. Chung, T. Song, Electronically double-layered metal boride hollow nanoprismas an

excellent and robust water oxidation electrocatalysts, Adv. Energy Mater. 9 (2019) 1803799–1803810.

[103] C. C. L. McCrory, S. Jung, I. M. Ferrer, S. M. Chatman, J. C. Peters, T. F. Jaramillo, Benchmarking hydrogen evolving reaction and oxygen evolving reaction electrocatalysts for solar water splitting devices, J. Am. Chem. Soc. 137 (2015) 4347–4357.

[104] R. Boggio, A. Carugati, S. Trasatti, Electrochemical surface properties of $Co_3O_4$ electrodes J. Appl. Electrochem. 17 (1987) 828–840.

[105] M. J. Gira, K. P. Tkacz, J. R. Hampton, Physical and electrochemical area determination of electrodeposited Ni, Co, and NiCo thin films, Nano Convergence 3 (2016) 6–13.

[106] D. Voiry, M. Chhowalla, Y. Gogotsi, N. A. Kotov, Y. Li, R. M. Penner, R. E. Schaak, P. S. Weiss, Best practices for reporting electrocatalytic performance of nanomaterials, ACS Nano 12 (2018) 9635–9638.

[107] W. Zheng, M. Liu, L. Y. S. Lee, Best practices in using foam-type electrodes for electrocatalytic performance benchmark, ACS Energy Lett. 5 (2020) 3260–3264.

[108] W. Zhang, W. Yuan, X. Zhang, Y. Ke, Y. Wu, Yafeng Bai, Functional high-entropy alloys: promising catalysts for high-performance water splitting, J. Mater. Chem. A (2024) in press. DOI: 10.1039/d4ta02271h

[109] S. Anantharaj, H. Sugime, S. Noda, Chemical leaching of inactive Cr and subsequent electrochemical resurfacing of catalytically active sites in stainless steel for high-rate alkaline hydrogen evolution reaction, ACS Appl. Energy Mater. 3 (2020) 12596–12606.

[110] C. Costentin, G. Passard, J. M. Savéant, Benchmarking of homogeneous electrocatalysts: overpotential, turnover frequency, limiting turnover number, J. Am. Chem. Soc. 137 (2015) 5461–5467.

[111] H. Vrubel, T. Moehl, M. Gratzelb, X. Hu, Revealing and accelerating slow electron transport inamorphous molybdenum sulphide particles for hydrogen evolution reaction, Chem. Commun. 49 (2013) 8985−8987.

[112] S. Anantharaj, P. E. Karthikc, S. Kundu, Petal-like hierarchical array of ultrathin $Ni(OH)_2$ nanosheets decorated with $Ni(OH)_2$ nanoburls: A highly efficient OER electrocatalyst, Catal. Sci. Technol. 7 (2017) 882−893.

[113] A. Kazemi, F. Manteghi, Z. Tehrani, Metal electrocatalysts for hydrogen production in water splitting, ACS Omega 9 (2024) 7310−7335.

[114] A. M. R. Ramirez, S. Heidari, A. Vergara, M.V. Aguilera, P. Preuss, M. B. Camarada, A. Fischer, Rhenium-based electrocatalysts for water splitting, ACS Mater. 3 (2023) 177−200.

[115] R. Boppella, J. Tan, J. Yun, S.V. Manorama, J. Moon, Anionmediated transition metal electrocatalysts for efficient water electrolysis: Recent advances and future perspectives. Coord. Chem. Rev. 427 (2021) 213552−213596.

# CHAPTER-I

# BIFUNCTIONAL CATALYSIS ON WATER SPLITTING REACTION BY GRAPHITIC CARBON SUPPORTED NiO, NiS AND NiSe NANOPARTICLES

# Bifunctional catalysis on water splitting reaction by graphitic carbon supported NiO, NiS and NiSe nanoparticles

## 2.1. Introduction

Continuous increase of global pollution along with fast depletion of fossil fuel rings the alarms of scientists for the generation of efficient carbon free renewable energy [1]. Among the different sources of energy, hydrogen is the best choice due to the high specific energy density, diffusion ability and particularly pollution free emission [2-4]. Low quality $H_2$ can be obtained by some environmentally hazardous expensive process of reforming of natural gas [5-7]. In this respect, synthesis of pure hydrogen from the abundant natural source of $H_2O$ by electrochemical water splitting is highly beneficial [8-12]. Electrocatalysis for the decomposition of water by either in the reaction of hydrogen or oxygen evolution is essential part in several environmentally benign energy storage and conversion devices, for example, fuel cells, water electrolyzer, metal–air batteries etc. [13-20]. Among different non-precious metals, Ni seems to be execellent catalysts for energy studies and applications. The non-metallic elements, like oxygen, sulphur, selenium possess the same group XVI in the periodic table. Compared to S and O, Se in NiX where X=O/S/Se, has the same valence electrons but greater intrinsic metal properties and electrical conductivity. The adsorption bond strengths of the intermediates are also expected to be different accordingly. Therefore, a systematic comparison is useful to understand their electrocatalytic activity.

Previous studies have shown that the $Ni^{II}$ compounds, like nickel oxyhydroxides, chalcogenides, pnictogenides, borates, phosphates, metal-organic framework, etc. can easily transform Ni(II) to Ni(III) creating in situ NiOOH sites [21]. It is revealed that NiOOH acts as active centres of OER and becomes resculer from poisonous effect of electrodes surface during oxidation. The electrochemical HER helps enrichment of heavy water and has become now so popular that the scientists are also trying to set hydrogen from non-aqueous solvents in presence of a proton donor. Synthesis of metal compounds of greater oxidation state is, thus, beneficial to produce oxyhydroxides as the reaction intermediates which is the main performer in the electrochemical water oxidation process, particularly under alkaline condition. For overall water splitting, a bifunctional electrocatalyst should be of low-cost, highly active and environmentally benign product which can provide long-term self and cyclic stability for both hydrogen evolution reaction (HER) and oxygen evolution reaction (OER). In this regard, the inexpensive and chemically stable non-noble metal based electrocatalysts have achieved significant attention. Non-noble metal compounds with elements, like phosphorus [22−24], sulphur [25−28], selenium [29−31], carbon [32-33] and nitrogen [34−35], etc. have been explored for HER and hydroxides [36−38], oxides [39−42], and chalcogenides [43], etc. have been employed for OER. Nonprecious transition metals, such as Fe, Co, Ni, Mn, etc., and the related structures, i. e., oxides, hydroxides, phosphates, and sulfides, have increasingly attracted research interest to develop OER and HER electrocatalysts in the recent years, owing to abundance, electrocatalytic activity, and their stability [44-49]. It is widely supported in the literature that Pt alloys and Ir/Ru oxides are the state-of-the-art catalysts for HER and OER, respectively. But their abundance and high cost [50] limit their marketable use. Chalcogenides are usually studied separately as electrocatalysts, but not systematically.

In the study, NiO, NiS and NiSe have been studied systematically as bifunctional catalysts by synthesizing them using similar hydrothermal method and observing their electrocatalytic properties in reference to OER and HER under acidic and alkaline conditions.

## 2.2. Experimental section

### *2.2.1. Reagents and instruments*

The reagents, nickel chloride hexahydrate ($NiCl_2.6H_2O$), sodium hydroxide (NaOH) (97% pure), potassium hydroxide (KOH) (99% pure) and sodium sulphide ($Na_2S.5H_2O$) (98 % pure) were purchased from Merck. Nafion solution (5 mass %) was taken from Sigma-Aldrich. All chemicals were used without further purification.

The purity and morphology of the synthesized catalysts were investigated with SEI INSPECTF 50 FE-SEM. Powder X-ray diffraction (XRD) study was executed using a Bruker D8 Advance diffractometer coupled with $CuK_\alpha$ radiation source ($\lambda$ = 1.5418 Å generated at 40 kV and 40 mA). Fourier transform infrared spectroscopy (FTIR) spectroscopic study was performed by PerkinElmer instrument.

### *2.2.2. Syntheses of NiO, NiS and NiSe nanoparticles*

In each case of syntheses, the equal volumes of aqueous solutions of 0.5 M nickel chloride ($NiCl_2.6H_2O$) and other appropriate reagents were mixed in a beaker by mechanical stirring for 1 h. The mixture was, then, poured into a Teflon-lined stainless steel autoclave which is placed in a reaction chamber kept at 180 °C for one day. Finally, the NiX (X=O/S/Se) was collected and dried in hot air oven for 12 h at 60 °C. For NiO synthesis, the other reagent used was 0.5 M NaOH solution; for NiS, it was 0.5 M aqueous sodium sulphide ($Na_2S$) solution; and for NiSe, it was sodium selenite ($Na_2SeO_3$) solution. Hydrazine hydrate ($N_2H_6O$) was used to reduce the $SeO_3^{2-}$. $Na_2SeO_3$ was used for Se source.

### *2.2.3. Electrochemical measurements*

Cyclic voltammetry (CV), potentio-dynamic stable polarization, constant potential chronoamperometry (CA), and AC impedance investigations were used to illustrate the electrocatalytic activities of the catalysts. The electrochemical measurements were conducted utilizing with a computer assisted potentiostat (AUTOLAB PG STAT 12, EcoChemic, Netherlands). All electrochemical experiments were pursued using Ag/AgCl/KCl reference electrodes (saturated aqueous solution). In each electrochemical study, a large Pt-foil (0.01 m × 0.01 m) was used as an auxiliary electrode. The working electrode was a planar graphite carbon electrode having area of $12 \times 10^{-6}$ $m^2$. The working electrode was prepared by sonication of 51.2 mg of catalyst dust in 1.0 mL ethanol for 30 min to form an almost homogeneous mixture. An aliquot of 10 μL of the dispersion was, then, drop cast on the carbon electrode followed by drying at room temperature (25 °C). Then, 5 μL nafion solution (1.0 mass %) was cast on the electrode followed by drying again. Cyclic voltammogram of each electrode was registered by immersing the electrodes in 1.0 M KOH solution and using the potential range from –0.9 V to 2.0 V at the scan rate of 50 mV/s for OER. For HER, the electrodes were dipped in 0.5 M $H_2SO_4$ solution and CV study was executed in the potential range of 0 to –1.5 V. Calibration of all the potentials with respect to Ag/AgCl,Cl electrodes was performed with respect to reversible hydrogen electrode (RHE) using the Nernst equation,

$$E_{RHE} = E_{Ag/AgCl/Cl^-} + (0.1976 + 0.059pH)\ V \qquad (2.1)$$

The value of overpotential (η) was estimated by the following equation,

$$\eta = E_{RHE} - 1.23\ V \qquad (2.\ 2)$$

To determine the Tafel slope, the well-known form Tafel equation was used.

$$\eta = a + b \log j \qquad (2.\ 3)$$

Using the Tafel slope (b), the constant (a), and the Ag/AgCl, Cl electrodes as the reference, all potentials were calibrated with regard to the reversible hydrogen electrode (RHE). Under static conditions, controlled potential electrolysis was also carried out.

The cyclic voltammogram was used to compute the turnover frequency (TOF) using the formula TOF= I/nFm, where I is the current (A), F is the Faraday constant, and m is the number of catalyst moles. The turnover frequency was also determined from the chronoamperometry profile using the formula, TOF=Q/nt, where n is the number of electrons transferred during the related electrochemical process and Q is the total charge spent.

## 2.3. Results and discussion

### *2.3.1. Structural characterization*

Powder X-Ray diffraction (XRD) was used to analyze the crystalline structures of as-synthesized electrocatalysts. XRD profile of NiO, NiS and NiSe nanoparticles are displayed in Fig.1. The X-ray diffractogram of NiO nanoparticles exhibits the diffraction peaks having 2θ values of 38.29°, 42.02°, 52.36° and 73.27°, which correspond to the planes (111), (200), (311) and (222) respectively, the diffraction pattern being correspond to the cubic phase of NiO nanocatalysts (JCPDS card number: 04-0835).The diffraction peaks observed for as-synthesized hexagonal NiS nanoparticles containing 2θ values of 31.05°, 38.40°, 49.26° and 55.16° corresponding to planes (100), (101), (102) and (110) (JCPDS card number: 02-1280).The hexagonal NiSe nanoparticles containing diffraction peaks having 2θ values 33.32°, 44.94°, 50.77° and 62.09° correspond to planes (101), (102), (110) and (103) (JCPDS card number: 18-0888). The average crystallite size of the nanoparticles was determined from the peak width at half maximum and is found 15.0 nm for NiO, 16.36 nm for NiS and 16.05 nm for NiSe by the Debye-Scherrer equation. Since the crystallite size does not differ much among the three NiX compounds, it can be anticipated that the difference in catalytic activity arises be a more from the nature of the materials rather than their exposed area.

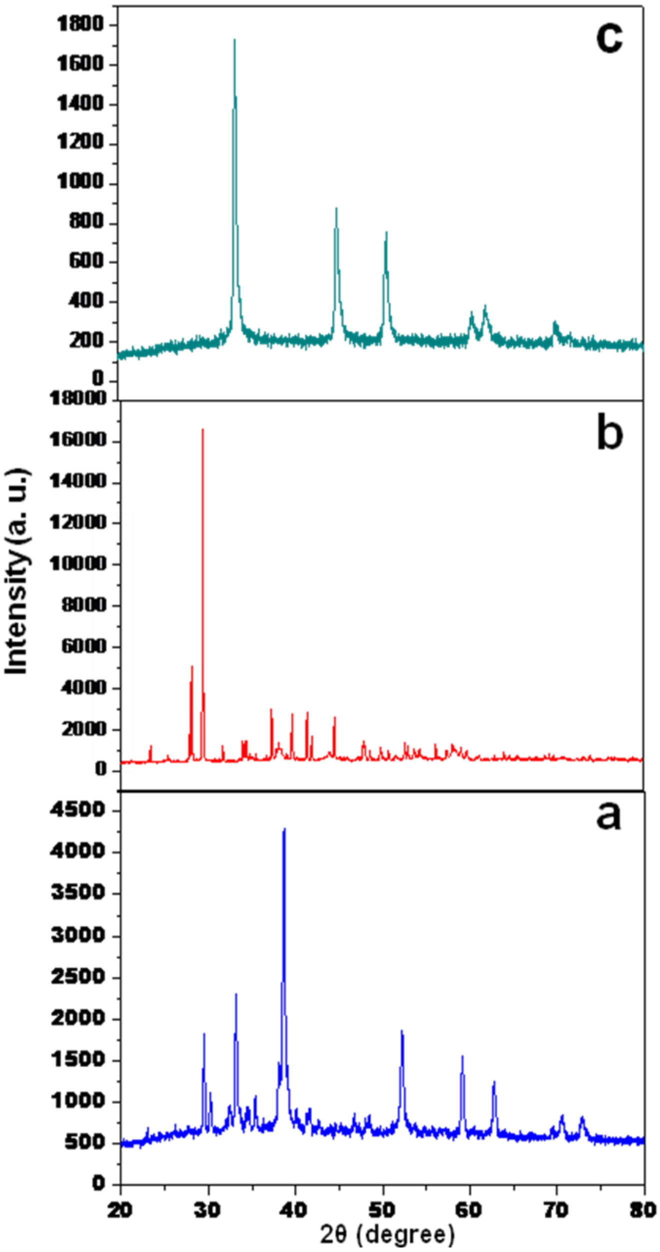

**Fig. 2.1.** X-ray diffraction patterns of (a) NiO, (b) NiS and (c) NiSe electrocatalysts

Fourier transform infrared spectroscopy has been used to study the nature of the functional groups of the produced NiX electrocatalysts. Fig. 2.2 displays the FTIR spectra of NiO, NiS, and NiSe nanoparticles. A broad band is observed at around 3436 $cm^{-1}$, which can be attributed to the stretching vibration of the X–H group. This vibration may arise as a result of a hydrogen bond with the X atom in all three circumstances. The

FTIR spectra of the series samples show a peak at 1085 $cm^{-1}$, which is significantly more intense for NiS. This peak is linked to the stretching vibration of the C–O of adsorbed $CO_2$. The position of absorption maximum of NiO is at 633 $cm^{-1}$. A strong band is seen at 425 $cm^{-1}$corresponding to the vibration of Ni–O bond in NiO nanoparticles. A broad peak located at 611-602 $cm^{-1}$ is indicative of the metal-sulfur bond (Ni-S) bending vibration. The vibrational mode composition of Se-O bonds determines the broad band at 578 $cm^{-1}$.

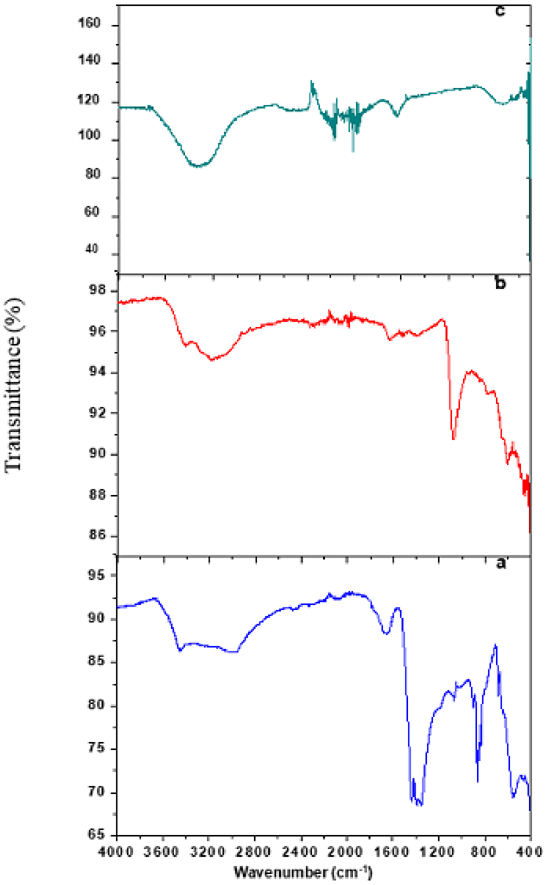

**Fig. 2.2.** Fourier transform infrared spectra of (a) NiO, (b) NiS and (c) NiSe electrocatalysts

The morphological characteristics at the surface of an electrocatalyst have an important role on its activity. Scanning electron micrographs of NiO, NiS and NiSe electrocatalysts are depicted in Fig. 2.3. The particles of NiSe consists of assemblage of small thin sheets generating numerous edges for the reaction. The gaps between the sheets are advantageous for molecular movements of the reactants and products. Synthesized NiS consists of rough sheets, bumps and rods of about 100 nm to 200 nm diameter. Holes and cracks are helpful for the movement of reactants and products. Particles of NiO consist of large brick and bump-like structure of about 500 nm thickness along with rods of about 100 nm diameter. Among different structures, there are gaps through which the reactants can penetrate and gases can be escaped. The EDS spectra indicate that the atomic composition of Ni:O = 50:50 for NiO, Ni:S= 54:47 for NiS and Ni:Se = 57:43 for NiSe. This indicates slight less of chalcogns of higher mass number according to the order: Se>S, during preparations of chalcogenides. It reflects plausibly the bond strengths of chalcogenides according to the expected order: NiO>NiS> NiSe.

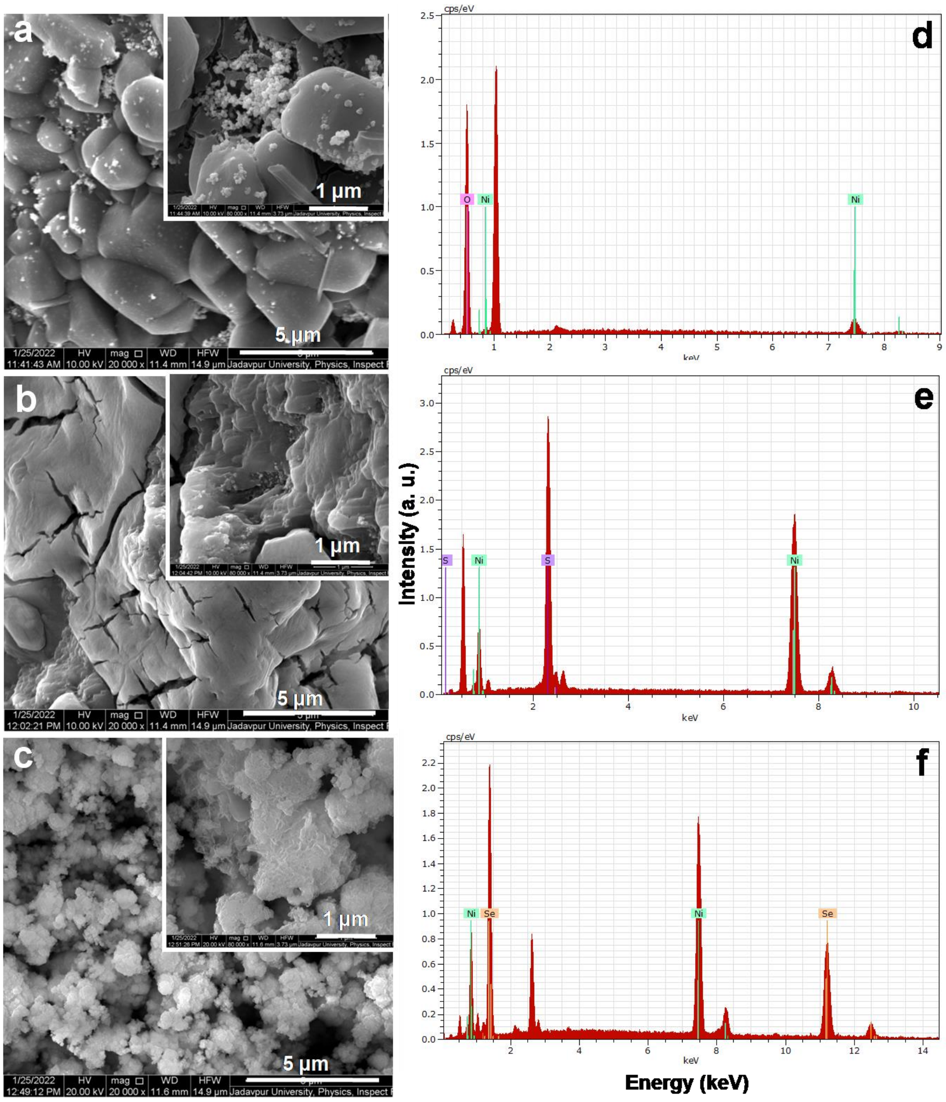

**Fig. 2.3**. (a, b, c) Scanning electron micrographs and (d, e, f) energy dispersive X-ray spectra of NiO, NiS and NiSe electrocatalysts, respectively.

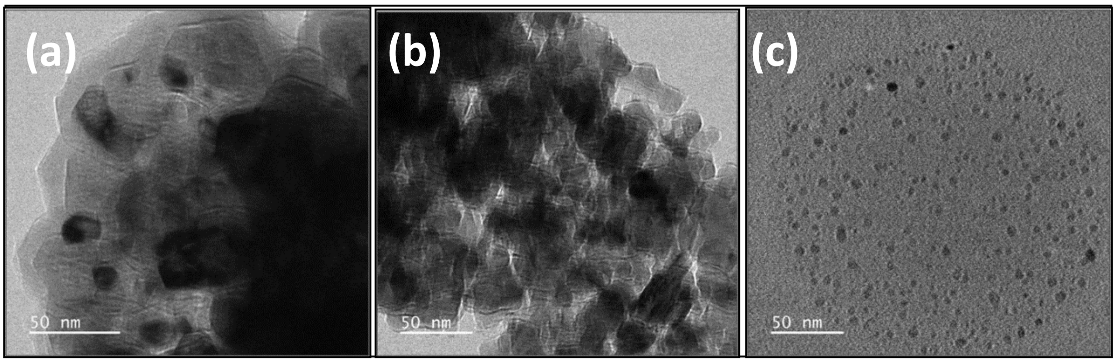

**Fig. 2.4.** Transmission electron micrographs of (a) NiO, (b) NiS and (c) NiSe nanoparticles, respectively.

Transmission electron micrographs of (a) NiO, (b) NiS and (c) NiSe electrocatalysts, respectively have been shown in Fig. 2.4. It is seen that NiO possesses nanocuboid-like structure, NiS is nanospherical structure and NiSe is quantum dot like structure. The average diameter of NiO, NiS, and NiSe, nanoparticles are 24±4 nm, 16±2.7, and 8±1.5 nm, respectively. Due to decrease in size, surface area increases that facilitate better absorption of ions for NiSe in comparison with NiO and NiS electrocatalysts.

### *2.3.2. Electrochemical studies*

Electrochemical studies have been carried out to study the decomposition of water of NiO, NiS and NiSe, NiS and NiSe nanoparticles by cyclic voltammetry in 1.0 M KOH and 0.5 M $H_2SO_4$ solution at a scan rate of 5 mV $s^{-1}$. Fig. 2.5 depicts the cyclic

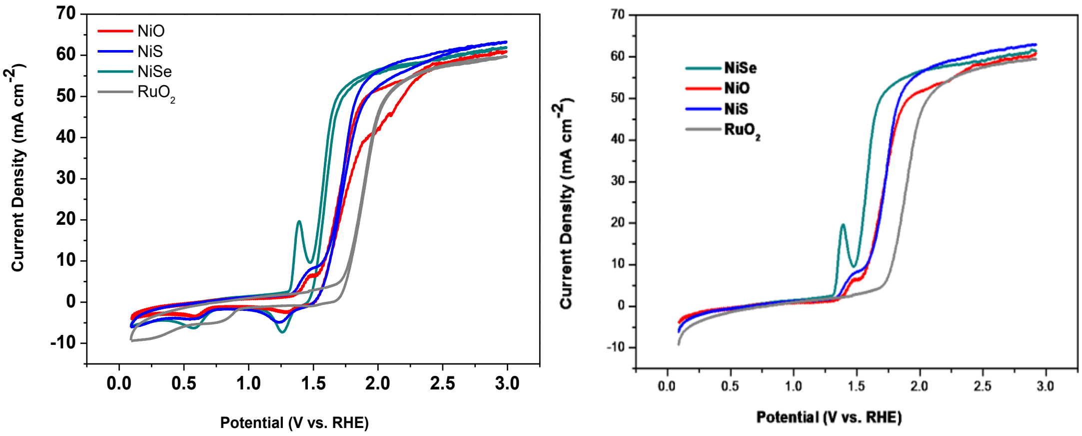

**Fig. 2.5**. (left) Cyclic voltammograms and (right) linear sweep voltammetry in 1.0 M KOH solution for NiO, NiS and NiSe electrocatalysts

voltammograms of NiX (X=O/S/Se) for oxygen evolution reaction. These exhibit initial slow increase of current density followed by one oxidation peak and then, sharp increase of current density in the forward scan of potential that corresponds to water oxidation. The initial slow increase of current density without any apparent peak is due to the oxidation Ni from metallic (zero) state to $Ni^{I}$ and $Ni^{II}$ [45]. The only forward peak and the corresponding reverse peak during backward scan arise due to the formation of NiXOH (X= (O/S/Se) ($Ni^{III}$ state) from NiX and the reverse corresponding to the interconversion of NiOOH for NiO electrode [51]. The onset overpotential (mV) of water splitting oxygen evolution reaction on NiO electrode is much higher than that of NiS and NiS eelectrocatalysts. The value for NiSe is less than the $NiSe_x$ catalysts deposited on Ni-foam electrode [52]. Because of the increased catalytic activity of NiSe deposited electrode, its overpotential (mV) at 10 mA $cm^{-2}$ current density is much lower than that of NiO and NiS based electrocatalysts. The observed overpotential for the as-synthesized NiSe, NiS, NiO and $RuO_2$ electrocatalysts at 10 mA $cm^{-2}$ current density are 259, 329, 355, 549.8 mV, respectively. At a current density of 50 mA $cm^{-2}$, the overpotential for NiO, NiS, and NiSe deposited electrodes are 654, 581, and 434 mV, respectively. All these data reveals that the order of electrocatalytic activity of the as-synthesized catalysts is NiSe >NiS>NiO> $RuO_2$.

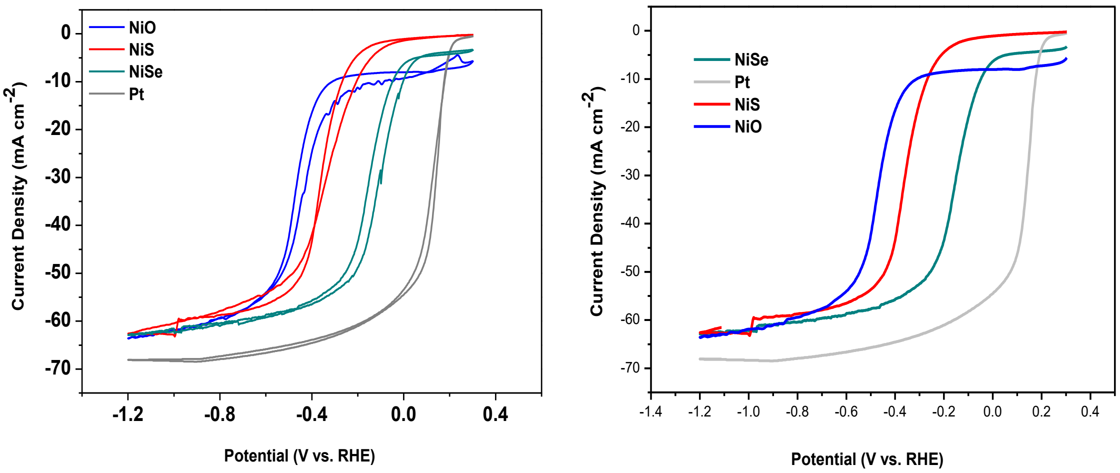

**Fig. 2.6.** (left) Cyclic voltammograms and (right) linear sweep voltammetry obtained in 0.5 M $H_2SO_4$ solution for NiO, NiS and NiSe electrocatalysts

The cyclic voltammograms for HER on NiX/C electrodes (X=O/S/Se) immersed in 0.5 M $H_2SO_4$ solution, were presented in Fig. 2.6. The curves are well separated from each other indicating distinct catalytic difference. The final currents at −1.2 V are little different from each other indicating almost same diffusion-controlled limiting current situation for the electrodes. The overpotentials at 10 mA cm$^{-2}$ current density for HER on NiO, NiS, NiSe and Pt electrocatalysts are 312, 269, 49.5 and 17.9 mV respectively and the overpotentials at 50 mA cm$^{-2}$ current density are 549.4, 449.3 and 214.1 mV respectively for the chalcogenides. This reveals that Pt is the best in electrocatalytic activity among the studied materials and NiSe among the chalcogenides.

To understand the electrode kinetics further, the slope obtained from the Tafel plot has been analysed. Tafel plots (η *vs.* log j) for NiO, NiS, and NiSe for HER in 0.5 M $H_2SO_4$ solution are presented in Fig. 2.7. The Tafel slopes has been calculated for the overall reaction kinetics of OER at the same chemical environment are 125, 81 and 70 mV dec$^{-1}$ for NiO, NiS and NiSe respectively, as have been shown in Table 2.1. It is also

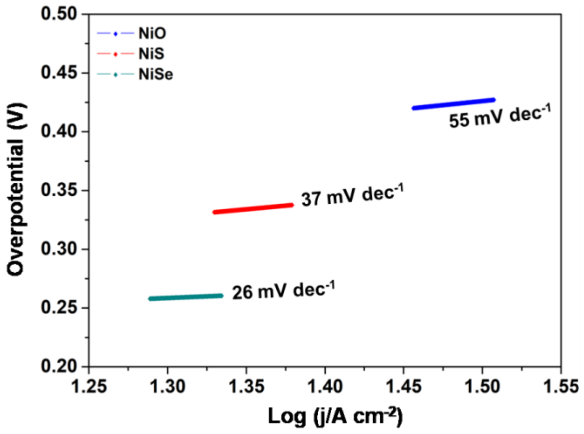

**Fig. 2.7.** Tafel plots obtained for NiO, NiS and NiSe electrocatalysts for HER in 0.5 M $H_2SO_4$ solution

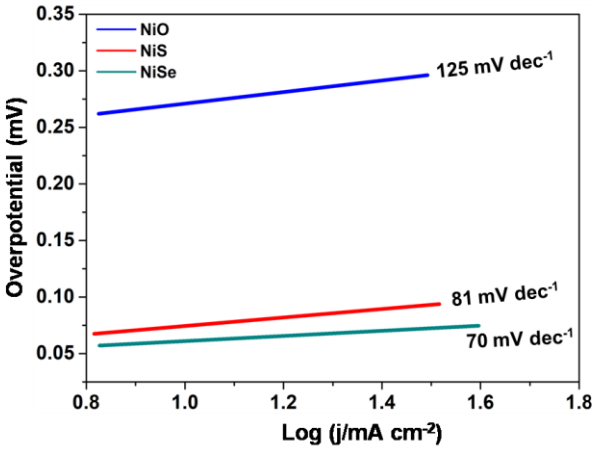

**Fig. 2.8.** Tafel plots obtained for NiO, NiS and NiSe electrocatalysts in 1.0 M KOH solution

observed that the Tafel slope of more conducting $Ni_3S_2/MoS_x$ nanosheets is almost similar (67.5 mV $dec^{-1}$) in alkali [48].

Tafel plots (η *vs.* log j) for NiO, NiS, and NiSe for HER in 1.0 M KOH solution are presented in Fig. 2.8. The experimental Tafel slopes for the HER on the NiO, NiS and NiSe electrocatalystsare 55, 37 and 26 mV $dec^{-1}$, respectively. It illustrates the better catalytic properties of NiX upon going down the group XVI element (X) in the periodic table.

The frequency dispersive electrochemical impedance spectroscopy has been performed to determine the charge transfer resistance ($R_{ct}$), solution resistance ($R_s$), and capacitances ($C_{ct}$); Nyquist plots of the electrocatalysts have been compared in Fig. 2.9. A simple electrochemical system is assumed consisting of solution resistance inseries combination with resistor and a capacitor in parallel, which correspond to the polarization resistance and capacitance of the double layer, respectively and the presentation is called Randles circuit model. From the model, at high frequencies, the impedance of the electrochemical cell corresponding to the point, where the semicircle intersects at *x*-axis, is produced by Ohmic resistance, $R_s$. The charge transfer resistance ($R_{ct}$) has been measured by taking the diameter of the semicircle into consideration at the relatively low frequency region of the plot. The charge transfer resistance of NiSe is lowered and the capacitance which is a measure of the extent of adsorption on the electrodes is higher than the other two electrocatalysts NiO and NiS and for these reasons, its electrocatalytic

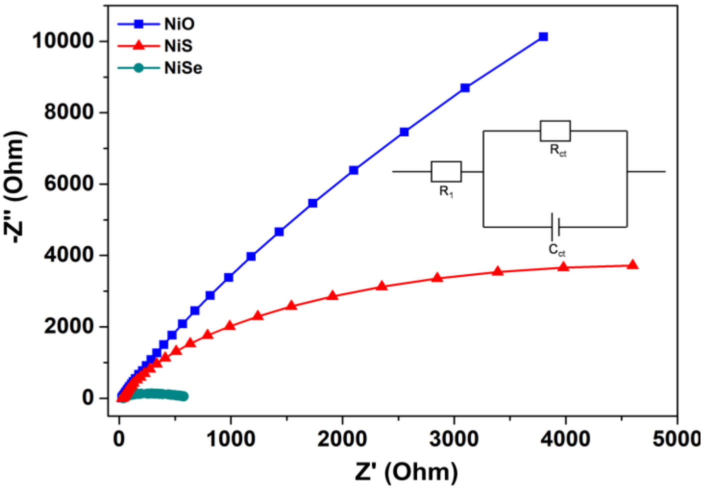

**Fig. 2.9.** Nyquist plots corresponding to the electrocatalysts NiO, NiS and NiSe in 1.0 M KOH solution

performance is better than other two electrocatalysts. The Randles circuit parameters of the NiO, NiS and NiSe electrocatalysts are shown in Table 2.1.

**Table 2.1.** Randles circuit parameters of the electrocatalysts

| Sample | $R_s$ (Ω) | $R_{ct}$ (Ω) | $C_{ct}$ (μF) |
|---|---|---|---|
| NiO | 26.82 | 164900 | 2.39 |
| NiS | 62.33 | 16600 | 3.22 |
| NiSe | 30.87 | 8445 | 3.86 |

To study the steady state behavior of different Ni based electrocatalysts, controlled potential electrolysis (chronoamperometry, CA) measurements have been carried out at a potential of 0.4 V for 1200 s in a solution of 1.0 M KOH for OER. For HER, 0.5 M $H_2SO_4$ solution and -0.4 V constant potential were used. The profile is depicted in Fig. 2.10. All catalysts reveal typical profiles of initial decrease of current density with time followed by almost constancy in current for OER and HER, with the order of electrocatalytic activity in the sequence: NiSe >NiS>NiO for both cases. All catalysts exhibit consistent steady current density after 1200 s indicating their possible applications as practical catalysts.

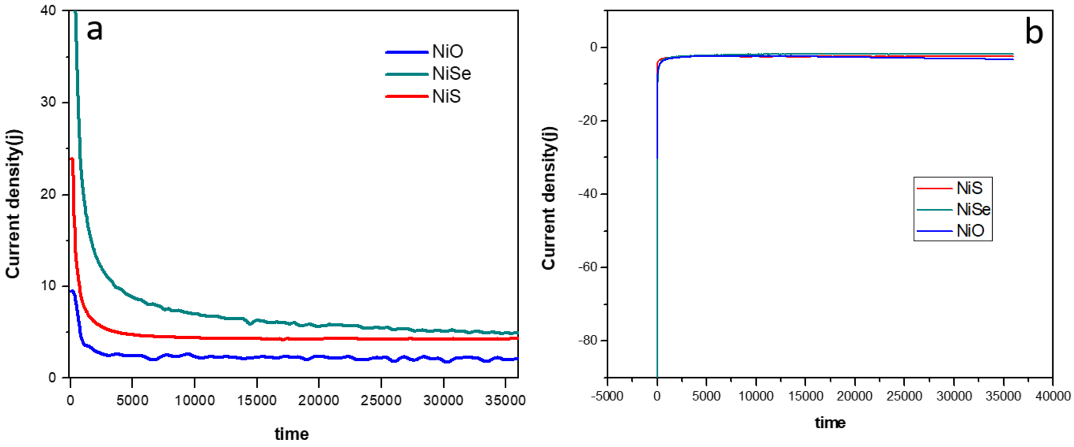

**Fig. 2.10.** Chronoamperommetry study of electrocatalysts in (a) 1.0 M KOH and (b) 0.5 M $H_2SO_4$ solution

Fig. 2.11 depicts the cyclic voltammograms of three electrodes in non-Faradaic regions at different scan rates of 10, 20, 50, 70, 90 and 100 mV $s^{-1}$ in 1.0 M KOH solution. The order of $C_{dl}$ values obtained from the study is NiSe>NiS>NiO at all the scan rates.The

$C_{dl}$ values are dependent on the catalytically active sites of the electrocatalysts. The higher $C_{dl}$ value indicates a larger ECSA in the electrochemical reaction, which improves the catalytic activity.

Thus, the ECSA which is proportional to the double layer capacitance, is a measure of the number of active catalytic sites in the electrocatalysts and hence, their activity [53]. The values of double layer capacitance $C_{dl}$ of NiO, NiS and NiSe are 2.72, 3.04, 3.94 µF cm$^{-2}$, respectively. The ratio of the capacities of the as-synthesized nickel chalcogenides (NiO: NiS: NiSe = 2.72: 3.04: 3.94) indicates the order of their real active surface area and the reaction sites of the system of catalysts.The electrochemical active surface area of the electrocatalysts NiO, NiS and NiSe are 6.8, 7.6 and 9.8 cm$^{-2}$ respectivelyBut the current densities of the materials are much higher at a given potential. The ratio of the chrono amperometric current densities of NiX materials at 0.8 V for OER after 20 min is NiO: NiS: NiSe =0.102: 0.54: 0.75. Similar ratio of current density at -0.4 V for HER is NiO: NiS: NiSe =0.0042: 0.0272: 0.413.

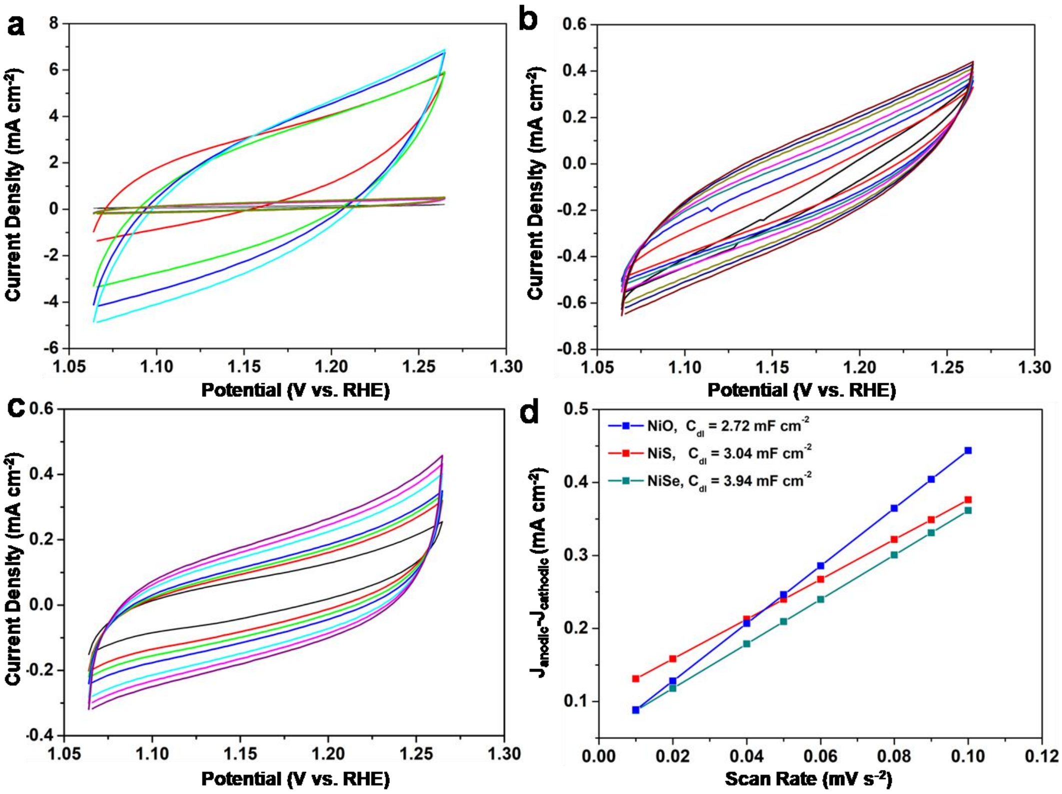

**Fig. 2.11.** Cyclic voltammogramms of the (a) NiSe, (b) NiS, and (c) NiO electrodes at different scan rates of 10, 20, 40, 50, 60, 80, 100 mV s$^{-1}$; and (d) display of scan rate dependences of the current densities for measurements of double layer capacitance of the electrocatalysts.

These data indicates that the material characteristics are the prime factor for increased catalytic activity of nickel chalcogenides, the activity of which is increased upon going down the periodic table, besides slight morphological improvements.

From the entire study, a plausible mechanism for the OER under alkaline medium can be proposed as follows:

1) $OH^{-} + NiX \rightarrow NiXOH + e^{-}$
2) $NiXOH + OH^{-} \rightarrow NiXO + H_2O + e^{-}$
3) $NiXO + NiXO \rightarrow 2NiX + O_2$

The process may also proceed with the slight less of $X^{-}$ and the formation of NiOOH by following the equation,

4) $NiXOH + 2OH^{-} \rightarrow NiOOH + H_2O + X^{-}$
5) $NiX + NiOOH \rightarrow Ni + O_2 + H_2O$

where NiX represents the active sites which might be NiO/NiS/NiSe. The OER must occur after generation of $Ni^{III}$ state as evident from Fig. 2.5. The initial adsorption of $OH^{-}$ on Ni of NiX is found to be relatively more on NiSe than the other two electrocatalysts. It is plausible that it has greater size and polarizability than others and thus, greater delocalization of charge is possible around it. Therefore, the peak potential for generation of $Ni^{III}$ species is lower for NiSe (1.38 V) than that of NiS (1.46 V) and NiO (1.48 V) and hence, the electrocatalytic activity is greater for NiSe. Moreover, as the electronegativity of X varies in the order: O>S=Se, the desorption of NiXO to form $O_2$ in the 3rd step is gradually difficult in the sequence $NiSeO<NiSO<NiO_2$. Therefore, oxygen evolution is more with the NiSe deposited electrode.

Studies have been conducted to reveal the mechanism of hydrogen evolution reaction. The first step of the reaction is the discharge step:

1) $NiX + H_3O^{+} + e\,(M) \rightarrow (NiX){-}H + H_2O$ (Volmer)

Then next step is either

2) $(NiX){-}H + (NiX){-}H = 2\,NiX + H_2$ (Tafel)
3) $(NiX){-}H + H_3O^{+} + e \rightarrow 2NiX + H_2O + H_2$ (Heyrovsky)

Since X is more electronegative than Ni and X contains lone pair of electrons, the bonding of $H^{+}$ is expected to take place through X rather than Ni. Moreover as the H-X bond strength is expected to be more in the order O-H>S-H>Se-H as the metallic character increases and the electronegativity decreases in going down the periodic table, the adsorption of hydrogen on NiX will be in the sequence NiO>NiS>NiSe. Since, the electrocatalytic activity of NiX follows the exact reverse trends, it indicates that the desorption (either step 2 or 3) is the rate determining for the system of catalyst materials. The value for NiSe is less than the $NiSe_x$ catalysts deposited on Ni-foam electrode [52] as presented in Table 2.2. The smallest value corresponding to the Tafel slope of NiSe electrode indicates that it is more facile among the electrocatalysts studied for HER. Considering the symmetry factor = ½, the expected values of the Tafel slope is 29 and 77 mV for Tafel and Heyrovsky steps being rate determining [54]. In this respect, both chalcogenides NiS and NiSe follow the step 2 as rate determining step whereas NiO on which HER occurs at relatively high potential seems to follow step 3 as the rate determining step. Therefore, the bond strength of NiX is expected to vary in the order NiO>NiS>NiSe.

**Table 2.2. A comparative account of electrochemical performance towards OER**

| Electrocatalyst | Electrolyte | Overpotential of OER | Tafel slope (mV $dec^{-1}$) | Reference |
|---|---|---|---|---|
| NiO | 1 M KOH | 340 mV@onset<br>355 mV@10mA$cm^{-2}$<br>654 mV@50mA$cm^{-2}$ | 125 | Present work |
| NiS | 1 M KOH | 309 mV@onset<br>329 mV@10mA$cm^{-2}$<br>581 mV@50mA$cm^{-2}$ | 81 | Present work |
| NiO | 1 M KOH | 400 mV@40mA$cm^{-2}$ | 70 | 21 |
| NiS | 1 M KOH | 220 mV@40mA$cm^{-2}$ | 65 | 21 |
| NiO/NiS | 1 M KOH | 209 mV@40mA$cm^{-2}$ | 60 | 21 |
| NiS | 1 M KOH | 430 mV@10mA$cm^{-2}$ | 101 | 51 |
| N-NiMoS | 1 M KOH | 1.54 mV@10mA$cm^{-2}$ | 46 | 53 |
| $Ni_3Se_2$ | 1 M KOH | 310 mV@onset | 97.1 | 54 |
| $Ni_{0.85}Se$ | 1 M KOH | 450 mV@onset | 120 | 55 |
| NiSe/NF | 1 M KOH | 329 mV@20mA$cm^{-2}$ | 110 | 47 |

| | | | | |
|---|---|---|---|---|
| NiSe | 1 M KOH | 328 mV@50mAcm$^{-2}$ | 72.2 | 56 |
| NiSe | 1 M KOH | 230 mV@onset<br>259 mV@10mAcm$^{-2}$<br>434 mV@50mAcm$^{-2}$ | 70 | Present work |

The performance of the present NiSe based electrode with other benchmark Ni based electrode for OER [55−62] is presented in Table 2.2. The performance is almost same when onset potential is considered but different when overpotential at a particular current density (say, 10 mA cm$^{-2}$) has been taken into consideration. In respect to these references, the electrode generated in the present experiment is better than some other electrodes but worse with respect to some others [21], the greater overpotential in the present experiment with respect to that arises plausibly because of less loading of catalyst (0.625 mg cm$^{-2}$) with respect to the (0.426× 10$^{-2}$ mg cm$^{-2}$) (as computed from their report). On the other hand, the performance of NiSe based electrode is very high for HER with respect to that in the literature as found in Table 2.3.

**Table 2.3. A comparative account of electrochemical performance towards hydrogen evolution reaction**

| Electrocatalyst | Electrolyte | Overpotential of HER | Tafel slope (mV dec$^{-1}$) | Reference |
|---|---|---|---|---|
| NiO | 0.5 M $H_2SO_4$ | 203 mV@onset<br>312 mV@10mAcm$^{-2}$<br>549.4 mV@50mAcm$^{-2}$ | 55 | Present work |
| NiS | 0.5 M $H_2SO_4$ | 151 mV@onset<br>269 mV@10mAcm$^{-2}$<br>449.3 mV@50mAcm$^{-2}$ | 37 | Present work |
| NiS | 1 M KOH | 430 mV@10mA cm$^{-2}$ | 130 | 51 |
| $NiSe_2$ | 0.5 M $H_2SO_4$ | 156 mV@10 mAcm$^{-2}$ | 54 | 52 |
| $NiSe_2$ | 1 M KOH | 164 mV@10 mAcm$^{-2}$ | 96 | 52 |

| | | | | |
|---|---|---|---|---|
| NiSe | 1 M KOH | 153 mV@10mA $cm^{-2}$ | 99 | 47 |
| NiSe | 1 M KOH | 198 mV@10mA$cm^{-2}$ | 115.7 | 56 |
| NiSe | 0.5 M $H_2SO_4$ | 31.23 mV@onset<br>49.5 mV@10mA$cm^{-2}$<br>214.1 mV@50mA$cm^{-2}$ | 26 | Present work |

## 2.4. Conclusions

The NiO, NiS and NiSe catalysts ware synthesized by utilizing similar one-pot hydrothermal method. The order of electrocatalytic activities corresponding to the both hydrogen and oxygen evolution reactions are NiSe>NiS>NiO. In both cases, NiSe electrocatalysts exhibit an excellent electrocatalytic activity and stability. The activity order has been related to suitable physicochemical characteristics along with increased ECSA values of NiSe compared to others and the characteristics of the rate determining step of the reactions.

## References

[1] Z. Zou, X. Wang, J. Huang, Z. Wu, F. Gao, An Fe-doped nickel selenide nanorod/nanosheet hierarchical array for efficient overall water splitting, J. Mater. Chem. A 7 (2019) 2233–2241.

[2] Z. L. Chen, H. L. Qing, K. Zhou, D. L. Sun, R. B. Wu, Metal-organic framework-derived nano composites for electrocatalytic hydrogen evolution reaction, Prog. Mater. Sci. 108 (2020) 100618 1–49.

[3] W. Zhu, W. Chen, H. Yu, Y. Zeng, F. Ming, H. Liang, Z. Wang, NiCo/NiCo-OH and NiFe/NiFe-OH core shell nanostructures for water splitting electrocatalysis at large currents, Appl. Catal. B 278 (2020) 119326 1–9.

[4] Y. Zhao, J. Zhang, Y. Xie, B. Sun, J. Jiang, W. J. Jiang, S. Xi, H. Y. Yang, K. Yan, S. Wang, X. Guo, P. Li, Z. Han, X. Lu, H. Liu, G. Wang, Constructing atomic heterometallic sites in ultrathin nickel-incorporated cobalt phosphide

nanosheets via a boron-assisted strategy for highly efficient water splitting, Nano Lett. 21 (2021) 8231–832.

[5] Z. Zhou, Z. Pei, L. Wei, S. Zhao, X. Jian, Y. Chen, Electrocatalytic hydrogen evolution under neutral pH conditions: current understandings, recent advances, and future prospects, Energy Environ. Sci. 13 (2020) 3185–3206.

[6] X. L. Wang, Y. J. Tang, W. Huang, C. H. Liu, L. Z. Dong, S. L. Li, Y. Q. Lan, Efficient electrocatalyst for the hydrogen evolutionreaction derived from polyoxotungstate/polypyrrole/grapheme, ChemSusChem. 10 (2017) 2402–2407.

[7] T. E. Mallouk, Water electrolysis: divide and conquer, Nat. Chem. 5 (2013) 362–363.

[8] P. Zhang, X. Sheng, X. Chen, Z. Fang, J. Jiang, M. Wang, F. Li, L. Fan, Y. Ren, B. Zhang, B. J. J. Timmer, M. S. G. Ahlquist, L. Sun, Paired electrocatalytic oxygenation and hydrogenation of organic substrates with water as the oxygen and hydrogen source, Angew. Chem. Int. Ed. 58 (2019) 9155−9159.

[9] E. J. Popczun, J. R. McKone, C.G. Read, A. J. Biacchi, A. M. Wiltrout, N. S. Lewis, R. E. Schaak, Nanostructured nickel phosphide as an electrocatalyst for the hydrogen evolution reaction, J. Am. Chem. Soc. 135 (2013) 9267−9270.

[10] X. Wang, Y. V. Kolen'ko, X. Q. Bao, K. Kovnir, L. Liu, One step synthesis of self-supported nickel phosphide nanosheet array cathodes for efficient electrocatalytic hydrogen generation, Angew. Chem. Int. Ed. 54 (2015) 8188−8192.

[11] Z. Huang, Z. Chen, Z. Chen, C. Lv, H. Meng, C. Zhang, $Ni_{12}P_5$ nanoparticles as an efficient catalyst for hydrogen generation via electrolysis and photoelectrolysis, ACS Nano 8 (2014) 8121–8129.

[12] J. Tian, Q. Liu, A. M. Asiri, X. Sun, Self-supported nanoporous cobalt phosphide nanowire arrays: an efficient 3D hydrogen-evolving cathode over the wide range of pH 0−14, J. Am. Chem. Soc.136 (2014) 7587−7590.

[13] M. Ma, G. Zhu, F. Xie, F. Qu, Z. Liu, G. Du, A. M. Asiri, Y. Yao, X. Sun, Homologous catalysts based on fe-doped cop nanoarrays for high-performance full water splitting under benign conditions, ChemSusChem 10 (2017) 3188−3192.

[14] M. Liu, R. Zhang, L. Zhang, D. Liu, S. Hao, G. Du, A. M. Asiri, R. Kong, X. Sun, Energy-efficient electrolytic hydrogen generation using a $Cu_3P$ nanoarray as a bifunctional catalyst for hydrazine oxidation and water reduction, Inorg. Chem. Front. 4 (2017) 420−423.

[15] Y. H. Chang, C. T. Lin, T. Y. Chen, C. L. Hsu, Y. H. Lee, W. Zhang, K. H. Wei, L. J. Li, Highly efficient electrocatalytic hydrogen production by MoS(x) grown on graphene-protected 3D Ni foams, Adv. Mater. 25 (2013) 756−760.

[16] J. Zhang, X. Wu, W.-C. Cheong, W. Chen, R. Lin, J. Li, L. Zheng, W. Yan, L. Gu, C. Chen, Q. Peng, D. Wang, Y. Li, Cation vacancy stabilization of single-atomic-site Pt1/Ni(OH)x catalyst for diboration of alkynes and alkenes, Nat. Commun. 9 (2018) 1002 1–9.

[17] D. A. Bulushev, M. Zacharska, A. S. Lisitsyn, O. Y. Podyacheva, F. S. Hage, Q. M. Ramasse, U. Bangert, L. G. Bulusheva, Single atoms of Pt-group metals stabilized by N-doped carbon nanofibers for efficient hydrogen production from formic acid, ACS Catal. 6 (2016) 3442–3451.

[18] L. Wang, W. Zhang, S. Wang, Z. Gao, Z. Luo, X. Wang, R. Zeng, A. Li, H. Li, M. Wang, X. Zheng, J. Zhu, W. Zhang, C. Ma, R. Si, J. Zeng, Atomic-level insights in optimizing reaction paths for hydroformylation reaction over Rh/CoO single-atom catalyst, Nat. Commun.7 (2016) 14036 1–8.

[19] C. Cheng, S. S. A. Shah, T. Najam, X. Qi, Z. Wei, Improving the electrocatalytic activity for hydrogen evolution reaction by lowering the electrochemical impedance of $RuO_2$/NiP, Electrochim. Acta 260 (2018) 358–364.

[20] E. Tsuji, A. Imanishi, K. I. Fukui, Y. Nakato, Electrocatalytic activity of amorphous $RuO_2$ electrode for oxygen evolution in an aqueous solution, Electrochim. Acta. 56 (2011) 2009–2016.

[21] N. A. Khan, N. Rashid, M. Junaid, M. N. Zafar, M. Faheem, I. Ahmad, NiO/NiS heterostructures: An efficient and stable electrocatalyst for oxygen evolution reaction, ACS Appl. Energy Mater. 2 (2019) 3587–3594.

[22] E. J. Popczun, J. R. McKone, C. G. Read, A. J. Biacchi, A. M. Wiltrout, N. S. Lewis, R. E. Schaak, Nanostructured nickel phosphide as an electrocatalyst for the hydrogen evolution reaction, J. Am. Chem. Soc. 135 (2013) 9267−9270.

[23] A. Goyal, S. Louisia, P. Moerland, M. T. M. Koper, Cooperative effect of cations and catalyst structure in tuning alkaline hydrogen evolution on Pt electrodes, J. Am. Chem. Soc. 146(2024) 7305–7312.

[24] Z. Huang, Z. Chen, Z. Chen, C. Lv, H. Meng, C. Zhang, $Ni_{12}P_5$ nanoparticles as an efficient catalyst for hydrogen generation via electrolysis and photoelectrolysis, ACS Nano 8 (2014) 8121–8129.

[25] C. Wu, Z. Li, S. Dong, K. Zhou, D. Ding, R. Liu, W. Pei Small-size intermetallic FeMnPt nanoparticles electrocatalyst for HER under acidic and alkaline conditions, ACS Appl. Nano Mater. 7 (2024) 8093–8101.

[26] M. Ma, G. Zhu, F. Xie, F. Qu, Z. Liu, G. Du, A. M. Asiri, Y. Yao, X. Sun, Homologous catalysts based on Fe-doped CoP nanoarrays for high-performance full water splitting under benign conditions, ChemSusChem 10 (2017) 3188–3192.

[27] M. Liu, R. Zhang, L. Zhang, D. Liu, S. Hao, G. Du, A. M. Asiri, R. Kong, X. Sun, Energy-efficient electrolytic hydrogen generation using a $Cu_3P$ nanoarray as a bifunctional catalyst for hydrazine oxidation and water reduction, Inorg. Chem. Front. 4 (2017) 420–423.

[28] Y.H. Chang, C. T. Lin, T. Y. Chen, C. L. Hsu, Y. H. Lee, W. Zhang, K. H. Wei, L. J. Li, Highly efficient electrocatalytic hydrogen production by MoS(x) grown on graphene-protected 3D Ni foams, Adv. Mater. 25 (2013) 756−760.

[29] I. H. Kwak, H. S. Im, D. M. Jang, Y. W. Kim, K. Park, Y. R. Lim, E. H. Cha, J. Park, $CoSe_2$ and $NiSe_2$ nanocrystals as superior bifunctional catalysts for electrochemical and photoelectrochemical water splitting, ACS Appl. Mater. Interfaces 8 (2016) 5327−5334.

[30] X. Lu, C. Zhao, Electrodeposition of hierarchically structured three-dimensional nickel-iron electrodes for efficient oxygen evolution at high current densities, Nat. Commun. 6 (2015) 6616 1–7.

[31] X. F. Lu, L. F. GU, J. W. Wang, J. X. Wu, P. Q. Liao, G. R. Li, Bimetal-organic framework derived $CoFe_2O_4/C$ porous hybrid nanorod arrays as high-performance electrocatalysts for oxygen evolution reaction, Adv. Mater. 29 (2017) 16044371–7.

[32] J. Yang, G. Zhu, Y. Liu, J. Xia, Z. Ji, X. Shen, S. Wu, $Fe_3O_4$-decorated $Co_9S_8$ nanoparticles in situ grown on reduced graphene oxide: A new and efficient electrocatalyst for oxygen evolution reaction, Adv. Funct. Mater. 26 (2016) 4712−4721.

[33] A. Swesi, J. Masud, M. Nath, Nickel selenide as a high efficiency catalyst for oxygen evolution reaction, Energy Environ. Sci. 9 (2016) 1771−1782.

[34] Y. Li, H. Wang, L. Xie, Y. Liang, G. Hong, H. Dai, $MoS_2$ nanoparticles grown on graphene: An advanced catalyst for the hydrogen evolution reaction, J. Am. Chem. Soc. 133 (2011) 7296−7299.

[35] D. Liu, Q. Lu, Y. Luo, X. Sun, A. M. Asiri, $NiCo_2S_4$ nanowires array as an efficient bifunctional electrocatalyst for full water splitting with superior activity, Nanoscale 7 (2015) 15122−15126.

[36] Y. Bai, W. Shen, K. Song, S. Zhang, Y. Wang, T. Xu, J. Xu, S. Dai, X. Wang, Controlled synthesis of NiSe-$Ni_{0.85}Se$ nanocomposites for high-performance hybrid supercapacitors, J. Electroanal. Chem. 880 (2021) 1147951–7.

[37] Y. Tang, T. Chen, S. Yu, Y. Qiao, S. Mu, S. Zhang, Y. Zhao, L. Hou, W. Huang, F. Gao, A highly electronic conductive cobalt nickel sulphide dendrite/quasi-spherical nanocomposite for a super-capacitor electrode with ultrahigh areal specific capacitance, J. Power Sources 295 (2015) 314−322.

[38] Y. Li, X. Wu, L. Pang, Y. Miao, A. Ye, Y. Sui, J. Qi, F. Wei, Q. Meng, Y. He, Z. Zhan, Y. Ren, Z. Sun, Self-supported NiSe@$Ni_3S_2$ core-shell composite on Ni foam for a high-performance asymmetric supercapacitor, Ionics 26 (2020) 3997–4007.

[39] Q. Bao, J. Wu, L. Fan, J. Ge, J. Dong, J. Jia, J. Zeng, J. Lin, Electrodeposited $NiSe_2$ on carbon fiber cloth as a flexible electrode for high-performance supercapacitors, J. Energy Chem. 26 (2017) 1252–1259.

[40] H. Wu, Y. Wang, L. Zhang, Z. Chen, C. Wang, S. Fan, Comparison of two nickel selenides materials with different morphologies as counter electrodes in dye-sensitized solar cells, J. Alloys Compd. 745 (2018) 222–227.

[41] M. A. Airo, F. Otieno, L. Mxakaza, A. Ipadeola, R. S. Kadzutu-Sithole, L. F. Machogo-Phao, C. Billing, M. Moloto, N. Moloto, Probing the stoichiometry

dependent catalytic activity of nickel selenide counter electrodes in the redox reaction of iodide/triiodide electrolyte in dye sensitized solar cells, RSC Adv. 10 (2020) 39509–39520.

[42] H. Che, X. Liu, Y. Gao, J. Liu, Z. Cao, Hydrothermal electrochemical deposition synthesis $NiSe_2$ as efficient counter electrode materials for dye-sensitized solar cells, J. Alloys Compd. 705 (2017) 645–651.

[43] F. Gong, X. Xu, Z. Li, G. Zhou, Z. S. Wang, $NiSe_2$ as an efficient electrocatalyst for a Pt-free counter electrode of dye-sensitized solar cells, Chem. Commun. 49 (2013) 1437–1439.

[44] Y. Guo, C. Zhang, J. Zhang, K. Dastafkan, K. Wang, C. Zhao, Z. Shi, Metal─organic framework-derived bimetallic NiFe selenide electrocatalysts with multiple phases for efficient oxygen evolution reaction, ACS Sustainable Chem. Eng. 9 (2021) 2047−2056.

[45] H. Shengnan, W. Shiquan, F. Chuanqi, W. Huimin, Z. Jiujun, M. He, Novel MOF-derived nickel nitride as high-performance bifunctional electrocatalysts for hydrogen evolution and urea oxidation, ACS Sustainable Chem. Eng. 8 (2020) 7414−7422.

[46] A. Kelong, W. Qufu, D. A. Walid, MOF-Derived sulfide-based electrocatalyst and scaffold for boosted hydrogen production, ACS Appl. Mater. Interfaces. 12 (2020) 33595−33602.

[47] P. Bhanja, Y. Kim, B. Paul, J. Lin, S. M. Alshehri, T. Ahamad, Y. V. Kaneti, A. Bhaumik, Y. Yamauchi, Facile synthesis of nanoporous transition metal-based phosphates for oxygen evolution reaction, ChemCatChem. 12 (2020) 2091–2096.

[48] P. Bhanja, Y. Kim, B. Paul, Y. V. Kaneti, A. A. Alothman, A. Bhaumik, Y. Yamauchi, Microporous nickel phosphonate derived heteroatom doped nickel

oxide and nickel phosphide: Efficient electrocatalysts for oxygen evolution reaction, Chem. Engg. J. 405 (2021) 126803 1–10.

[49] N. L. W. Septiani, Y. V. Kaneti, K. B. Fathoni, Y. Guo, Y. Ide, B. Yuliarto, X. Jiang, Nugraha, H. K. Dipojono, D Golberg, Y. Yamauchi, Tailorable nanoarchitecturing of bimetallic nickel–cobalt hydrogen phosphate via the self-weaving of nanotubes for efficient oxygen evolution, J. Mater. Chem. A. 8 (2020) 3035–3047.

[50] Y. Y. Yao, H. J. Chao, T. H. Chou, S. H. Chang, C. G. Wu, Y. C. Ling, J. Y. Chang, In situ fabrication of $Co_{0.85}Se$ and $Ni_{0.85}Se$ hierarchical thin films as high-performance counter electrode for dye-sensitized solar cells, Solar Energy 137 (2016) 401–408.

[51] J. Bagchi, S. K. Bhattacharya, Electrocatalytic activity of binary palladium ruthenium anode catalyst on Ni support for ethanol alkaline fuel cells, Trans Met. Chem. 32 (2007) 45–55.

[52] P. S. Roy, S. K. Bhattacharya, Size-controlled synthesis, characterization and electrocatalytic behaviours of polymer protected nickel nanoparticles a comparison with respect to tend polymers, RSC Adv. 4 (2014) 13892–13900.

[53] J. Zhu, Y. Ni, Phase-controlled synthesis and the phase dependent HER and OER performances of nickel selenide nanosheets prepared by an electrochemical deposition route, Cryst. Engg. Commun. 20 (2018) 3344–3352.

[54] R. A. Hussain, I. Hussain, Fabrication and applications of nickel selenide, J. Solid State Chem. 277 (2019) 316–328.

[55] C.Wei, S. Sun, D. Mandler, X. Wang, S. Z. Qiao, Z. J, Xu, Approaches for measuring the surface areas of metal oxide electrocatalysts for determining their intrinsic electrocatalytic activity, Chem. Soc. Rev. 48 (2019) 2518–2534.

[56] J. O’, M. Bockris, A. K. N. Reddy, M. Gambda-Aldeco, In *Modern Electrochemistry* Vol. 2A, 2nd edn., Kluwer Academic, Netherlands, 2002.

[57] D. Chinnadurai, S. J. Lee, Y. Yu, S. Y. Nam, M. Y. Choi, Cation modulation in dual-phase nickel sulfide nanospheres by pulsed laser irradiation for overall water splitting and methanol oxidation reaction, Fuel 320 (2022) 123915 1–10.

[58] K. S. Bhat, H. S. Nagaraja, Effect of oxygen substitution and phase on nickel selenide nanostructures for supercapacitor applications, Mater. Res. Exp. 5 (2018) 105504 1–14.

[59] D. Chen, Y. Chen, W. Zhang, R. Cao, Nickel selenide from single-molecule electrodeposition for efficient electrocatalytic overall water splitting, New J. Chem. 45 (2021) 351–357.

[60] A. T. Swesi, J. Masud, M. Nath, Nickel selenide as a high-efficiency catalyst for oxygen evolution reaction, Energy Environ. Sci. 9 (2016) 1771–82.

[61] S. Anantharaj, E. Subhashini, K. C. Swaathini, T. S. Amarnath, S. Chatterjee, K. Karthick, S. Kundu, Respective influence of stoichiometry and NiOOH formation in hydrogen and oxygen evolution reactions of nickel selenides, Appl. Surf. Sci. 487 (2019) 1152–1158.

[62] Z. Zou, X. Wang, J. Huang, Z. Wu, F. Gao, An Fe-doped nickel selenide nanorod/nano sheet hierarchical array for efficient overall water splitting, J. Mater. Chem. A 7 (2019) 2233–3341.

# *CHAPTER 1*

# CHAPTER-II

## SUPERIORITY OF CuSe AS A NON-NOBLE ELECTROCATALYST AMONG COPPER CHALCOGENS FOR OVERALL WATER SPLITTING REACTIONS

# *CHAPTER 2*

# Superiority of CuSe as a non-noble electrocatalyst among copper chalcogens for overall water splitting reactions

## 3.1. Introduction

One of the serious upsurging global problems is the energy crisis that is world facing today. Energy demand is skyrocketing in the last few decades. Sources of non-renewable energy are depleting fast and the world is looking for new handy non-traditional energy sources. Splitting of water into oxygen and hydrogen is one of the best ways to overcome the current energy crisis and reduce air pollution simultaneously. For natural photosynthesis, which converts light energy into chemical energy, this is crucial. Cu is essential for the water splitting process in the biological systems. Some of the ongoing research efforts demonstrate an eagerness to comprehend the contribution of Cu to biological water splitting. In the effort to generate artificial photosynthetic systems employing sustainable and noble metal-free catalysts, highly crystalline CuSe has been deployed in alkaline media as active electrodes for overall water splitting (OWS) [1].

The low abundance of these precious elements limits their wide practical application. Copper is a more abundant and cheaper metal among the transition metal elements (such as cobalt, nickel, iridium and manganese). Recently, some copper-based compounds have been researched as OER catalysts, such as oxides, hydroxides, phosphides, nitrides and selenides [2–4]. Copper selenide is an important member of first row transition metal chalcogenides [5–7], can exist in a wide range of compositions, both stoichiometric (CuSe, $Cu_2Se$, $CuSe_2$, $Cu_3Se_2$, $Cu_7Se_4$) and non-stoichiometric ($Cu_{2-x}Se$) [8–9]. Although, they are rarely formed as minerals in nature, synthetic selenides represent a remarkable group of compounds with great potential in various scientific fields (such as photovoltaics, thermoelectric, or optoelectronics) due to their extraordinary electric and thermal properties. The state-of-the-art electrocatalysts to perform water splitting mainly rely on the noble-metal-based materials ($RuO_2$ and $IrO_2$ for OER, and Pt for HER). But their high cost has prevented their practical applications [10–11]. Conversely, recent studies infer that higher OER or HER catalytic activity could be achieved by a subtle choice of earth-abundant transition metal-based catalysts, particularly the first-row metallic components [12–17]. However, only a few of them have been shown to mediate efficient bifunctionality for water splitting reactions [18–19]. The metal organic framework (MOF) can act as an efficient bifunctional electrocatalyst for HER and OER [20].

Electrochemical water splitting continues to be a frontier field of study. In this respect, it is worth to point out that many transition metal nitrides, phosphides, chalcogenides, MOF, polymers and their composites that have been established to realize the comparable efficacy to substitute the state-of-the-art catalyst, Pt. In comparison, very few works have been done with $Cu^{II}$ chalcogenides as electrocatalysts [21]. In search of low overpotential material, we concentrated in this study on $Cu^{II}$ chalcogenides which may help in understanding the chalcogen group, since some $Cu^{I}$ and $Cu^{III}$ compounds, like $Cu_2Se$, $Cu_3N$, $Cu_3P$, etc. are already found in the literature [22–24].

## 3.2. Experimental section

### *3.2.1. Chemicals*

Copper nitrate ($Cu(NO_3)_2$ (99.99% Merck), sodium sulphide ($Na_2S$) (99.99% Merck), sodium hydroxide (NaOH) (99.9%, Sigma-Aldrich), sodium selenite ($Na_2SeO_3$) (99.99% Merck), hydrazine hydrate ($N_2H_4.H_2O$) (99%, Sigma-Aldrich) have been used without further purification. The deionized water has been used throughout the study. Any other solvents have been purchased from Sigma-Aldrich and used without further purification.

### *3.2.2. Synthesis of copper oxide, sulphide and selenide nanoparticles*

An aliquot of 2 M copper nitrate and 1 M sodium selenite ($Na_2SeO_3$) were mixed thoroughly and equivalent amount of hydrazine hydrate was added in the solution. The mixture was put into the autoclave and heated for 24 h at 180 °C. Then, the mixture was cooled to room temperature. The solution was centrifuged and the product was heated at 60 °C in a hot air oven. Copper nitrate and sodium sulphide was used for the synthesis of copper sulphide nanoparticles. Similarly, copper nitrate and sodium hydroxide were used for synthesis of copper oxide nanoparticles in the same hydrothermal procedure.

### *3.2.3. Structural characterization*

The crystal structure of synthesized nanoparticles was investigated by X-ray diffraction (XRD) study was performed using a (Bruker D8 Advance) diffractometer equipped with a $CuK_\alpha$ radiation source ($\lambda$=1.5418Å generated at 40 kV and 40 mA.). The field emission scanning electron spectroscopy (FESEM) and energy dispersion X-ray spectroscopy (EDX) with SEI INSPECT F50 FE-SEM was used for the characterization of morphology and composition. The chemical valence was characterized by X-ray photoelectron spectroscopy.

### *3.2.4. Electrochemical characterization*

The electrocatalytic responses of the catalysts were demonstrated using cyclic voltammetry (CV) and fixed potential chronoamperometric (CA) studies. The electrochemical measurements were conducted using a computer aided potentiostat/galvanostat of AUTOLAB PG STAT 12 (Eco Chemic, Netherlands). The reference electrode used in all electrochemical measurements was Ag/AgCl (KCl saturated). In all of the electrochemical studies a large Pt-foil (1 cm × 1 cm) was used as counter electrode. The working electrode was a planar graphite carbon electrode having area as $12 \times 10^{-6}$ $m^2$. The working electrode was prepared by sonication of 5 mg of catalyst dust in 1 mL ethanol for 30 min to form an almost homogeneous mixture. 10 μL of the dispersion was, then, drop cast on the carbon electrode followed by drying at room temperature (25 °C). Then, 5 μL Nafion solution (1 mass %) was cast on the electrode followed by drying again cyclic voltammogram of each electrode measured in 1 M KOH solution at the scan rate of 50 mV $s^{-1}$ for OER and 0.5 M $H_2SO_4$ solution for HER. The measurement potentials were converted to the reversible hydrogen electrode (RHE) by using Nernst equation,

$$E_{RHE} = E_{Ag/AgCl} + (0.059\ pH + 0.197)\ V \qquad (3.\ 1)$$

The value of overpotential (η) was calculated by the equation,

$$\eta = E_{RHE} - 1.23\ V \qquad (3.\ 2)$$

The electrochemical kinetics of the catalysts towards water splitting reaction the overpotential η with was evoluted by Tafel equation,

$$\eta = a + b\log j \qquad (3.\ 3)$$

where j is the current density, b is Tafel slope and a is constant.

The electrochemical active surface area (ECSA) was calculated from double layer capacitane, $C_{dl}$ by cyclic voltammograms measured as various scan rates 10, 20, 40, 50, 80, 100 mV $s^{-1}$ in the potential range in the non-Faradic region. The $C_{dl}$ was evaluted from the average value of cathodic and anodic slopes. The turnover frequency was calculated from CV and CA plots.

## 3.3. Results and Discussion

### *3.3.1. XRD analysis*

Powder X-Ray diffractometer (XRD) was used to analyze the crystal structure of the as-synthesized samples as has been shown in Fig. 3.1. Copper selenide nanoparticles contain 27.31 (103), 31.23 (110), 45.06 (111), 46.95 (106), 50.14 (200), 53.35 (202), 56.12 (116) and 72.84 (220) planes. The mean size of the nanoparticle has been calculated from the peak width at half maximum as 18.4 nm by the Debye Scherrer equation. Copper sulphide nanoparticles contain 28.1 (101), 29.01 (102), 31.50 (103), 32.01 (006), 49.01 (110), 53.1 (108) and 60.1(116) planes (JCPDS No.: 06-0464) and half maxima is 17.23 nm. Copper oxide nanoparticles contain 29.1 (110), 45.5 (002), 55.5 (200), 68.9 (113) planes (JCPDS No.89-2531) and half maxima is 16.10 nm.

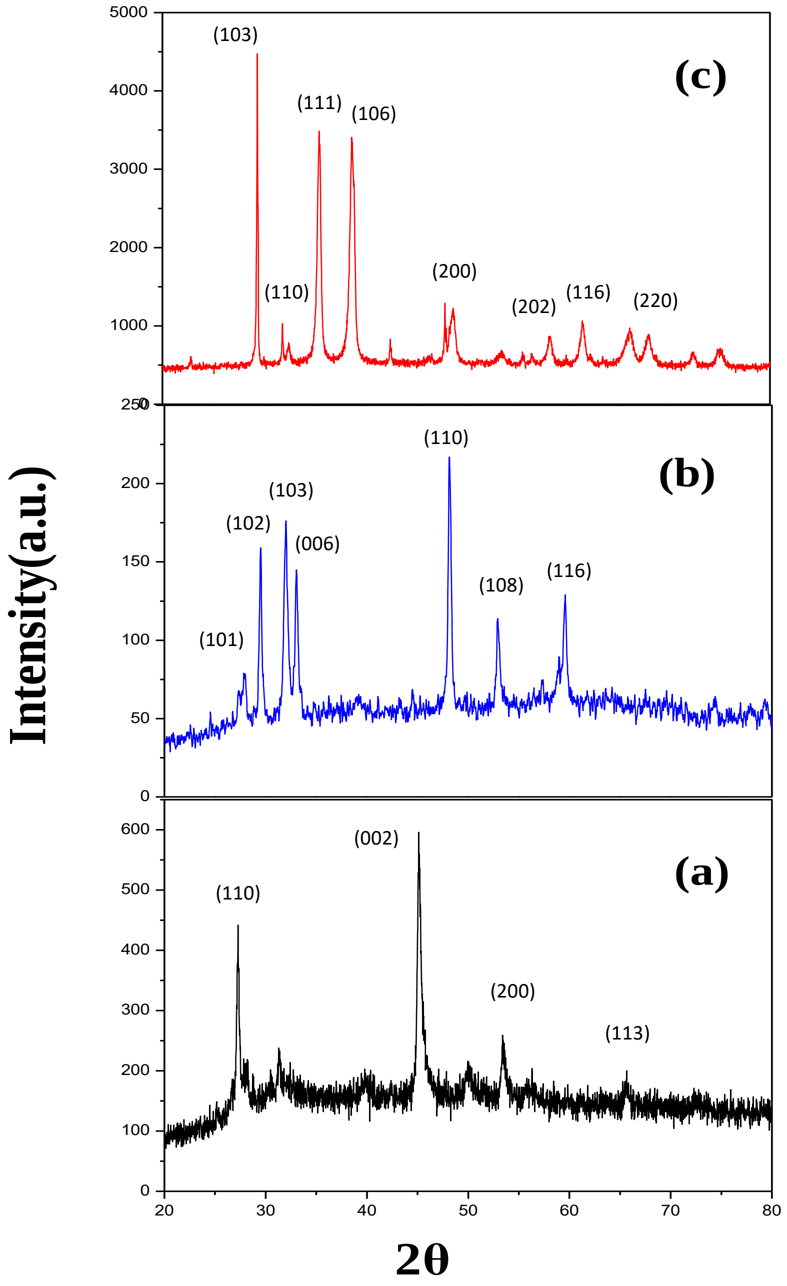

**Fig. 3.1.** X-ray diffraction plots of (a) CuO, (b) CuS and (c) CuSe nanoparticles. The 2θ values along the *x*-axis have been expressed in degrees.

### *3.3.2. FTIR analysis*

Fourier transform infrared spectra of CuO, CuS and CuSe nanoparticles have been exhibited in Fig. 3.2. CuO nanoparticles bands at around 601 cm$^{-1}$ and 487 cm$^{-1}$ for vibrations confirm the formation of Cu-O bonds. The sharp peak observed at 601 cm$^{-1}$ characteristics of Cu-O bond formation. A broad peak at 3433 cm$^{-1}$ for O-H stretching arises due to moisture content [25]. For CuS nanoparticles, 3435 cm$^{-1}$ vibration mode corresponding to –OH group indicating the presence of small amount of water absorbed on the particle 1631 cm$^{-1}$ for –OH bending [26]. CuSe exhibits two major peaks at 1609 cm$^{-1}$ and 3471 cm$^{-1}$. The peak at 1609 cm$^{-1}$ may be attributed to the presence of Cu$^{2+}$ ion in the present system. The peak at around 3471 cm$^{-1}$ may corresponds to N-H stretching vibration band which can be attributed to the interaction of $N_2H_4$ with copper ions [27].

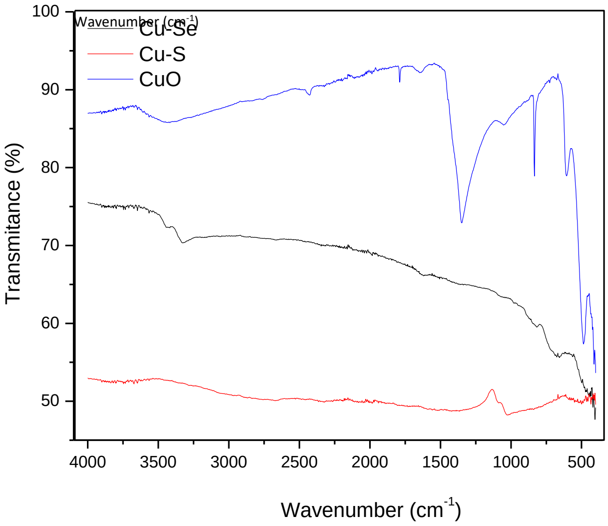

**Fig. 3.2.** Fourier transform infrared spectra of CuO, CuS and CuSe nanoparticles

### 3.3.3. FESEM and TEM analysis

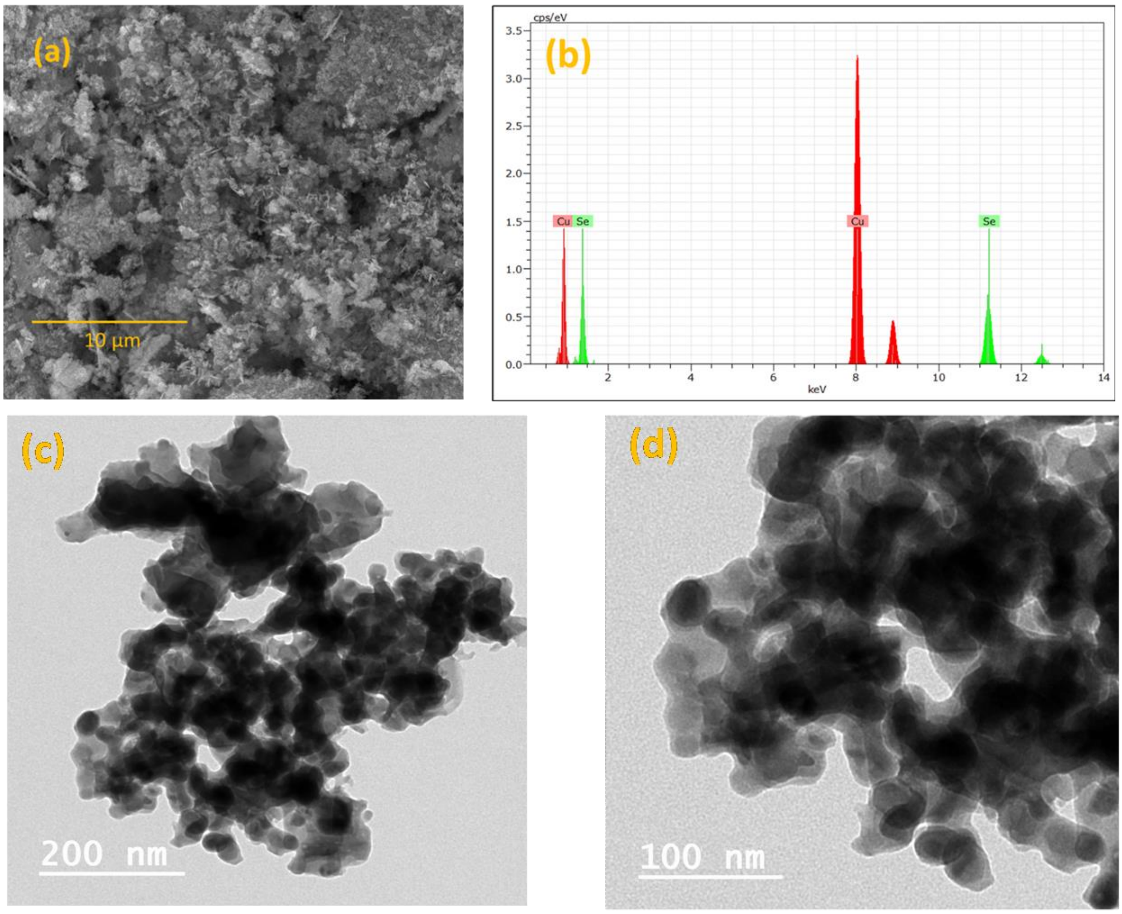

**Fig. 3.3.** (a) Field emission scanning electron micrograph; (b) energy dispersive X-ray spectrum; and (c, d) transmission electron micrographs of CuSe nanoparticles at different magnifications

The FE-SEM, EDX and TEM observation giving the morphology and composition of CuSe nanoparticles are shown in Fig. 3.3. Here, we are obtaining nanoscale images and chemical data using HR-transmission electron microscopes (S/TEM) in conjunction with energy dispersive X-ray spectroscopy (EDX), providing crucial insights into the configuration and potential functions of deployed Cu-catalyst. The contrast of TEM image arises from the interference in the image plane of the electron wave itself.

### 3.3.4. XPS analysis

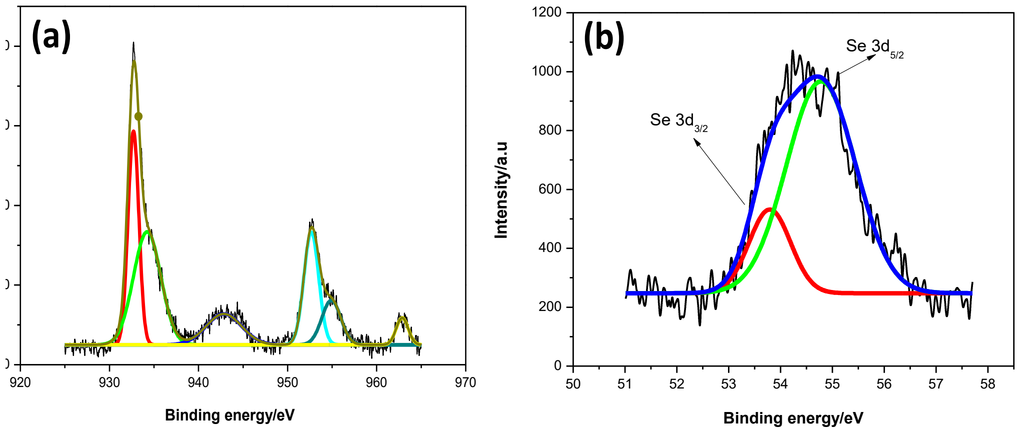

**Fig. 3.4**. X-ray photoelectron spectra corresponding to (a) Cu and (b) Se of CuSe nanoparticles

In this study, we also employed X-ray photoelectron spectroscopy to analyze the surface chemistry of our catalyst samples as has been presented in Fig. 3.4. The purpose of this experiment was to determine the elemental composition and chemical state of the atoms within our sample. Using an X-ray beam, the surface atoms of the solid copper chalcogen samples being excited and measured the kinetic energy and the number of electrons that escaped from the top 0 to 10 nanometers of the sample. On the generated spectra, the position of a peak on the *x*-axis indicated the elemental and chemical composition while the *y*-axis recorded the intensity of surface material how much of a particular element can be found at the surface. Peaks from the XPS spectra gave relative number of electrons with a specific binding energy. Our results showed that our sample contained Cu and Se elements. In the high-resolution XPS, the Cu2p envelope consisted of two peaks corresponding to $Cu2p_{3/2}$ and $Cu2p_{1/2}$ at the binding energies of 932.1 eV and 952.2 eV, respectively. The Se3d envelope recorded with the powder sample showed an overlapped spin-orbit component with two maxima for $3d_{5/2}$ and $3d_{3/2}$ peaks at 53.8 and 54.5 eV (D = 0.7 eV). These energy values (after deconvolution) are consistent with the presence of Se(II), as shown for reported CuSe materials. Moreover, a weak loss feature at 56.1 eV and a weak peak corresponding to Se(IV) arise from surface passivation at 58.3 eV, as observed in other metal selenides.

## 3.4. Electrochemical results

The electrochemical performances are studied in 1.0 M KOH and 0.5 M $H_2SO_4$ solutions at the scan rate of 50 mV $s^{-1}$ for OER and HER, respectively as have shown in Fig. 3.5. These exhibit shoulders before oxygen evolution and corresponding small peaks in the reverse scan plausibly due to $Cu/Cu^{+2}$ and reverse transition, respectively. The oxidation state of chalcogens seems to be much more stable in the scan range. The onset potential of CuSe, CuS and CuO catalysts for OER follows the order: CuSe < CuS < CuO as presented in the Table 3.1, indicating the reverse order of catalytic activity near the equilibrium region. The overpotential (mV) at the benchmark current density, 10 mA $cm^{-2}$ are 410, 385, and 343 for these synthesized materials, CuO, CuS and CuSe, respectively revealing superiority of CuSe over others in catalytic property. During activation process of the CuSe based electrode by repeated cyclic voltammetry, it is found that the overpotential decreases with increase of catalytic cycle. In the first 100 cycles, the overpotential decreases by about 120 mV. It is expected that there might be some compositional/morphological change of the catalyst at least at the surface of the electrode which is responsible for such positive effect.

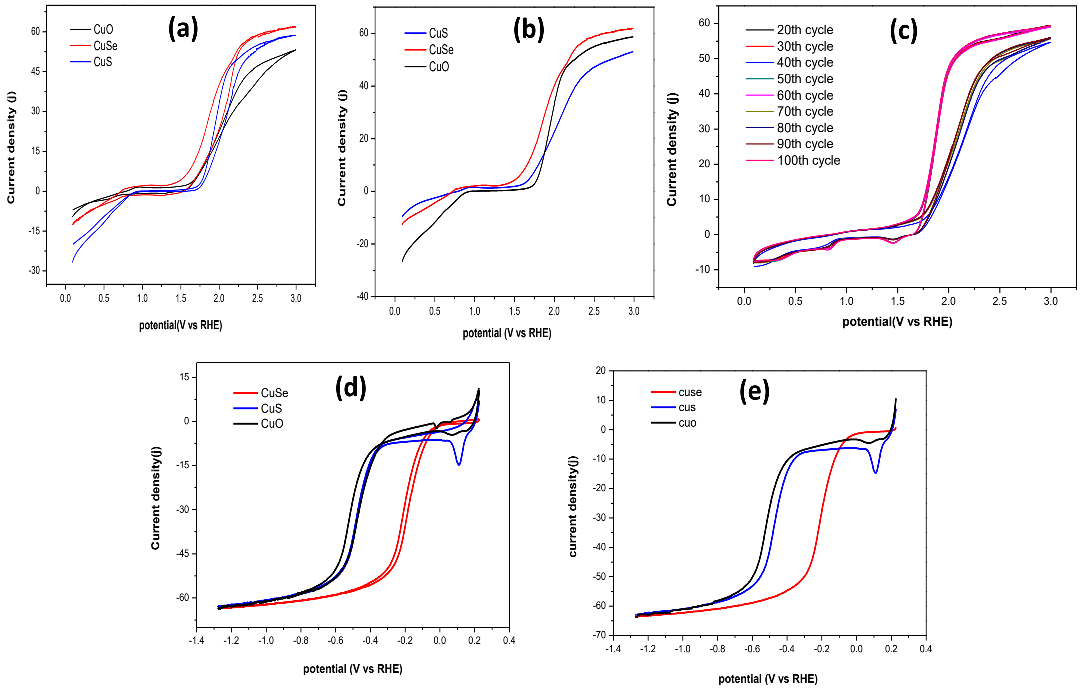

**Fig. 3.5.** (a, b) Cyclic voltammogram and linear sweep voltammetry for OER in 1 M KOH solution; (c) cyclic voltammogram up to 100th cycle; and (d, e) cyclic voltammogram and linear sweep voltammetry for HER in 0.5 M $H_2SO_4$ solution.

The reason behind such trend might be due to the formation of a thin layer of $Cu(OH)_2$ which acts as electro-post-catalyst in alkali as suggested elsewhere [1]. The $Cu(OH)_2$ layer is thin over CuSe; since, the latter is enough stable and found in nature as selenide materials [28-29]**.** The trend of greater catalytic ability of CuSe over CuO and CuS is also found at much higher current density. The order of overpotential @10 mA cm$^{-2}$ is found to be CuSe < CuS < CuO, (343, 385, 410 mV) but that for 50 mA cm$^{-2}$ is CuSe < CuO < CuS, (768, 823, 943 mV) implying that CuO is a better catalyst over CuS at higher potentials/current density. This indicates a large change of catalytic activity of CuO based electrode at higher potential in comparison to CuS, which might be due to the greater formation of $Cu(OH)_2$ or CuOOH on the surface of CuO based electrode at higher potential [20–21].

To assess the constancy in catalytic activity and long-term stability of catalysts, chronoamperometric measurements were carried out at a potential of -0.4V for 1200 s in a solution of 0.5 M $H_2SO_4$ and 0.8 V in 1 M KOH solution as have been presented in Figure 3.6.

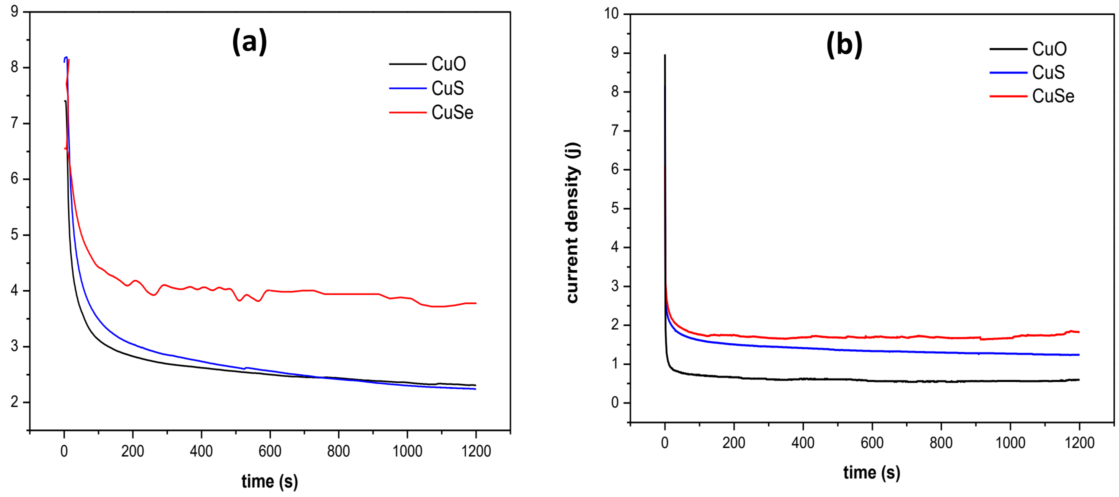

**Fig. 3.6.** Chronoamperometry plot corresponding to the electrocatalysts in (a) 1.0 (M) KOH and (b) 0.5 (M) $H_2SO_4$ solution

Turnover frequency (TOF) is an integral property of an ideal catalyst. The TOF for both HER and OER can be calculated by assuming 100 % faradic efficiency for the catalysts as,

$$TOF = I/nFm = JA'/nFm \qquad (3.4)$$

where I = current (A), J = average current density (A $cm^{-2}$), A′ = geometrical surface area = 0.12 $cm^2$, n = number of electrons being transferred = 4 (for OER)/2 (for HER), F = 96485 C, m = moles of catalyst per active site [30–31]

**Table 3.1.** Cyclic voltammetry and chronoamperometry data of oxygen and hydrogen evolution reaction

| Turnover frequency ($h^{-1}$) | CV | | CA | |
|---|---|---|---|---|
| | OER | HER | OER | HER |
| CuO | 0.76 | 0.59 | 0.51 | 0.49 |
| CuS | 0.33 | 1.81 | 0.54 | 0.77 |
| CuSe | 1.40 | 7.18 | 1.20 | 5.47 |

The onset potential of hydrogen evolution reaction (HER) on CuSe, CuS and CuO are 108,136 and 142 mV *vs.* RHE. The overpotentials at current density 10 mA $cm^{-2}$ for the reaction are 126, 320 and 345 mV respectively. The electronegativity of Se is greater than Cu. Thus, Cu is slightly +ve and Se is –ve in CuSe nanostructures. Therefore, for OER, Cu center acts as $OH^-$ adsorption center to initiate the reaction. CuSe + $OH^- \rightarrow$ HO-CuSe + e (M). The intermediate HO….CuSe subsequently causes OER. On the otherhand, Se acts as a center for adsorption of $H^+$ accordingly to the reaction, CuSe + $H_2O \rightarrow$ CuSe….H + $OH^-$. The intermediate, CuSe…..H subsequently undergoes HER. These are obtained from the detail experimental kinetic measurements and theoretical studies on the energy and stability of the involved intermediates of the reactions. According to periodic table down the group, the size of the elements increases and so the bond length increases and bond energy decreases. The component, Cu…Se is thermally broken easily than CuS and CuO; as a consequence, CuSe shows better water splitting reaction (bond lengths of CuO, CuS and CuSe are 1.98, 2.24 and 2.51 Å). The formation of $Cu(OH)_2$ layer is thin over CuSe since the latter is enough stable and found in nature at higher potential. This indicates a large change in catalytic activity of CuO based electrode in comparison to CuS which might be due to the formation of $Cu(OH)_2$ or CuOOH at higher potential [32–33].

OER Mechanism

$$CuX + OH^- \rightarrow CuXOH + e^- \qquad (3.5)$$

$$CuXOH + OH^- \rightarrow CuXO + H_2O + e^- \qquad (3.6)$$

$$CuXO + CuXO \rightarrow 2CuX + O_2 \qquad (3.7)$$

$$2CuCOH + 4OH^- \rightarrow 2CuOOH + 2H_2X + O_2 \qquad (3.8)$$

$$CuXOH + CuOOH \rightarrow CuX + O_2 + H_2O \qquad (3.9)$$

HER possess through three distinct routes by 2e$^-$ transfer mechanism in acidic medium which can be expressed as,

$$\text{Volmer step: } H_3O^+ + * + e^- \rightarrow H^* + H_2O \qquad (3.10)$$

$$\text{Heyrovsky step: } H_3O^+ + H^* + e^- \rightarrow H_2 + H_2O + * \qquad (3.11)$$

$$\text{Tafel step: } H^* + H^* \rightarrow H_2 + 2^* \qquad (3.12)$$

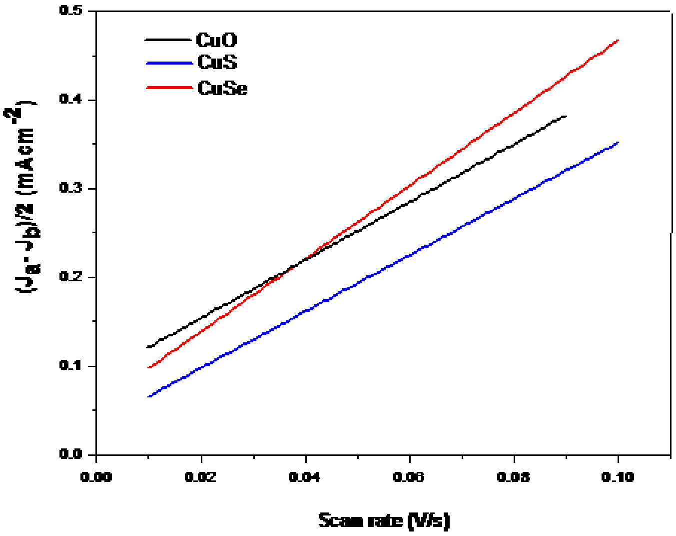

**Fig. 3.7.** $C_{dl}$ plots CuO, CuS and CuSe electrocatalysts

The $C_{dl}$ values for CuO, CuS and CuSe electrocatalysts are 2.18, 2.27 and 4.12 mF cm$^{-2}$, respectively.The electrochemical active surface area of CuO, CuS and CuSe electrocatalysts are 5.5, 5.7 and 10.3 c respectively. From the Randles equivalence circuit model, $R_s$, series resistance, can be calculated at the intersection of the real axis ($x$-axis) in the high-frequency region. The series resistance, $R_s$ represents the ohmic resistance and ionic resistance at the electrode and electrolyte interface. However, the charge transfer resistance ($R_{ct}$) has been found from the lower-frequency region of the Nyquist plot [34] as have been shown in Fig. 3.8.

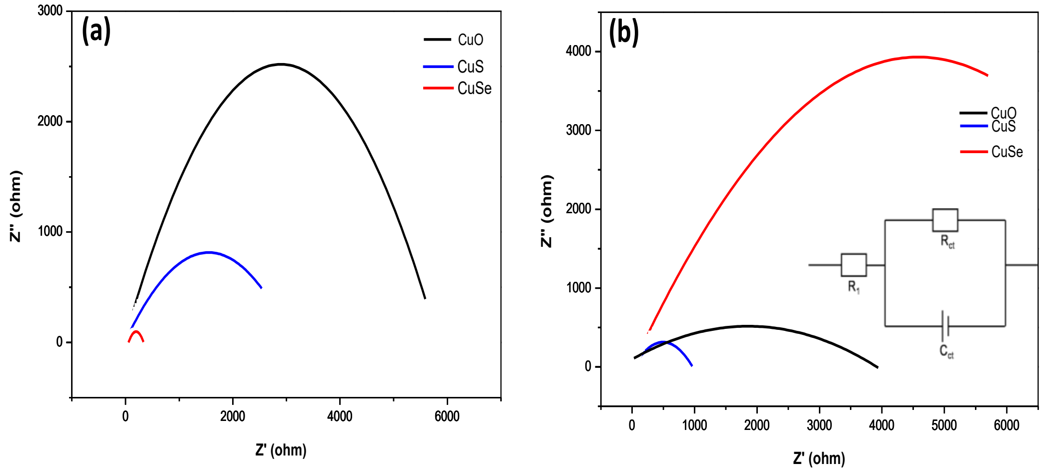

**Fig. 3.8**. Nyquist plots of (a) OER in KOH medium and (b) HER in $H_2SO_4$ medium

To study the reaction kinetics electrochemical impedence spectroscopy (EIS) measured as have been presented in Table 3.2. The OER involves a four electron transfer process, higher potentials than the theoretical potential (>1.23 V *vs.* RHE) are required to surmount the overall energy barrier in each electron transfer step [35-36]. Overpotential (η) is one of the most crucial parameters that affect the OER/HER performance of the electrocatalysts which is usually measured at a specific current density of 10 mA $cm^{-2}$.

$$\eta = a + b \log (j) \tag{3.13}$$

**Table 3.2.** Electrochemical impedance spectroscopy data corresponding to CuO, CuS and CuSe electrocatalysts

| Electrocatalyst | Electrolyte | $R_s$ (Ω) | $R_{ct}$ (Ω) | $C_{ct}$ (μF) |
|---|---|---|---|---|
| CuO | 1 (M) KOH | 71.82 | 2198 | 4.20 |
| | 0.5 (M) $H_2SO_4$ | 56.78 | 2325 | 5.98 |
| CuS | 1 (M) KOH | 44.04 | 1157 | 1.83 |
| | 0.5 (M) $H_2SO_4$ | 53.90 | 776 | 1.33 |
| CuSe | 1 (M) KOH | 42.00 | 1137 | 1.56 |

| | | | | |
|---|---|---|---|---|
| | 0.5 (M) $H_2SO_4$ | 52.08 | 285 | 1.26 |

Low overpotential shines as advantages of good OER electrocatalysts. Because of the high overpotential, leads to more energy consumption reducing energy conversion efficiencies. It is highly suggested that the loading mass and turnover frequency are reported while comparing the OER/HER activities of electrocatalysts as overpotential is strongly influenced by the loading mass of electrocatalysts.

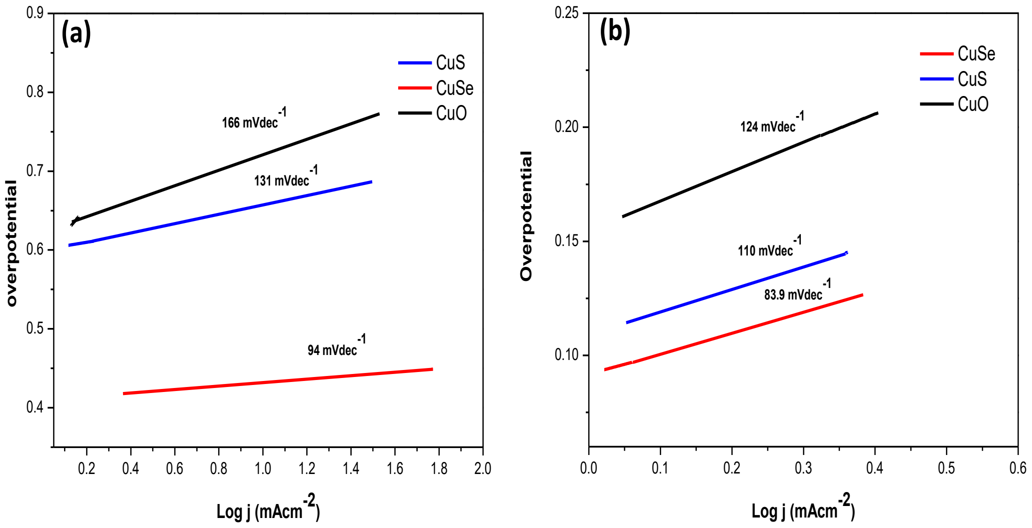

**Fig. 3.9.** (a) OER and (b) HER Tafel plots for CuO, CuS and CuSe nanoparticles

Tafel slope (η) is another crucial parameter that reflects the kinetics of OER and HER. According to the Tafel equation, the slope is the rate of augmentation of overpotential (η) in relation to current density (j). A diminished Tafel slope implies a rapid escalation in the current density with the increment of overpotential, which signifies swift of OER and HER kinetics of the electrocatalysts. The Tafel slopes (mV dec$^1$) found for OER are 166, 131 and 94 for CuO, CuS and CuSe, respectively. The experimental Tafel slopes (mV dec$^{-1}$) for HER with CuO, CuS and CuSe are 124, 110, 83.9, respectively. The Tafel slopes for HER indicate that the Tafel-Heyrovsky mechanism is followed for all the materials. Table 3.3 compares the efficacy of the synthesized materials with some others used as electrocatalysts in reference to HER and OER. It is found that the study on Cu$^{II}$ bssed materials is few and the overpotetial and Tafel slopes using the synthesized Cu$^{II}$ chalcogenides are comparable with those of the others.

**Table 3.3.** Comparative account of electrochemical performance of copper chalcogenides with similar materials

| Electrocatalyst | Electrolyte | Reaction | Overpotential ($\eta$) (mV) | Tafel slope (mV dec$^{-1}$) | Reference |
|---|---|---|---|---|---|
| CuO | 1 M KOH | OER | 410 | 188 | Present work |
| | 0.5 M $H_2SO_4$ | HER | 345 | 124 | Present work |
| CuS | 1 M KOH | OER | 385 | 131 | Present work |
| | 0.5 M $H_2SO_4$ | HER | 320 | 110 | Present work |
| CuSe | 1 M KOH | OER | 343 | 94 | Present work |
| | 0.5 M $H_2SO_4$ | HER | 126 | 83.9 | Present work |
| CuSe film | 1 M KOH | OER | 270 | | [29] |
| $Cu_3P$/CuO core/shell nanorod arrays | 1 M KOH | OER | 315 | | [33] |
| $Cu_2S$ branch arrays | 1 M KOH | OER | 284 | | [35] |
| CuO nanoparticles | 1 M NaOH | OER | 290 | | [36] |

## 3.5. Conclusions

Electrocatalytic water splitting is an emerging and challenging area of chemistry that has received limited attention until the last two decades. To explore the potential of powdered catalysts for water splitting reaction, especially those based on earth abundant metals, we synthesized Cu based nanoparticles via a hydrothermal approach and evaluated their electrocatalytic performance for both oxygen evolution reaction (OER) and hydrogen evolution reaction (HER). Powdered catalysts offer advantages for large-scale application of water splitting due to their high turnover numbers and low overpotential.

We also investigated other copper chalcogenides, such as copper oxide and copper sulphides (which were prepared under similar conditions by the same method) and demonstrated that CuSe exhibited superior catalytic activity for both OER and HER compared to the other copper chalcogenides. This indicates that the activity and electronic structure of electrocatalysts for water electrolysis can be modulated by varying the chalcogen element in the same group. The present study provides a new opportunity to design and fabricate novel catalysts from noble-metal-free and earth-abundant sources, and to disseminate valuable information and knowledge to the scientific community interested in electrocatalytic water splitting.

## References

[1] B. Chakraborty, R. Beltr-Suito, V. Hlukhyy, J. Schmidt, P. W. Menezes, M. Driess, Crystalline copper selenide as a reliable non-noble electro(pre)catalyst for overall water splitting, ChemSusChem 13 (2020) 3222–3229.

[2] G. Jia, W. Zhang, G. Fan, Z. Li, D. Fu, W. Hao, C. Yuan, Z. Zou., Three-dimensional hierarchical architectures derived from surface-mounted metal e organic framework membranes for enhanced electrocatalysis, Angew. Chem. Int. Ed. 56 (2017) 13781 1–5.

[3] T. N. Huan, G. Rousse, S. Zanna, I. T. Lucas, X. Xu, N. Menguy, V. Mougel, M. Fontecave, A dendritic nanostructured copper oxide electrocatalyst for the oxygen evolution reaction, Angew. Chem. Int. Ed. 56 (2017) 4792 1–6.

[4] L. Bie, X. Lue, Q. He, D. He, Y. Liu, P. Jiang, Hierarchical $Cu/Cu(OH)_2$ nanorod arrays grown on electrode for enzyme-free glucose sensing, RSC Adv. 6 (2016) 95740–95746.

[5] M.D. Khan, M.A. Malik, N. Revaprasadu, Progress in selenium based metal-organic precursors for main group and transition metal selenide thin films and nanomaterials, Coord. Chem. Rev. 388 (2019) 24–47.

[6] R.A. Hussain, I. Hussain, Fabrication and applications of nickel selenide, J. Solid State Chem. 277 (2019) 316–328.

[7] R. A. Hussain, I. Hussain, Copper selenide thin films from growth to applications, Solid State Sci. 100 (2020) 106101 1–3.

[8] E. Andrade, V. M. Garcí, P. K. Nair, M. T. S. Nair, E. P. Zavala, L. Huerta, M. F. Rocha, Ion beam analysis of copper selenide thin films prepared by chemical bath deposition, Nucl. Instrum. Methods Phys. Res. B 161–163 (2000) 635–640.

[9] V. M. Garcí, P. K. Nair, M. T. S. Nair, Copper selenide thin films by chemical bath deposition, J. Cryst. Growth 203 (1999) 113–124.

[10] P. Chakadola, M. Prashanth W, Zheng Min, O. Steven, D. Matthias. In-situ formation of nanostructured core-shell $Cu_3N$-CuO to promote alkaline water electrolysis, ACS Energy Lett. 4 (2019) 747–754.

[11] D. Thanh, H Tuan, T. Luu, L. Doan, N. Hoon, J. Hee, Pt nanodots monolayer modified mesoporous Cu@$Cu_xO$ nanowires for improved overall water splitting reactivity, Nano Energy 59 (2019) 216–228.

[12] S. Zhao, J. Huang, Y. Liu, J. Shen, H. Wang, X. Yang, Y. Zhu, C. Li, Multimetallic NieMo/Cu nanowires as nonprecious and efficient full water splitting catalyst, J. Mater Chem. A 5 (2017) 4207–4214.

[13] J. Theerthagiria, S. J. Leea, A. P. Murthy, J. Madhavanb, M. Y. Choia, Fundamental aspects and recent advances in transition metal nitrides as electro catalysts for hydrogen evolution reaction, A review Curr. Opin. Solid State Mater. Sci. 24 (2020) 100805 1–3.

[14] Y. Yiseul, J. Theerthagiri, J. Seung, G. Muthusamy, M. Ashokkumar, Y. C. Myong, Integrated technique of pulsed laser irradiation and sonochemical processes for the production of highly surface-active NiPd spheres, Chem. Engg. J. 411 (2021) 128486 1–3.

[15] Y. Yiseul, J. L. Seung, J. Theerthagiri, S. Fonseca, L. M. C. Pinto, G. Maia, M. Y. Choi, Reconciling of experimental and theoretical insights on the electroactive behavior of C/Ni nanoparticles with AuPt alloys for hydrogen evolution efficiency and non-enzymatic sensor, Chem. Engg. J. 435 (2022) 134790 1–3.

[16] S. N. Shreyanka, J. Theerthagiri, S. J. Lee, Yu. Yiseul, M. Y. Choi, Multiscale design of 3D metal–organic frameworks (M-BTC, M: Cu, Co, Ni) via PLAL enabling bifunctional electrocatalysts for robust overall water splitting, Chem. Engg. J. 446 (2022) 137045 1–3.

[17] J. Theerthagiri, K. Karuppasamy, S. J. Lee, R. Shwetharani, H. S. Kim, S. K. K. Pasha, M. Ashokkumar, M. Y. Choi, Fundamentals and comprehensive insights on pulsed laser synthesis of advanced materials for diverse photo- and electrocatalytic applications, Light Sci. Appl. 11 (2022) 250 1–47.

[18] S. Chatterjee, S. Shaymal, M. Mukherjee, D. Halder, S. Chongdar, A. Paul, A. Bhaumik, Metal-Thiolate framework for electrochemical and photoelectrochemical hydrogen generation, ChemSusChem 15 (2022) e202200114 1–7.

[19] S. Zhao, J. Huang, Y. Liu, J. Shen, H. Wang, X. Yang, Y. Zhu, C. Li., Multimetallic Ni–Mo/Cu nanowires as nonprecious and efficient full water splitting catalyst, J. Mater. Chem. A 5 (2017) 4207–4214.

[20] Y. Hou, M. Qiu, T. Zhang, X. Zhuang, C. Kim, C. Yuan, X. Feng, Ternary porous cobalt phosphoselenide nanosheets an efficient electrocatalyst for electrocatalytic and photoelectrochemical water splitting, Adv. Mater. 29 (2017) 1701589 1–9.

[21] K. K. Bera, M. Chakraborty, S. R. Chowdhury, A. Ray, S. Das, S. K. Bhattacharya, Significantly improved and synergistic effect of Pt–ZnO–$Bi_2O_3$

ternary hetero-junctions toward anode-catalytic oxidation of methanol in alkali, Electrochim. Acta 322 (2019) 134775 1–7.

[22] W. Shi, J. Lian, Facile synthesis of copper selenide with fluffy intersected-nanosheets decorating nanotubes structure for efficient oxygen evolution reaction international, J. Hydrogen Energy 44 (2019) 229831–922990.

[23] A. Sajeev, A. M. Paul, R. Nivetha, K. Gothandapani, T. S. Gopal, G. Jacob, M. Muthuramamoorty, S. Pandiaraj, A. Alodhayb, S. Y. Kim, Q. V. Le, P. L. Show, S. K. Jeong, A. N. Grace, Development of $Cu_3N$ electrocatalyst for hydrogen evolution reaction in alkaline medium, Sci. Rep. 12 (2022) 2004 1–13.

[24] W. Shuting, Q. Kun, J. Zhao, C. Jiashu, W. Zheng, H. Chen, X. Cui, One-Step synthesis of a self-supported copper phosphide nanobush for overall water splitting, ACS Omega 1 (2016) 1367–1373.

[25] A. Radhakrishnan, B. Beena, Structural and optical absorption analysis of CuO nanoparticles, Ind. J. Adv. Chem. Sci. 2 (2014) 158–161.

[26] S. Riyaz, A. Parveen, A. Azam, Microstructural and optical properties of CuS nanoparticles prepared by sol-gel route, Perspecive Sci. 8 (2016) 632–635.

[27] N. N. Krishnan, S. Vijayakumar, P. Gnanadurai, R. Shabu, K. C. Preetha, Structural and optical characterization of copper selenide ($Cu_{2-X}Se$) nanoparticles, J. Nanosci. Tech. 4 (2018) 345–347.

[28] J. Masud, W. P. R. Liyanage, X. Cao, A. Saxena, M. Nath, Copper selenides as high-efficiency electrocatalysts for oxygen evolution reaction, ACS Appl. Energy Mater. 1 (2018) 4075−4083.

[29] R. A. Hussain, I. Hussain, Copper selenide thin films from growth to applications, Solid State Sci., 100 (2020) 106101 1–9.

[30] S. L. Goes, M. N. Mayer, J. E. Nutting, L. E. Hoober-Burkhardt, S. S. Stahl, M. Rafiee, Deriving the turnover frequency of aminoxyl-catalyzed alcohol oxidation by chronoamperometry, An introduction to organic electrocatalysis, Chem. Ed. 98 (2021) 600–606.

[31] H. Rahaman, S. Kundu, S. K. Ghosh, Size-selective silver-induced evolution of $Mn_3O_4$-Ag nanocomposites for effective ethanol sensing, Chem. Select 2 (2017) 6991–6999.

[32] C. Wei, Z. J. Xu, The comprehensive understanding of 10 mA $cm^{-2}$ as an evolution parameter for electrochemical water splitting, Small 2 (2018) 1800168 1–6.

[33] J. Du, F. Li, Y. Wang, Y. Zhu, L. Sun. $Cu_3P$/CuO core-shell nanorod arrays as high-performance electrocatalysts for water oxidation, ChemElectroChem, 5 (2018) 2064–2068.

[34] A. Ghosh, S. Shyamal, A. Palui, R. N. Manna, S. Mondal, M. Jana, A. Ghosh, A. Bhaumik, Photoelectrochemical water oxidation over novel semiconducting zinc-based metal─thiolate framework, ACS Appl. Mater. Interfaces 14 (33) (2022) 37699–37708.

[35] T. N. Huan, G. Rousse, S. Zanna, I. T. Lucas, X. Xu, N. Menguy, V. Mougel, M. Fontecave, A dendritic nanostructured copper oxide electrocatalyst for the oxygen evolution reaction, Angew. Chem. Int. Ed. 56 (2017) 4792–4796.

[36] S. Deng, Y. Shen, D. Xie, Y. Lu, X. Yu, L. Yang, X. Wang, X. Xia, J. Tu, Directional construction of $Cu_2S$ branch arrays for advanced oxygen evolution reaction, J. Energy Chem. 39 (2019) 61–67.

# CHAPTER-III

# WATER SPLITTING REACTION ON NICKEL SULPHIDE, MOLYBDENIUM SULPHIDE, NICKELMOLYBDENIUM SULPHIDE ELECTROCATALYSTS

# *CHAPTER 3*

# Water splitting reaction on NiS, MoS, NiMoS electrocatalysts

## 4.1. Introduction

Due to increasing global energy demand while on the contrary, to protect the environment, it is obvious to lessen our dependence on fossil fuels and therefore, to increase the amount of sustainable and renewable energy resources [1]. During the past couple of decades, various approaches to encompass the efficient production of biofuels with hydrogen, methane, and bioalcohols have been demonstrated [2–5]. Hydrogen has been considered as a model fuel to meet the need as one of the energy resources of the future.

One of the most effective and fascinating processes for producing hydrogen is the water splitting reaction in the presence of light or electricity [6–12]. The splitting of water using electrochemical techniques is a viable method to convert electricity into chemical energy [13]. The transition metal sulphides possessing typical structural character rich with active sites, and adjustable to the electronic properties and components have been paying attention to widespread research, for example, in layered $MoS_2$, $WS_2$ and non-layered $Ni_3S_2$ and $Co_3S_4$ [14]. As bifunctional electrocatalysts, a variety of earth abundant and economically friendly transition metal-based compounds, including oxides, hydroxides, carbides, sulphides, nitrides and phosphides have been employed towards the overall water splitting reaction [15]. A multi-step process involving proton-coupled transfer of electrons can occur in oxygen evolution reaction. However, the reaction necessitates a large overpotential, which causes energy loss and therefore, lowers the total efficiency of energy conversion [16]. The kinetic bottleneck for the electrochemical decomposition of water that has an addiction to the hydrogen oxygen is the oxygen evolution reaction. To speed up the OER process, several catalysts have been explored [17]. Because of their optimal binding to reaction intermediates, active metal oxide catalysts, such as $IrO_2$ and $RuO_2$, have shown the maximum activity towards OER. However, their rarity, corrosiveness, and high expenses have limited their uses in a wide range of applications [18]. Through numerous studies, it has been established that composites of molybdenum sulphide and nickel sulphide could increase the electrocatalytic activity [19–21]. A lot of work has been carried out into finding reliable, affordable, and effective electrocatalysts for OER [21–23].

In the study, NiS, MoS and NiMoS have been studied systematically as bifunctional catalysts by synthesizing them using similar hydrothermal method and observing their electrocatalytic properties with special emphasis to OER under alkaline condition. It demonstrates that in 1 M KOH for NiS and NiMoS, there is a an overpotential of 160 mV (10 mA $cm^{-2}$) with a Tafel slope of 69.9 mV $dec^{-1}$ and lower overpotential of 124 mV (10 mA $cm^{-2}$) with a Tafel slope of 41.6 mV $dec^{-1}$, and. However, in case of MoS, an overpotential of 210.1 mV (10 mA $cm^{-2}$) and Tafel slope of97.6 mV $dec^{-1}$ have been determined.

## 4.2. Experimental Section

***4.2.1. Materials:*** Nickel chloride ($NiCl_2.4H_2O$), ammonium molybdate ($(NH_4)_6Mo_7O_{24}$), sodium sulphide pentahydrate ($Na_2S.5H_2O$) were purchased from Sigma Aldrich. Nafion was purchased from Arora Matthey Ltd.

***4.2.2. Synthesis:*** The electrocatalysts have been synthesized by hydrothermal method. An aliquot of 1 M nickel chloridewas mixed thoroughly into 1 M sodium sulphide solution. The solution was poured into a teflon-lined stainless steel autoclave and heated to 24 h at 180 °C. For the synthesis of molybdenum sulphide nanoparticles, the same procedure was followed. For the synthesis of nickel molybdenum sulphide nanoparticles, 1 M nickel chloride and 1 M molybdenum sulphide were mixed thoroughly and then, 1 M sodium sulphide was mixed. After the mixture was added, the autoclave was heated to 180 °C for 24 h. The mixture was, then, cooled down to room temperature. After centrifugation of the solution, the obtained product was heated in a hot air oven at 60 °C.

***4.2.3. Characterization of materials:*** The X-ray diffraction (XRD) was performed by using a (Bruker D8 Advance) diffractometer along with a $CuK_\alpha$ radiation source ($\lambda$=1.5418 Å generated at 40 kV). The surface morphology of the electrocatalysts were investigated with SEI INSPECT F 50 FE-SEM. Surface composition of electrocatalysts were analyzed by energy dispersive X-ray spectroscopy (EDX) attached with the same instrument. Transmission electron microscopy was carried out using JEOL JEM 2010 transmission electron microscope. X-ray photoelectron spectroscopy (XPS) was performed with Omicron Nanotechnology XPS 0571 spectrometer.

***4.2.4. Electrochemical Performance***: An aliquot of 90 µL of isopropanol was mixed with 10 µL of 5% nafion solution to produce a 4:1 mixture, which was, then, added to the solution containing 2 mg of electrocatalysts. Subsequently, the mixture was sonicated for 6 h. Next, 5 μL of the catalyst was drop-cast in a graphite carbon electrode with a 0.12 $cm^2$ geometric surface area, which serves as the working electrode for these electrochemical investigations. The cyclic voltammogram of the electrode was measured at a scan rate of 50 mV $s^{-1}$ in a 1 M KOH solution. The Tafel slope of the catalysts has been calculated by taking the plot of overpotential against the current density into consideration. The Tafel slope (b), the current density (j), and the overpotential (η) are related by the equation, $\eta = a + b \log (j)$. Electrochemical impedance spectroscopy (EIS) has been used in these investigations. Capacitance corresponding to the electrical double layer ($C_{dl}$) has been used to calculate the electrochemically active surface area (ECSA) of the catalysts. The slope from $I_c$ *vs.* $\upsilon$ plot, the value of double layer capacitance ($C_{dl}$) can be obtained.

$$I_c = (I_{anodic} - I_{cathodic}) \quad (4.1)$$

$$C_{dl}(F) = \text{slope} = \Delta I_c / 2\Delta\upsilon \quad (4.2)$$

# 4.3. RESULTS AND DISCUSSION

## *4.3.1. XRD analysis*

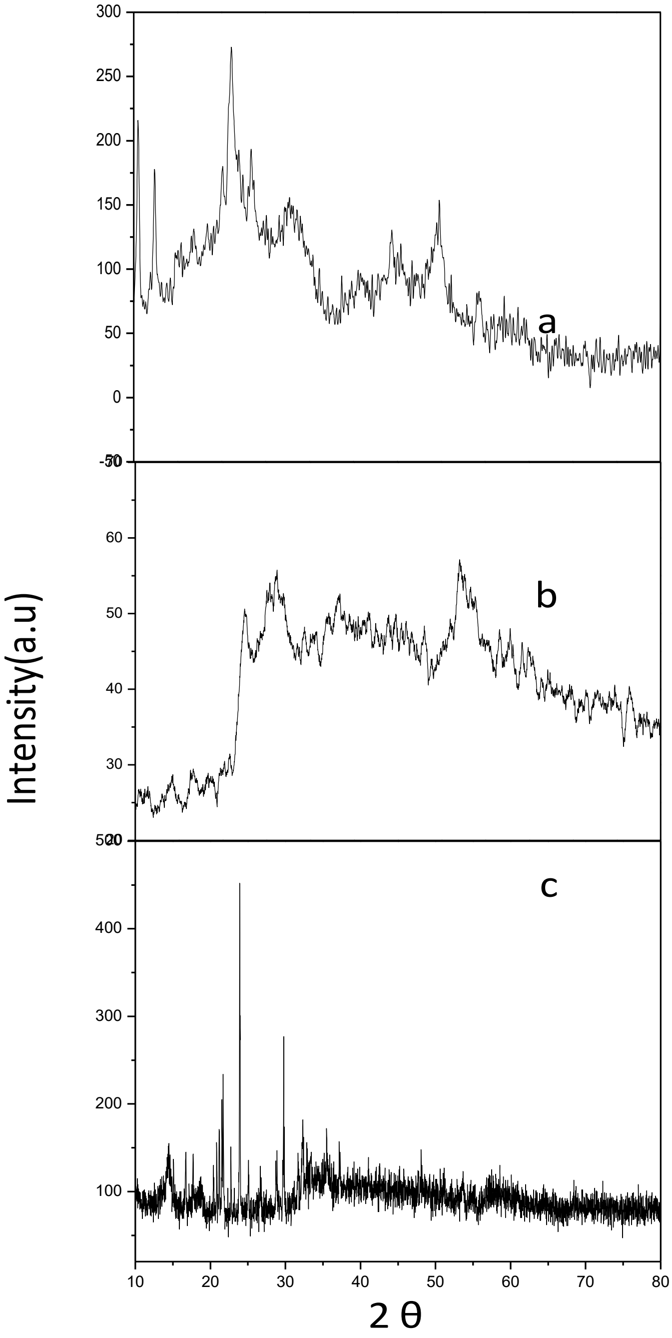

**Fig. 4.1.** X-ray diffraction patterns of (a) NiS, (b) MoS, and (c) NiMoS nanoparticles. The diffraction angle (2θ) along *x*-axis has been expressed in degrees.

X-ray diffraction patterns of NiS, MoS and NiMoS nanoparticles have been presented in Fig. 4.1. It reveals that NiS nanoparticles containing (100), (101), (102), (110) planes (JCPDS Card No.: 02-1280); MoS containing (101), (102) and (110) planes (JCPDS Card No.: 37-1492) and NiMoS containing (101), (111), (102) and (110) planes (JCPDS ard No.: 73-1508).

***4.3.2. SEM analysis:*** Scanning electron micrographs and energy dispersive X-ray spectra of NiS, MoS, and NiMoS nanoparticles have been displayed in Fig. 4.2. NiS exhibit weathered rock-like structures, MoS the solid rock-like structures and NiMoS the chloral flower-like structurestructures. In these superstructures, there are gaps through which the reactants can penetrate and gases can be escaped. The EDS spectra indicate that the atomic composition is Ni:S = 50:50 for NiS, Mo:S = 54:47 for MoS, and Ni:Mo:S = 57:43 for NiMoS.

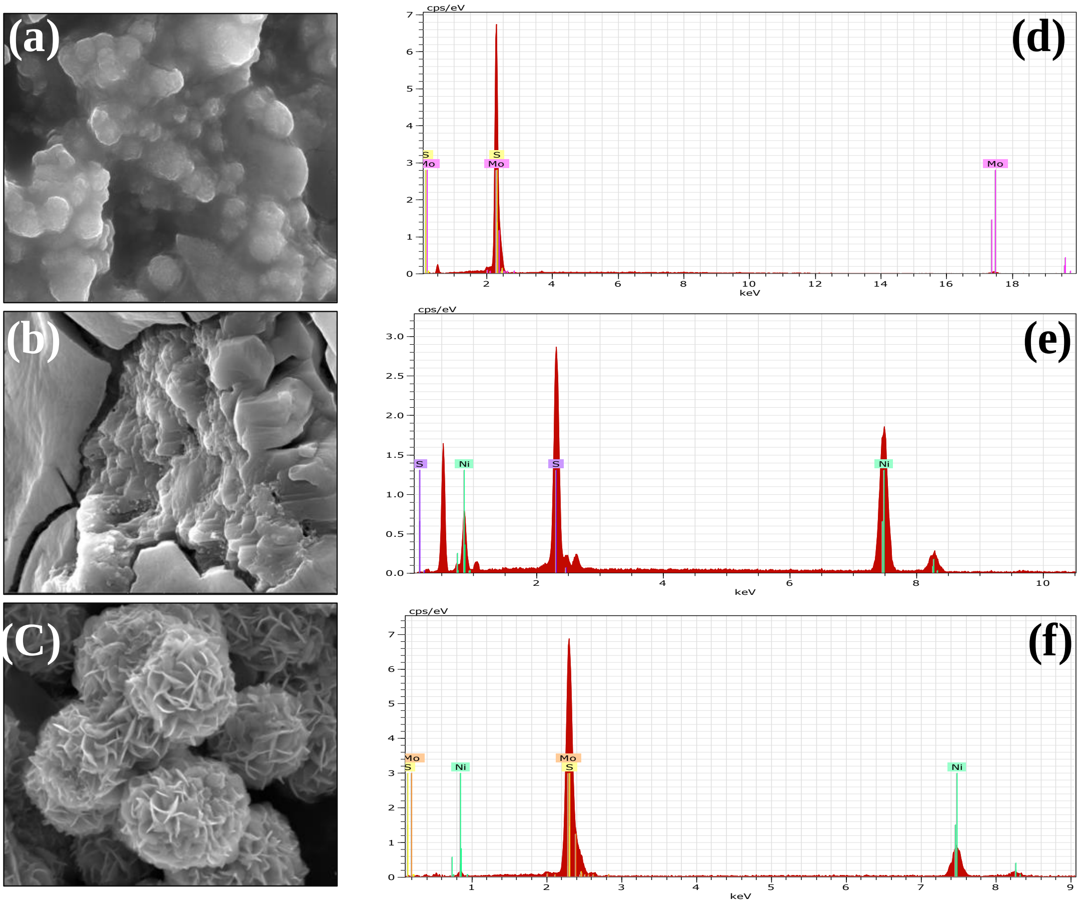

**Fig. 4.2.** (a, b, c) Scanning electron micrographs and (d, e, f) energy dispersive X-ray spectra of NiS, MoS, and NiMoS nanoparticles

### 4.3.3. TEM analysis:

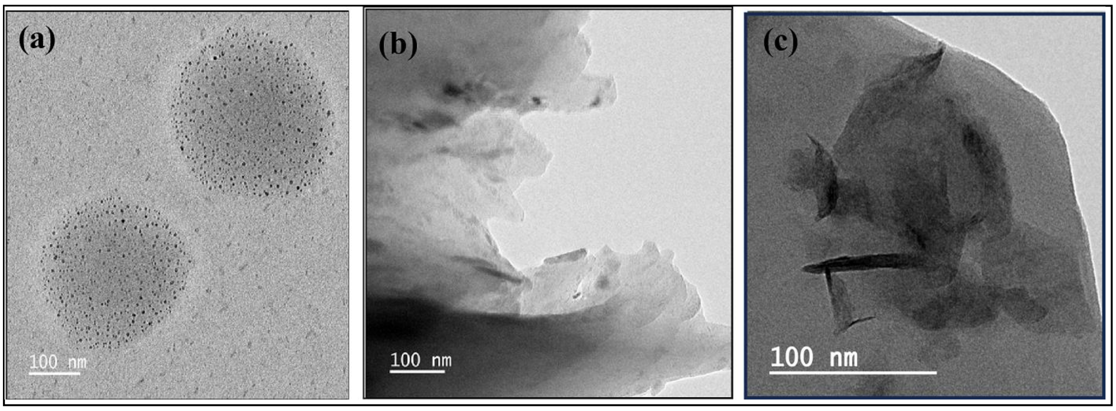

**Fig. 4.3.** Transmission electron micrographs of (a) NiS, (b) MoS and (c) NiMoS nanoparticles

Transmission electron micrographs of NiS, MoS and NiMoS nanoparticles have been displayed in Fig. 4.3. The NiS nanoparticles shows the bubble-like structures, MoS nanoparticles the bricks-like structures and NiMoS nanoparticles the flowers-like structures. The average diameter of the NiS, MoS and NiMoS nanoplarticles are 15±2.8, and 25±3.9, 28±4.3 nm, respectively. Due to decrease in size, surface area increases and therefore, better absorption of ions for NiMoS electrocatalysts rather than NiS and MoS electrocatalysts.

***4.3.4. XPS analysis:*** Using X-ray photoelectron spectroscopy (XPS), the chemical composition and oxidation states of the NiMoS nanoparticles have been examined as has been presented in Fig. 4.4. The two distinct peaks in the Mo 3d spectra, located at 231.9 and 23.1 eV, are related to the binding energies of $Mo3d_{5/2}$ and $Mo3d_{3/2}$, which stand for the oxidation states of the $Mo^{4+}$ in $MoS_2$ or $MoS_3$[24]. The Ni 2p spectrum is displayed by the binding energies of Mo $3d_{3/2}$ and $3d_{5/2}$, which are bound to the oxide states of $Mo^{6+}$. For $Ni2p_{1/2}$ and $Ni2p_{3/2}$, the peaks become broadened with binding energies of approximately 872.7 and 855.2 eV, respectively. These indicate the $Ni^{+}$ and $Ni^{2+}$ oxidation states corresponding to the

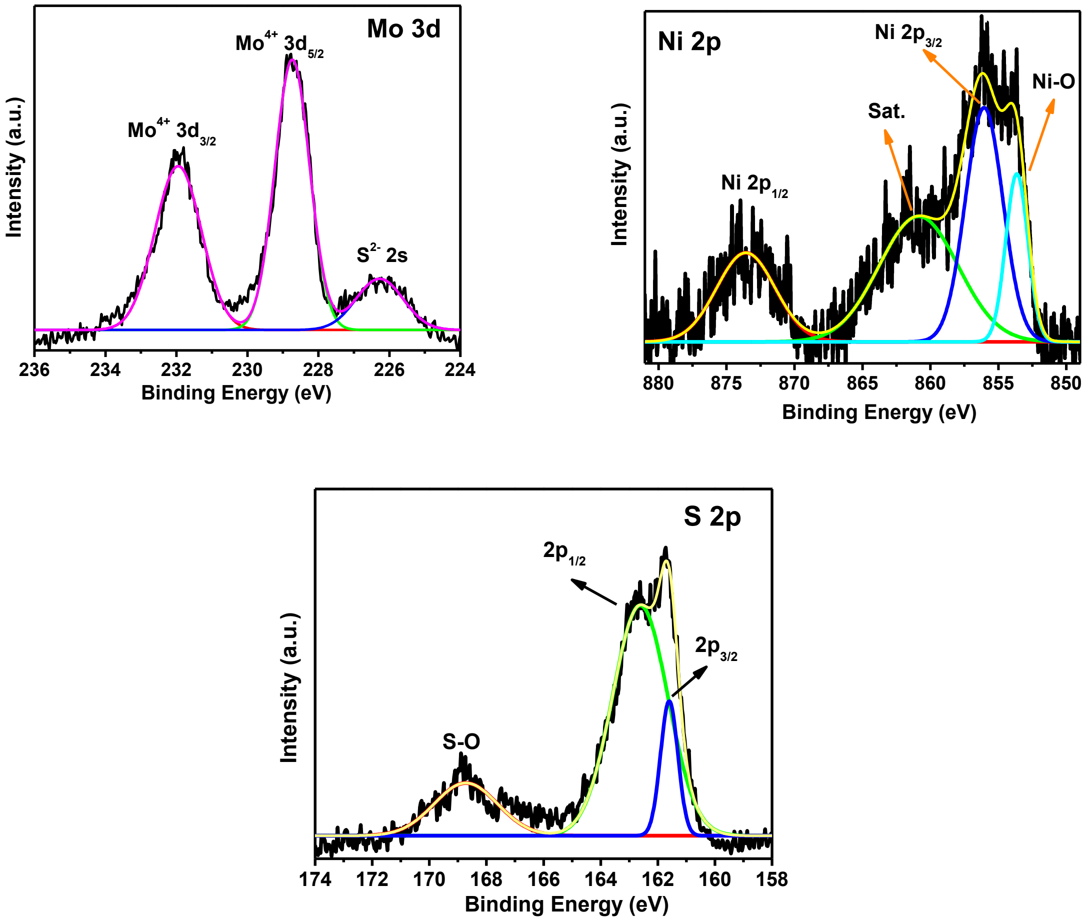

**Fig. 4.4.** X-ray photoelectron spectroscopic analysis of NiMoS nanoparticles

$Ni_3S_2$. The other two satellites peaks situated at 860.9 eV and 879.7 eV corresponds to the nickel and oxygen, respectively. The S 3d spectra shows that binding energies corresponding to the $S2p_{3/2}$ and $S2p_{1/2}$ orbitals are 162.3 and 163.5 eV, respectively. This could be indicative of the presence of bridging $S_2^{2-}$or inarticulate to $S^{2-}$ [25]. It is possible to assign the S 2p spectra with two S 2p doublets, indicating the possibility of the presence of amorphous $Mo_x$ structure and $Ni_xS_y$ in the samples. The peak located at 168.7 eV can be assigned to the remaining $SO_4^{2-}$ species due to the oxidation of surfaces S caused by molybdate oxidation [26].

### *4.3.5. Electrochemical Studies*

The electrocatalytic performance of NiS, MoS, and NiMoS nanoparticles has been studied electrochemically using cyclic voltammetry in a 1.0 M KOH solution at a scan rate of 5 mV $s^{-1}$.

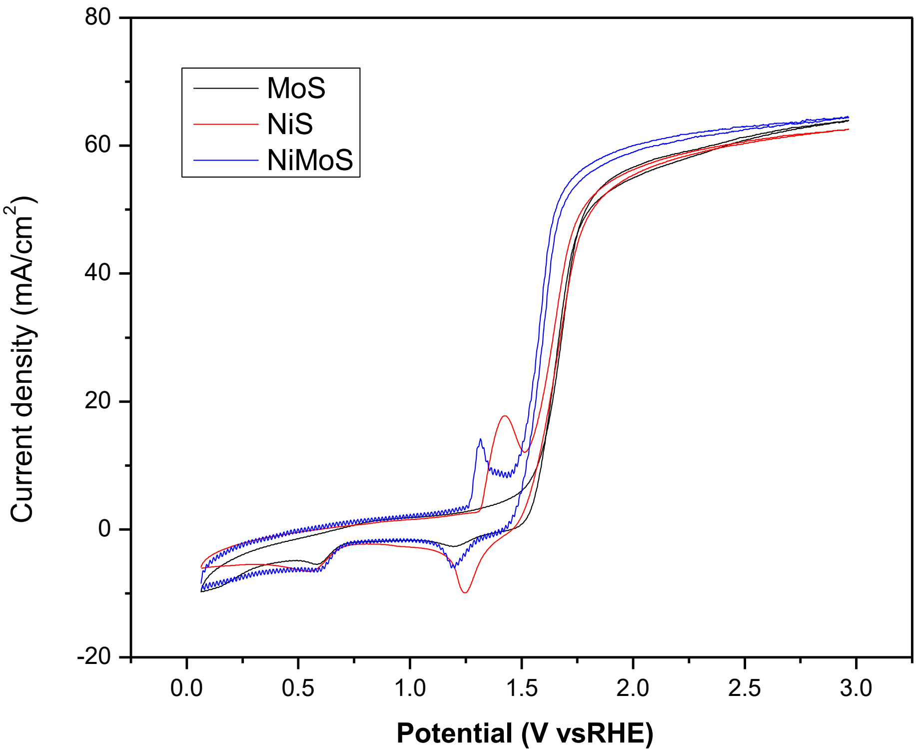

**Fig. 4. 5.** Cyclic voltammograms for NiS, MoS and NiMoS electrocatalysts in 1 M KOH solution

By immersing the electrodes in a 1 M KOH solution, the cyclic voltammograms (Fig. 4.5) of these electrocatalysts for oxygen evolution reaction have been recorded. Oxygen evolution reaction is an electron transfer process that occurs through multiple steps. High potential walls with significant overpotential are required for the reaction to occur [27]. The potential has been measured with respect to AgCl/Ag, $Cl^{-1}$ electrode and normalized with respect to reversible hydrogen electrode (RHE). At 10 mA $cm^{-2}$ current density, the overpotentials are (mV) 160, 210.1 and 124.3 for NiS, MoS, NiMoS based electrodes, respectively.

OER occurs through four steps by $4e^-$ transfer in alkaline medium

$$OH^- + * \longrightarrow OH^* + e^- \quad (4.3)$$

$$OH^* + OH^- \longrightarrow O^* + H_2O + e^- \quad (4.4)$$

$$O^* + OH^- \longrightarrow OOH^* + e^- \quad (4.5)$$

$$OOH^* + OH^- \longrightarrow O_2 + H_2O + e^- \quad (4.6)$$

where * represents the active site of the catalyst and H* and OH* represents the species adsorbed on the catalytic surface.

***4.3.5.1. Tafel plots:*** The Tafel plots corresponding to different electrocatalysts have been presented in Fig 4.6. The values of Tafel slope of NiS, MoS and NiMoS (mV dec$^{-1}$) are 69.9, 97.6 and 41.6 respectively

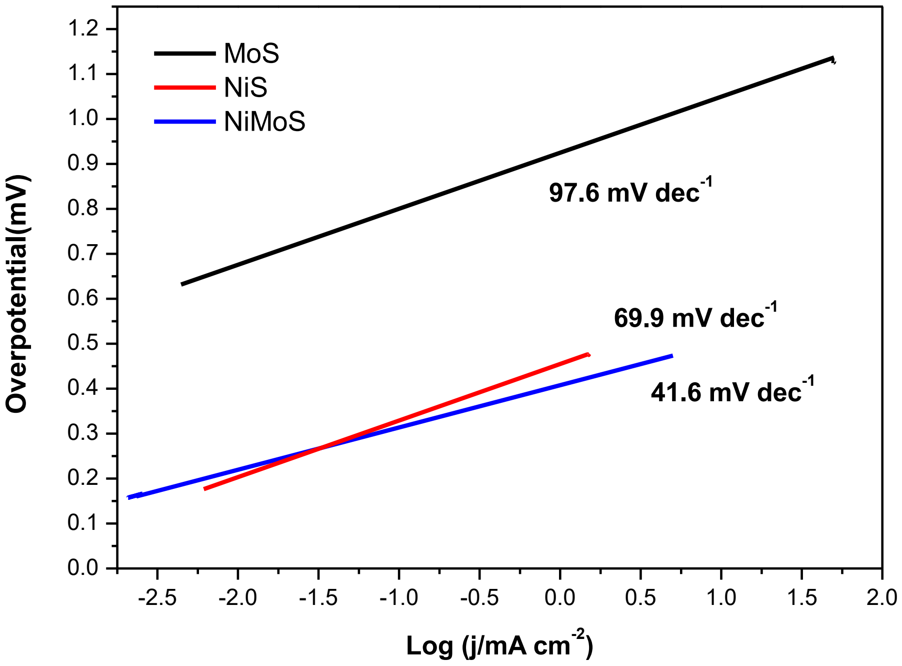

**Fig. 4.6.** Tafel plots of NiS, MoS and NiMoS nanoparticles

### *4.3.5.2. Chronoamperommetry study:*

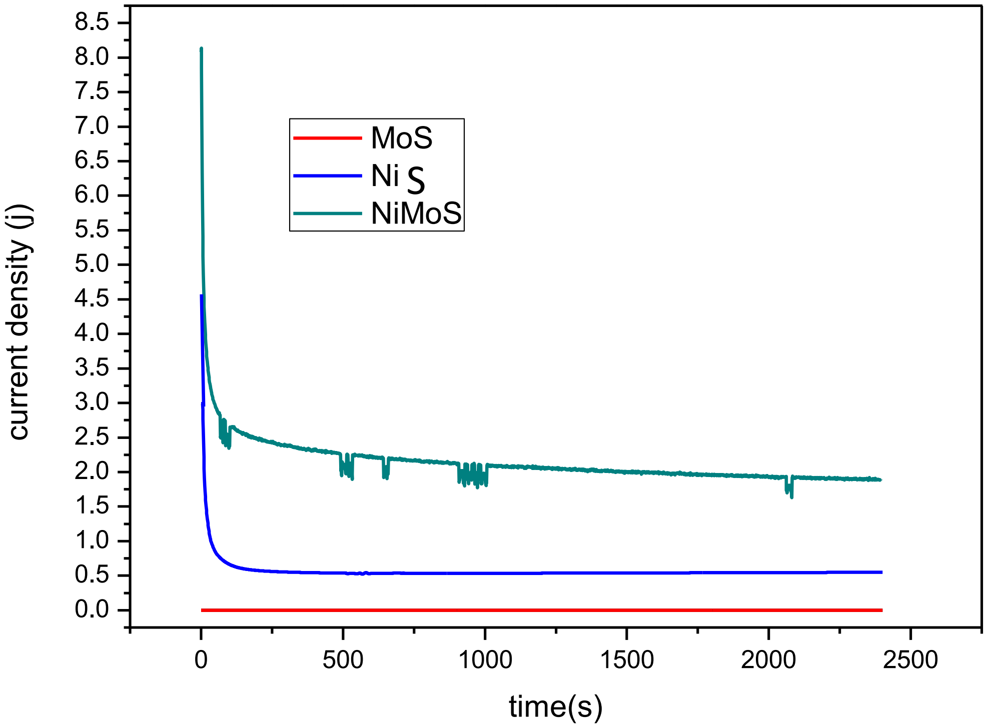

**Fig. 4.7.** Chronoamperometry plots corresponding to NiS, MoS and NiMoS nanoparticles as the electrocatalysts of 1.0 M KOH solution

The chronoamperometry measurement reveals that to study the constancy of the activeness in the catalysts and long term stability during the electrocatalytic performance. The study has been presented graphically in Fig. 4.7. Chronoamperometric studies have been performed with a 0.8V fixed potential for 2500 s in 1 M KOH solution.

### 4.3.5.3. Electrochemical impedence spectroscopy:

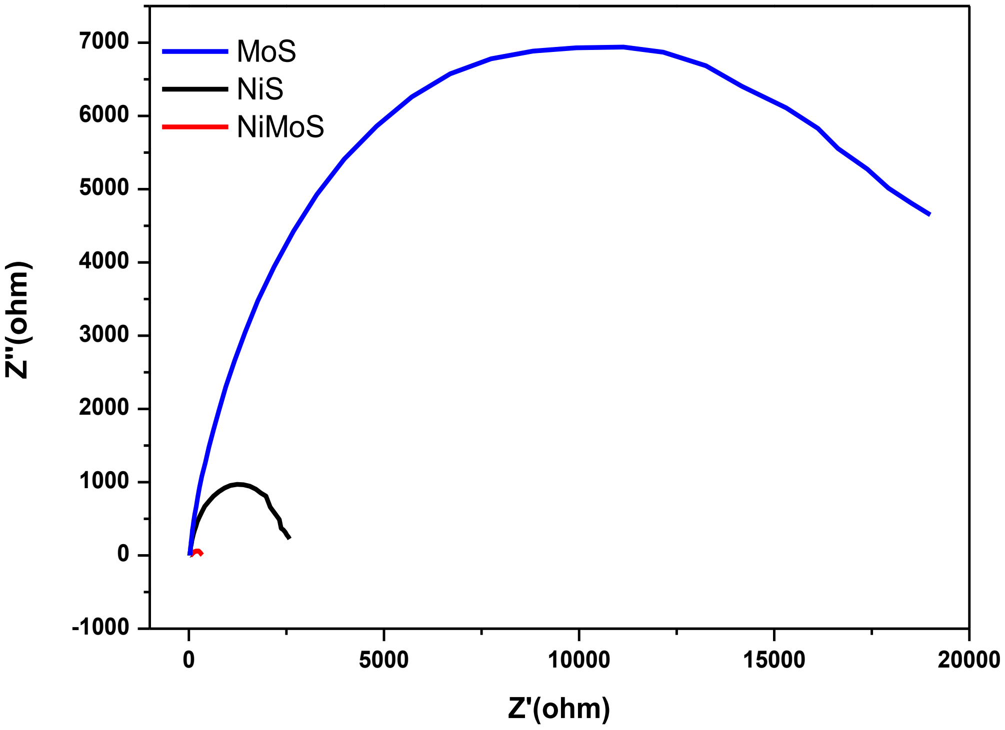

**Fig. 4.8.** Nyquist plots of NiS, MoS and NiMoS nanoparticles

The kinetics of the reaction has been followed through electrochemical impedence spectroscopy (EIS). The Nyquist plots corresponding to NiS, MoS and NiMoS nanoparticles have been presented in Fig. 4.8. From the equivalent circuit model proposed by Randles, $R_s$ signifies the ohmic and ionic resistances at the electrode-electrolyte interface. Moreover, the charge transfer resistance ($R_{ct}$) was started from the lower frequency region in the Nyquist plot. $C_{ct}$ represents the capacitance of the electrical double layer [28]. The values of $R_s$, $R_{ct}$ and $C_{ct}$ have been given in the Table 4.1.

**Table 4.1.** Comparative account of electrochemical impedence spectroscopy of the NiS, MoS and NiMoS electrocatalysts

| Electrocatalyst | Electrolyte | $R_s$ (Ω) | $R_{ct}$ (Ω) | $C_{ct}$ (µF) |
|---|---|---|---|---|
| NiS | 1 M KOH | 67.1 | 2196 | 3.97 |
| MoS | 1 M KOH | 56.3 | 2051 | 2.01 |

| | | | | |
|---|---|---|---|---|
| NiMoS | 1 M KOH | 46.7 | 1424 | 1.05 |

***4.3.5.4. Electrochemical active surface area***: Cyclic voltammetry has been performed using three electrodes in non-Faradaic regions at different scan rates of 10, 20, 50, 70, 90 and 100 mV $s^{-1}$ in 1.0 M KOH solution. The values of double layer capacitance of the electrocatalysts NiS, MoS and NiMoS are 3.04, 1.20 and 3.80 mF $cm^{-2}$, respectively. The ECSA vlues have been calculated by the following equation, ECSA ($cm^2$) = $C_{dl}/C_{s,}$ where $C_s$ is the specific capacitance; the conventional specific charge density, $C_s$ is taken as, 40 µF $cm^{-2}$. The ECSA values for NiS, MoS and NiMoS are 7.6, 3.4 and 9.3 $cm^2$ which indicates the better electrocatalytic activity.

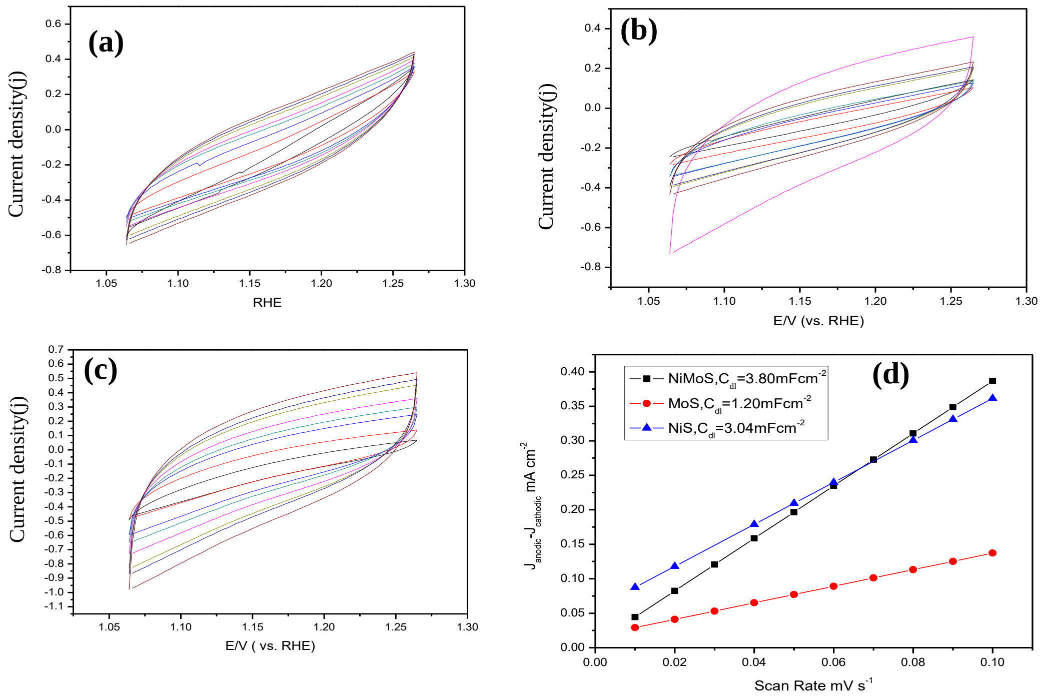

**Fig. 4.9.** Cyclic voltammograms of (a) NiMoS, (b) MoS, and (c) NiS electrodes at different scan rates of 10, 20, 40, 50, 60, 80, 100 mV $s^{-1}$; (d) scan rate dependence of the current densities derived from double layer capacitance measurements of the electrocatalysts

**Table 4.2.** Electrochemical performance of catalysts

| Electrocatalysts | Overpotential for OER (mV) | Tafel slope (mV dec$^{-1}$) | Reference |
|---|---|---|---|
| NiMoS | 124@10 mA cm$^{-2}$ | 41.6 | Present work |
| $Ni_3S_2/MoS_x$ | 215@10 | 67.5 | [2] |
| N-NiMoS | 167@onset potential | 72 | [3] |
| NiMoS | 1.54@10 | 102 | [3] |
| $MoS_2/NiS_2$ | 1.67@10 | 58 | [4] |
|  | 303 mV@10 OER |  |  |
| NiS | 160 | 69.9 | Present work |
| MoS | 210.1 | 97.6 | Present work |

**4.4. Conclusion:** The hydrothermal approach makes it simple to synthesis the catalysts. The OER of the NiMoS nanoparticles at 10 mA cm$^{-2}$ is 124 mV and the Tafel slope is 97.6 mV dec$^{-1}$, and the values of double layer capacitance is 3.72 mF cm$^{-2}$ of the electrocatalysts. The electrochemically active surface area of the nanostructures is 9.3 cm$^{2}$ which indicates the presence of more active sites that have been found to be advantageous for OER. Sulphur-containing transition metals are inexpensive and effective electrocatalysts for the water splitting reaction.The transition metals on affordable and effective electrocatalysts for the total water splitting processes may be initiated by the current work.

## References:

[1] T. E. Mallouk, Water electrolysis: divide and conquer, Nat. Chem. 5 (2013) 362–363.

[2] Y. Z. Xua, C. Z. Yuanb, X. P. Chena, One-pot synthesis nickel sulfide/amorphous molybdenum sulfide nanosheets array on nickel foam as a robust oxygen evolution reaction electrocatalyst, J. Solid State Chem. 256 (2017) 124–129.

[3] K. Wu, X. Wei, D. Li, P. Hu, Nitrogen incorporated nickel molybdenum sulfide as efficient electrocatalyst for overall water splitting, J. Mater. Sci. Tech. 99 (2022) 270–276.

[4] J. Xu, J. Rong, Y. Zheng, Y. Zhu, K. Mao, Z. Jing, T. Z. D. Yang, F. Qiu, Construction of sheet-on-sheet hierarchical $MoS_2$/$NiS_2$ heterostructures as efficient bifunctional electrocatalysts for overall water splitting, Electrochimica Acta385(2021) 138438 1–9.

[5] H. Zhao, W. Wang, Y. Du, Y. Yang, M. Wang, S. Li, R. Chen, Y. Liu, L. Wang, Se doped nickel-molybdenum bimetal sulfide with enhanced electrochemical activity for hydrogen evolution reaction, Int. J. Hydrogen Energy 46 (2021) 10763 –10772.

[6] C. Zhang, M. Antonieti, T. P. Fellinger, $Co_3O_4$ decorated blood derived carbon as a superior bifunctional electrocatalyst, Adv.Funct. Mater. 24 (2014) 7655–7665.

[7] S. D. Tilley, M. Cornuz, K. Sivula, M. Grätzel, Light-induced water splitting with hematite: improved nanostructure and iridium oxide catalysis, Angew. Chem. Int. Ed. 49 (2010) 6405–6408.

[8] T. R. Cook, D. K. Dogtan, S. Y. Reece, Y. Surendranath, T. S. Teets, D. G. Nocera, Solar energy supply and storage for the legacy and nonlegacy worlds, Chem. Rev. 110 (2010) 6474–6502.

[9] E. J. Popczun, C. G. Read, C. W. Roske, N. S. Lewis, R. E. Schaak, Highly active electrocatalysis of the hydrogen evolution reaction by cobalt phosphide nanoparticles, Angew. Chem. Int. Ed. 53 (2014) 5427–5430.

[10] S. Chandrasekaran, L. Yao, L. Deng, C. Bowen, Y. Zhang, S. Chen, Z. Lin, F. Peng, P. Zhang, Recent advances in metal sulphides from controlled fabrication to electrocatalytic, photocatalytic and photoelectrochemical water splitting and beyond, Chem. Soc. Rev. 48 (2019) 4178–4280.

[11] F. Yu, L. Yu, I. K. Mishra, Y. Yu, Z. F. Ren, H. Q. Zhou, Recent developments in earth-abundant and non-noble electrocatalysts for water electrolysis, Mater. Today Phys. 7 (2018) 121–138.

[12] C. Hu, L. Zhang, J. Gong, Recent progress made in the mechanism comprehension and design of electrocatalysts for alkaline water splitting, Energy Environ. Sci. 12 (2019) 2620–2645.

[13] S. Anantharaj, S. R. Ede, K. Sakthikumar, K. Karthick, S. Mishra, S. Kundu, Recent trends and perspectives in electrochemical water splitting with an emphasis on sulphide, selenide, and phosphide catalysts of Fe, Co, and Ni: A review, ACS Catal. 6 (2016) 8069–8097.

[14] L. -A. Stern, L. Feng, F. Song, X. L. Hu, $Ni_2P$ as a Janus catalyst for water splitting the oxygen evolution activity of $Ni_2P$ nanoparticles, Energy Environ. Sci. 8 (2015) 2347–2351.

[15] Z. Kang, H. Guo, J. Wu, X. Sun, Z. Zhang, Q. Liao, S. Zhang, H. Si, P. Wu, L. Wang, Y. Zhang, Engineering an earth abundant element-based bifunctional electrocatalyst for highly efficient and durable overall water splitting, Adv. Funct. Mater. 29 (2019) 1807031 1–10.

[16] J. Wang, X. Yue, Y. Yang, S. Sirisomboonchai, P. Wang, X. Ma, A. Abudula, G. Guan, Earth-abundant transition-metal-based bifunctional catalysts for overall

electrochemical water splitting: A review, J. Alloys Compd. 819 (2020) 153346 1–23.

[17] M. Wang, L. Zhang, Y. Hec, H. Zhu, Recent advances in transition-metal-sulfide-based bifunctional electrocatalysts for overall water splitting, J. Mater. Chem. A 9(2021) 5320–5363.

[18] L. Zhang, T. Wang, L. Sun, Y. Sun, T. Hu, K. Xu, F. Ma, Hydrothermal synthesis of 3D hierarchical $MoSe_2/NiSe_2$ composite nanowires on carbon fiber paper and their enhanced electrocatalytic activity for the hydrogen evolution reaction, J. Mater. Chem. 5 (2017) 19752–19759.

[19] X. Zhang, Y. Y. Zhang, Y. Zhang, W. J. Jiang, Q. H. Zhang, Y. G. Yang, L. Gu, J. S. Hu, L. J. Wan, Phase-Controlled synthesis of 1T-$MoSe_2$/NiSe heterostructure nanowire arrays via electronic injection for synergistically enhanced hydrogen evolution, Small 3 (2019) 1800317 1–6.

[20] X. Zhou, Y. Liu, H. Ju, B. Pan, J. Zhu, T. Ding, C. Wang, Q. Yang, Design and epitaxial growth of $MoSe_{2e}NiSe$ vertical hetero nanostructures with electronic modulation for enhanced hydrogen evolution reaction, Chem. Mater. 28 (2016) 1838–1846.

[21] C. Wang, P. Zhang, J. Lei, W. Dong, J. Wang, Integrated 3D $MoSe_2@Ni_{0.85}Se$ nanowire network with synergistic cooperation as highly efficient electrocatalystsfor hydrogen evolution reaction in alkaline medium, Electrochim. Acta 246 (2017) 712–719.

[22] K. Premnath, P. Arunachalam, M. S. Amer, J. Madhavan, A. M. Al-Mayouf, Hydrothermally synthesized nickel molybdenum selenide composites as cost effective and efficient trifunctional electrocatalysts for water splitting reactions, Int. J. Hydrogen Energy 44 (2019) 22796–22805.

[23] S. Han, Y. Ai, Y. Tang, J. Jiang, D. Wu, Carbonized polyaniline coupled molybdenum disulfide/graphene nanosheets for high performance lithium ion battery anodes, RSC Adv. 5 (2015) 96660–96664.

[24] N. Liu, L. Yang, S. Wang, Z. Zhong, S. He, X. Yang, Q. Gao, Y. Tang, Ultrathin $MoS_2$ nanosheets growing within an in-situ-formed template as efficient electrocatalysts for hydrogen evolution, J. Power Sources 275 (2015) 588–594.

[25] C. Liu, K. Wang, X. Zheng, X. Liu, Q. Liang, Z. Chen, Rational design of $MoSe_2$-NiSe@carbon heteronano structures for efficient electrocatalytic hydrogen evolution in both acidic and alkaline media, Carbon 139 (2018) 1–9.

[26] L. L. Feng, G. Yu, Y. Wu, G. D. Li, H. Li, Y. Sun, T. Asefa, W. Chen, X. Zou, High index faceted $Ni_3S_2$ nanosheet arrays as highly active and ultrastable electrocatalysts for water splitting, J. Am. Chem. Soc. 137 (2015) 14023–14026.

[27] A. Ghosh, M. Mondal, R. N. Manna, A. Bhaumik, Targeted synthesis of a metal-free thiadiazolate based nitrogen and sulfur rich porous organic polymer for an unprecedented hydrogen evolution in the electrochemical water splitting, J. Colloid Interface Sci. 658 (2024) 415–424.

[28] A. Ghosh, S. Shyamal, A. Palui, R. N. Manna, S. Mondal, M. Jana, A. Ghosh, A. Bhaumik, Photoelectrochemical water oxidation over novel semiconducting zinc-based metal−thiolate framework, ACS Appl. Mater. Interfaces 14 (33) (2022) 37699–37708.

# CHAPTER-IV

## HYDROTHERMALLY SYNTHESIZED NICKEL SELENIDE, MOLYBDENIUM DISELENIDE AND NICKEL MOLYBDENIUM SELENIDE ARE COST EFFECTIVE AND BIFUNCTIONAL ELECTROCATALYSTS FOR WATER SPLITTING REACTION

# *CHAPTER 4*

# Hydrothermally synthesized nickel selenide, molybdeniumdiselenide and nickel molybdenium selenide are cost effective and bifunctional electrocatalysts for Water splitting reaction

## 5.1. Introduction

The intercalation of diverse guests into chalcogenide hosts has been the focus of numerous research investigation over the last few decades [1–6]. Certain compounds, such as nickel selenide ($NiSe_2$) and iron selenide ($FeSe_2$), have been found to exhibit large cathodic current densities at lower overpotentials along with good electrocatalytic activity. High cathodic current densities and low overpotentials boost the electrocatalytic activity of the active sites, which are consisting of Ni or Fe molecules [7–13]. The transition metal based selenides have been considered as one of the most electrifying class of electrocatalysts that performed opponents of noble metal based electrocatalysts [14–19]. The variety of nickel selenides, such as NiSe [20–23], $Ni_{0.85}Se$ [24], $NiSe_2$ [25–27], and $Ni_3Se_2$ [28–29], have been extensively observed for the HER and OER processes. Materials, such as FeSe, CuSe, MoSe, CoSe and their corresponding alloys have been reported earlier to water splitting reactions and other applications related to energy demands [30–35]. Molybdenum selenide ($MoSe_2$) is an another gifted electrocatalyst with better electrocatalytic performance, low cost, and earth abundant elements [36–40]. $RuO_2$ or $IrO_2$ has been found to be the best electrodes for OER [41–42]**.** Platinum has been proven to be the most valuable HER electrocatalyst reported so far in the literature [43–44].

In the present study, it is reported that molybdenum selenides, nickel selenides and their composites could enhance the electrocatalytic activity [45–51]. The electrocatalytic water splitting reaction of the NiMoSe electrocatalysts towards OER at 10 $mAcm^{-2}$ overpotential with respect to RHE is 165 mV and the Tafel slope value is 83 mV $dec^{-1}$.

## 5.2. Experimental Section

***5.2.1. Reagents:*** Nickel chloride ($NiCl_2.4H_2O$), ammonium molybdate ($(NH_4)_6Mo_7O_{24}$), sodium selenite ($Na_2SeO_3$) and hydrazinehydrate ($N_2H_4.H_2O$) were purchased from

Sigma Aldrich and were used as received. Nafion was purchased fromArora Matthey Ltd.and was used without further purification.

### *5.2.2. Instrumentation*

The morphologies of the selenide-based materials were investigated using scanning electron microscopy (SEM) on a SEI INSPECT F 50 FE-SEM and their elemental compositionswere assessed using energy-dispersive X-ray spectroscopy (EDS) on an EDS spectrometer. HRTEM images of the specimen were collected on a JEOL JEM 2010 transmission electron microscope. The hydrothermally synthesized crystal structure of synthesized nanoparticles was investigated by X-ray diffraction (XRD) study that was performed using a Bruker D8 Advance diffractometer equipped with a $CuK_\alpha$ radiation source ($\lambda$=1.5418 Å generated at 40 kV and 40 mA.). The chemical valence was characterized by X-ray photoelectron spectroscopy (XPS) performed in the Omicron Nanotechnology XPS 0571 spectrometer. Fourier transform infrared (FTIR spectroscopic study was performed by PerkinElmer instrument.

### *5.2.3. Synthesis of nickel molybdenium selenide nanoparticles*

The electrocatalysts were synthesized by following hydrothermal protocol. An aliquot of 1 M nickel chloride was mixed thoroughly to 1 M sodium selenite solution. An equivalent amount of hydrazine hydrate was added in the solution. The solution was poured into a stainless steel autoclave and heated at 180 °C for 24 h. For the synthesis of molybdenium selenide nanoparticles, the same protocol was applied. For synthesis of nickel molybdenium selenide nanoparticles, 1 M nickel chloride and 1 M molybdenium selenide were mixed thoroughly and then, 1 M sodium selenite was reduced by hadrazine hydrate. After the mixture was agitated and sealed into an autoclave and the mixture was heated at 180 °C for 24 h. The mixture was, then, allowed to cool down to room temperature. After centrifugation of the mixture, the resulting product was agitated at 60 °C in a hot air oven.

## 5.3. Characterization of materials

### *5.3.1. Electrochemical performance*

The bifunctional activity of the electrocatalysts has been investigated in water splitting that involves the individual testing of oxygen evolution reaction under three electrode setups (Autolab). In this experiment, Ag/AgCl electrode has been used as the reference electrode, Pt foil as the counter electrode, and graphite electrode as the working electrode. The working electrode has a geometric surface area of 0.12 $cm^{-2}$. Now, 2 mg of the powdered catalystshas been dissolved in 80 µL of isopropanol and 20 µL of 5% nafion to produce a mixture of 4:1. The solution was, then, sonicated for 2 h and subsequently, 5 µL mixture was dropped over the working electrode. The following equation,

$$E_{RHE} = E_{Ag/AgCl} + 0.197 + (0.059 \times pH) \tag{5.1}$$

has been used to make the electrode potentials equivalent to the reversible hydrogen electrode (RHE).

The Tafel equation, expressed as, $\eta = a + b \log j$, indicates the electrokinetic character of OER. In this equation, $\eta$ is the overpotential, j represents the current density, a stands for the Tafel constant, and b for the Tafel slope. The non-faradic portion of cyclic voltammograms at various scan rates ($\upsilon$) has been used to calculate the electrochemical active surface area. The charging current ($I_c$) has been calculated from the ECSA data. We have calculated the value of double layer capacitance ($C_{dl}$) by taking the slope from the $I_c$ *vs.* $\upsilon$ plot into consideration.

$$I_c = (I_{anodic} - I_{cathodic}) \tag{5.2}$$

$$C_{dl}\,(F) = \text{slope} = \Delta I_c / 2\Delta\upsilon \tag{5.3}$$

## 5.4. Results and discussion

### *5.4.1. Structural characterization*

### *5.4.1.1. XRD Analysis*

X-ray diffraction patterns of NiSe, $MoSe_2$ and NiMoSe nanoparticles have been displayed in Figure 5.1. For $MoSe_2$, the prominent peak appears at 29° corresponding to the (100) planes. Other peaks appearing at 41°, 47°, 56° and 65° angles can be assigned to the planes of (006), (105), (110), (200) respectively (JCPDS card number:29-0914. The hexagonal NiSe nanoparticles containing diffraction peaks having 2θ values 33.32°, 44.94°, 50.77° and 62.09° corresponding to planes (101) ,(102), (110) and (103) planes, respectively (JCPDS card number: 18-0888).For NiMoSe nanoparticles containing diffraction peaks having 2 θ values 44.5, 51.9, 76.4 corresponding to planes (111), (200), (220) planes.

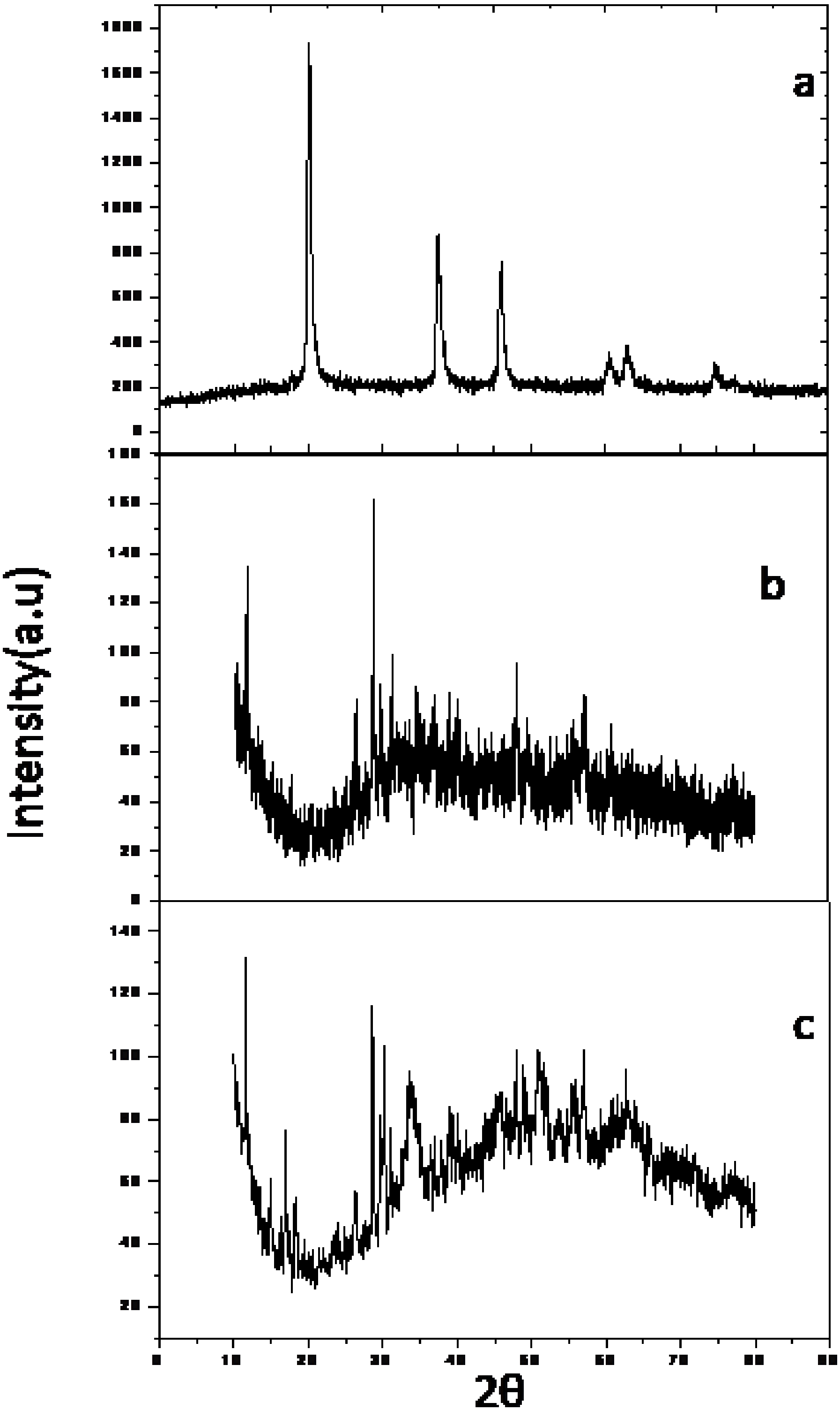

**Fig. 5.1.** X-ray diffraction patterns of (a) NiSe, (b) $MoSe_2$ and (c) NiMoSe nanoparticles. The diffacion angle 2θ along has been expressed in degrees.

### *5.4.1.2. FTIR spectroscpy*

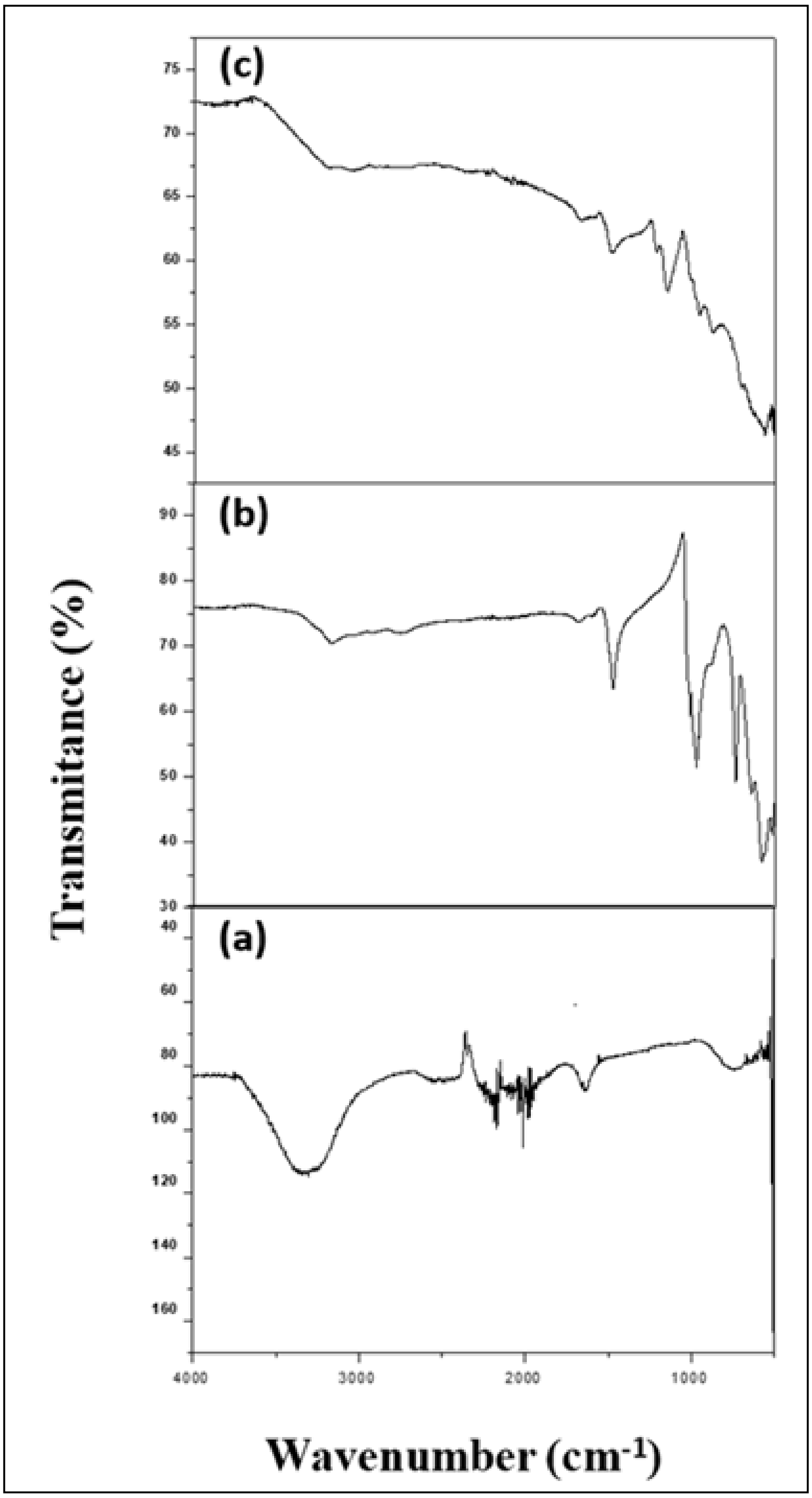

**Fig. 5.2.** Fourier transform infrared spectroscopy of (a) NiSe, (b) $MoSe_2$ and (c) NiMoSe nanoparticles

To understand the nature of the functional groups of the synthesized Ni and Mo based electrocatalysts, Fourier transform infrared spectroscopy spectroscopy has been used. FTIR spectra of NiSe, $MoSe_2$, and NiMoSe are shown in Fig. 5.2. The characteristic peaks observed at 601 $cm^{-1}$ and 930 $cm^{-1}$ are related to the Mo–Se and Se–Se molecules; the peaks are shown in 1412 and 1617 $cm^{-1}$ were indicated the Mo–O functional groups; the broad peak is investigated at 1114 $cm^{-1}$ for the aromatic ring C–H stretching and bending mode; the peak is observed at 715 $cm^{-1}$ is to bending out of plane; the $MoSe_2$ nanosheet peaks are shifted slightly towards lower the intensity. These results are clearly confirmed by the accurate chemical interaction in the presence of the functional groups that can change in the structural phase of the nanostructures.

### *5.4.1.3. SEM analysis*

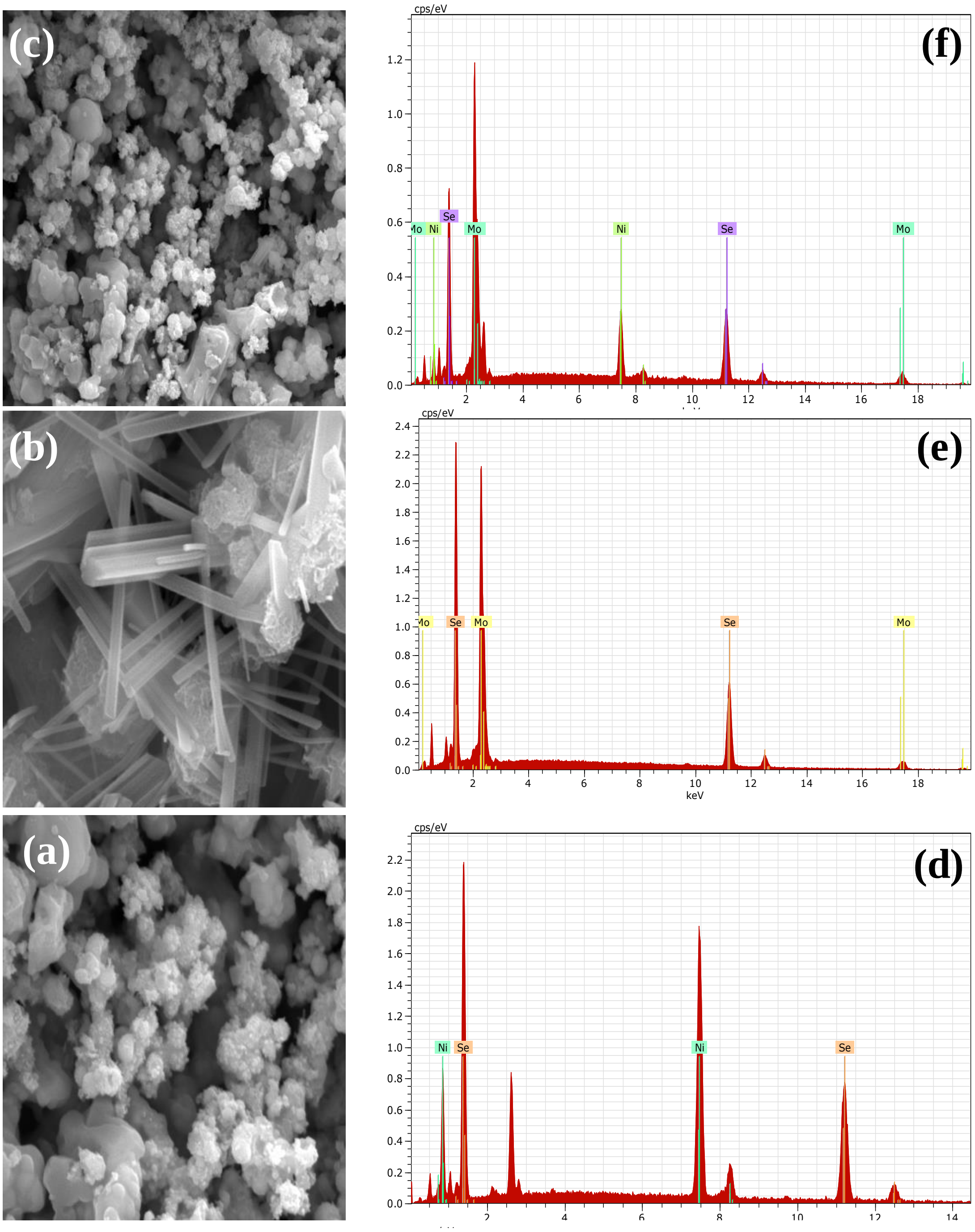

**Fig. 5. 3.** (a, b, c) Scannng electron micrographs and (d, e, f) energy dispersive X-ray spectrum of NiSe, $MoSe_2$ and NiMoSe nanoparticles

Scannng electron micrographs and energy dispersive X-ray spectrum of NiSe, $MoSe_2$ and NiMoSe nanoparticles have been shown in Fig. 5. 4. Using SEM, the morphologies of the synthesized samples were examined. The dense and compact coral-like surface shape of the NiMoSe composites can be thought to be more advantageous for an effective electron transport process [33]. The EDS spectra indicate that the atomic compositions as Ni:Se = 41:54 for NiSe, Mo:Se= 54:45 for MoSe, and for Ni:Mo:Se = 12:49:38 NiMoSe composites.

### 5.4.1.4. TEM analysis

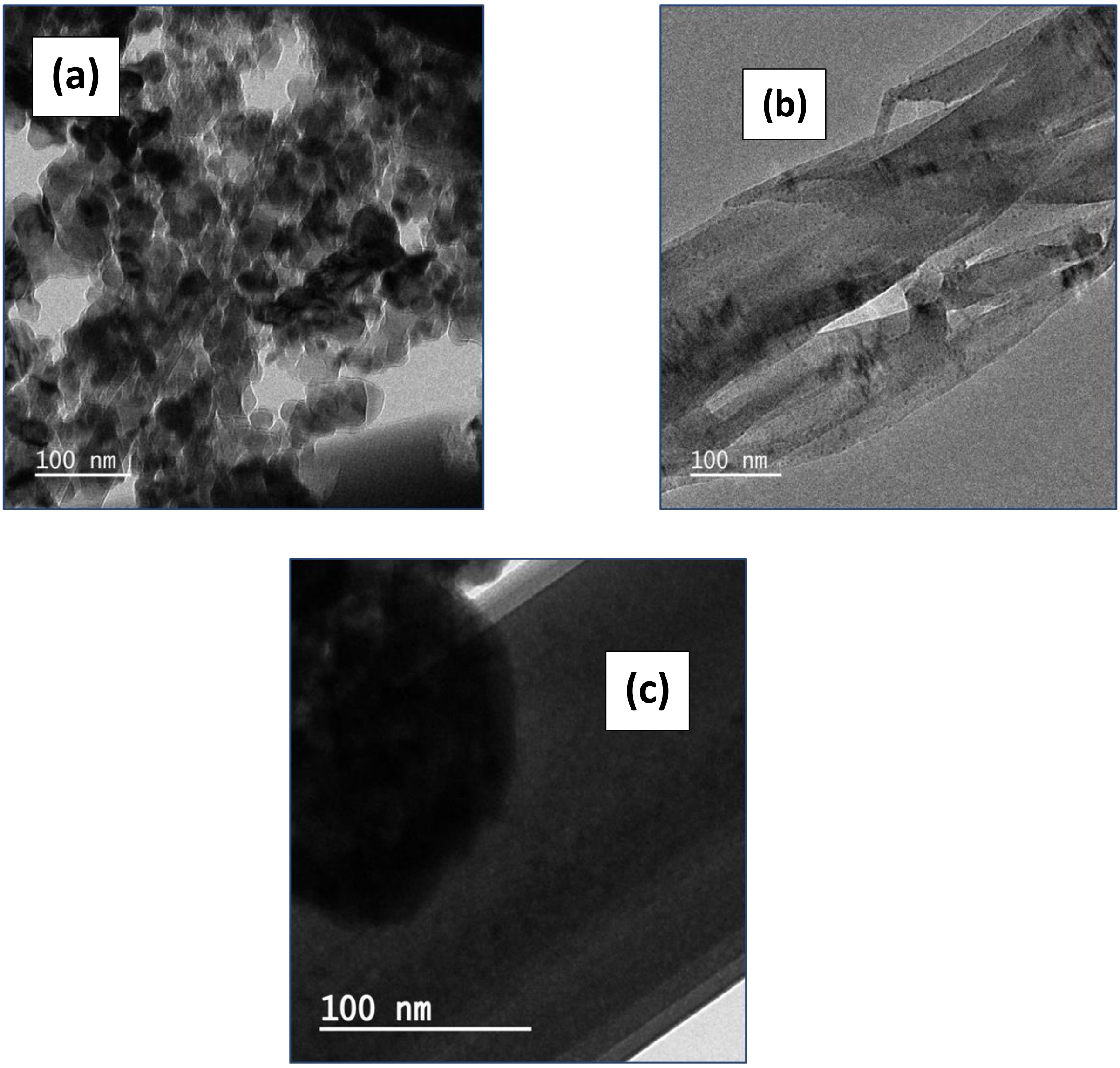

**Fig. 5.5.** Transmission electron micrographs of (a)NiSe, (b)$MoSe_2$ and (c)NiMoSe nanoparticles

Transmission electron micrographs of NiSe, $MoSe_2$ and NiMoSe nanoparticles have been exhibited in Fig. 5.4. It is observed that NiSe possesses quantum-dot like structures, and $MoSe_2$, NiMoSe the spherical structures. The average diameter of the NiSe, $MoSe_2$, and NiMoSe nanostructures are 16±2.3, 8±1.6, and 24 ±2.7 nm, respectively.

### *5.4.2. Electrochemical Studies*

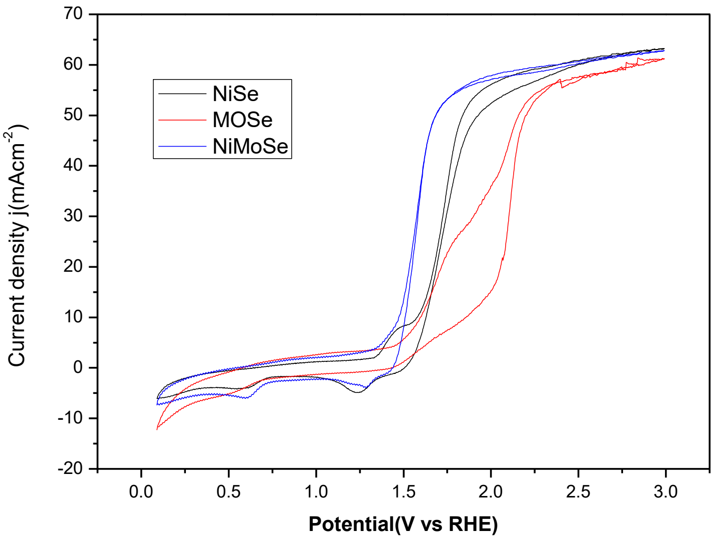

**Fig. 5.6.** Cyclic voltammograms for NiSe, $MoSe_2$ and NiMoSe electrocatalysts in 1 M KOH solution

#### *5.4.2.1. Oxygen Evolution Reaction (OER)*

The inherent potential corresponding to the OER activity has been observed in 1 M KOH solution at pH~14. At a scan rate of 50 mV $s^{-1}$, the OER activity was conducted in a cyclic voltammograms in the potential regime of +1 to + 2.8 V with respect to RHE. For NiSe, $MoSe_2$, and NiMoSe, the measured current density at 10 mA $cm^{-2}$ is 180, 210, and 165 mV, respectively. Oxygen evolution reaction can be considered as a multi-step electron transfer reaction that requires an overpotential, or high potential energy barrier.

$$OH^- + * \longrightarrow OH^* + e^- \qquad (5.4)$$

$$OH^* + OH^- \longrightarrow O^* + H_2O + e^- \qquad (5.5)$$

$$O^* + OH^- \longrightarrow OOH^* + e^- \qquad (5.6)$$

$$OOH^* + OH^- \longrightarrow O_2 + H_2O + e^- \qquad (5.7)$$

In an alkaline medium, OER happens in four steps by 4 electron transfer, where * denotes the active site of the catalyst and H* and OH* represent the species adsorbed on the surface [52].

The Tafel diagram provides the mechanistic pathway for the OER reaction. Fig. 5. 6 displays the Tafel slopes that have been measured for the NiSe, $MoSe_2$, and NiMoSe . The plot of the logarithm of current density against the overpotential has been used to calculate the Tafel slope. The polarization plots provide the current density j, which is needed to evaluate the Tafel plot.

The Tafel equation states that slope is the relationship between current density, j and the overpotential, $\eta$. For NiSe, $MoSe_2$, and NiMoSe nanoparticles, the Tafel slopes (mV $dec^{-1}$) have been enumerated as 126, 96, and 83 respectively. Tafel slope for NiMoSe suggests that the electrochemical reaction occurs through a Volmer-Heyrovsky process. Therefore, in the current work, the electrocatalysts exhibit improved activity towards the oxygen evolution reaction in 1 M KOH solution.

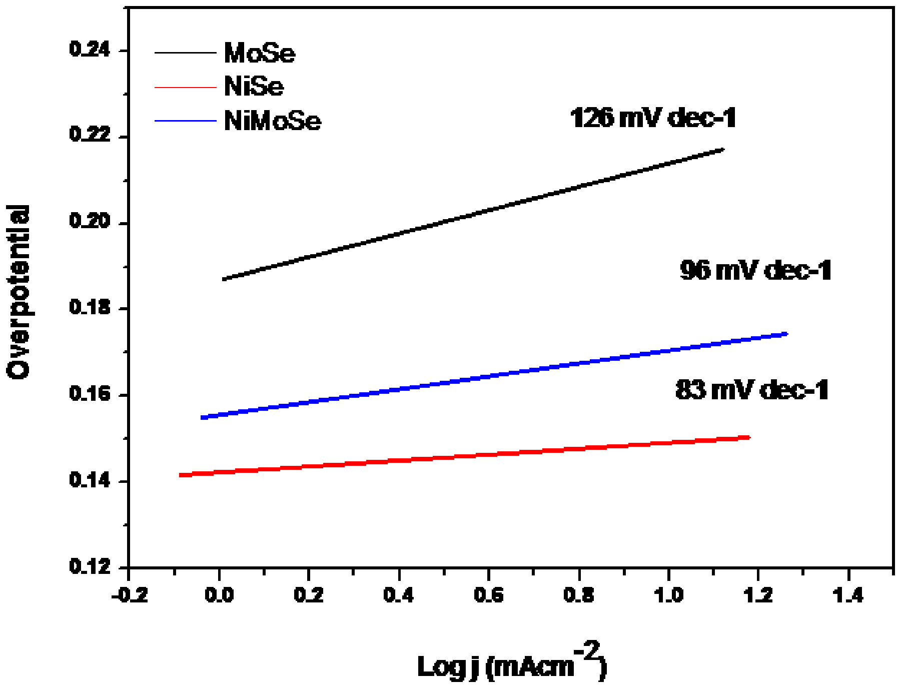

**Fig. 5.7.** Tafel plots corresponding to oxygen evolution reaction for NiSe, $MoSe_2$ and NiMoSe nanoparticles. The overpotential along the *y*-axis has been expressed in mV.

### *5.4.2.2. Chronoamperommetry study:*

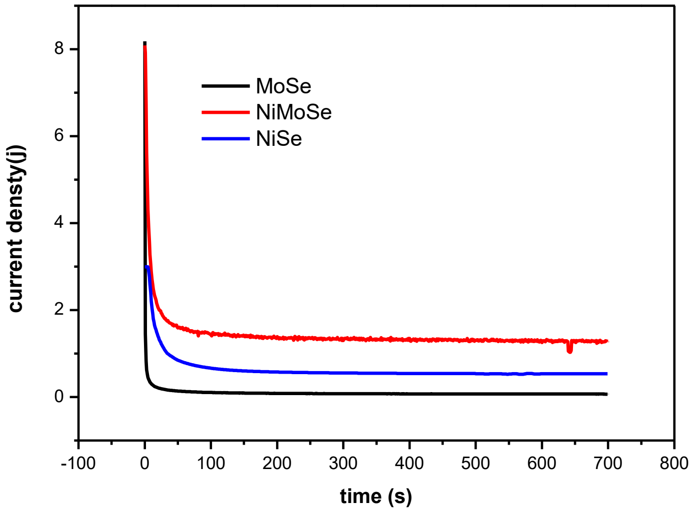

**Fig. 5.8.** Chronoamperommetry study of the electrocatalysts in 1.0 M KOH solution

Fig. 5.7 shows the chronoamperometric stability of the three electrocatalysts against the oxygen evolution reaction over a continuous period of time at a fixed potential of 0.8 V. These investigations show that consistency occurs throughout the electrochemical process.

***5.4.2.3. Electrochemical active surface area:*** Cyclic voltammograms at various scan rates, ranging from 10 mV $s^{-1}$ to 100 mV $s^{-1}$, have been displayed in Fig. 5.8. The electrochemical active surface has been computed from the non-faradic region. The values of double layer capacitance ($C_{dl}$) of the NiSe, $MoSe_2$ and NiMoSe nanoparticles have been calculated as 2.6, 1.9 and 3.8 mF $cm^{-2}$, respectively under the non-faradic potential region (1.06 V- 1.26 V). The ECSA values for NiSe, $MoSe_2$ and NiMoSe have been enumerated from the equations are 6.5, 4.8 and 9.5 $cm^2$ (ECSA ($cm^2$) = $C_{dl}/C_s$, specific charge density, $C_s$ = 40 μF $cm^{-2}$).

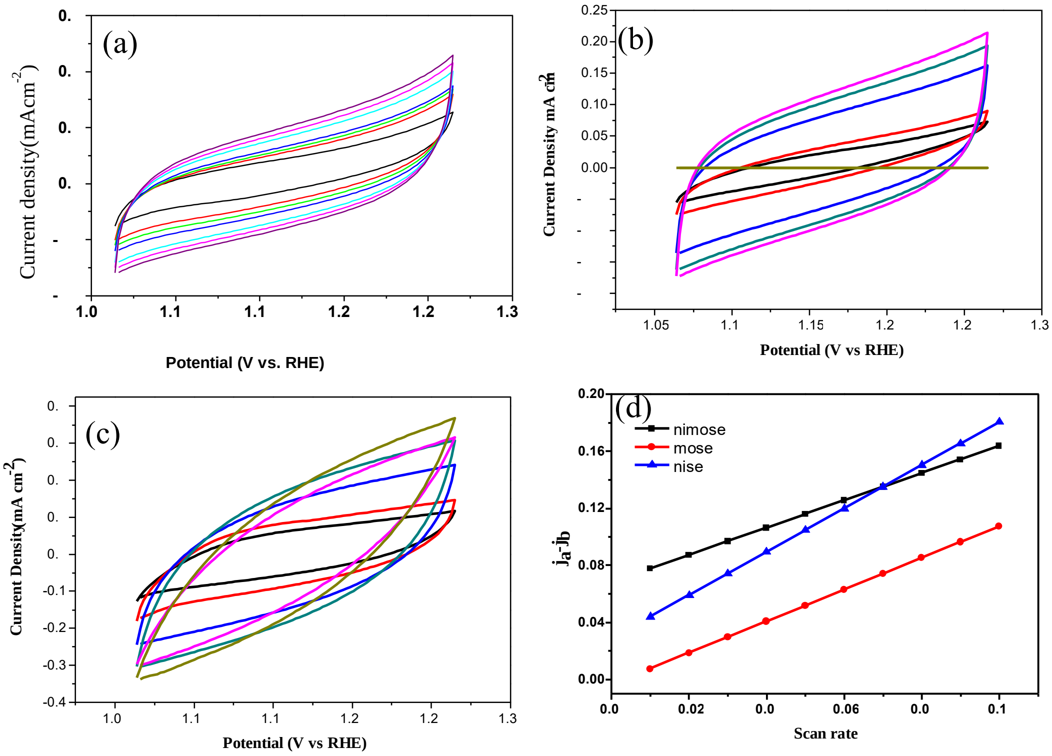

**Fig. 5.9.** Cyclic voltammograms of (a) NiSe, (b) $MoSe_2$ and (c) NiMoSe electrodes at different scan rates of 10, 20, 40, 50, 60, 80, 100 mV $s^{-1}$; (d) scan-rate dependences of the current densities derived from double-layer capacitance measurements of the electrocatalysts.

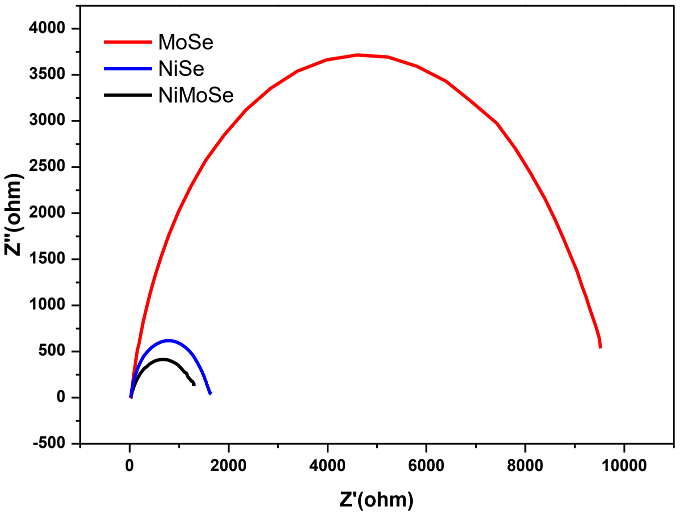

**Fig. 5. 10.** Nyquist plots of NiSe, $MoSe_2$ and NiMoSe nanoparticles

Electrochemical impedance spectroscopy has been used to study the kinetics of the reaction. The Nyquist plots of NiSe, $MoSe_2$ and NiMoSe nanoparticles have been shown in Fig. 5.9. From the equivalence circuit model proposed by Randles, where, $R_s$ is solution resistance can be calculated from the intersection of real axis which is *x*-axis corresponding to the high frequency region. $R_{ct}$ represents the ohmic and ionic resistances at electrode-electrolyte interface which is found from lower frequency state of the Nyquist plot. $C_{ct}$ represents the double layer capacitance value from these equivalence circuit model. Electrochemical impedance spectroscopic results corresponding to NiSe, $MoSe_2$ and NiMoSe electrocatalysts have been presented in Table 5.1.

**Table 5.1.** Electrochemical impedance spectroscopic results corresponding to NiSe, MoSe2 and NiMoSe electrocatalysts

| Electrocatalyst | Electrolyte | $R_s$ (Ω) | $R_{ct}$ (Ω) | $C_{ct}$ (μF) |
|---|---|---|---|---|
| NiSe | 1 M KOH | 30.87 | 8597 | 3.248 |
| $MoSe_2$ | 1 M KOH | 26.25 | 6258 | 2.129 |
| NiMoSe | 1 M K0H | 24.01 | 1815 | 1.264 |

A comparative account of the electrocatalysts with some other similar catalysts towards oxygen evolution reaction have been shown in Fig. 5.2.

**Table 5. 2.** A comparative account of the electrocatalysts towards oxygen evolution reaction

| Electrocatalysts | Overpotential for OER (mV) | Tafel slope (mV $dec^{-1}$) | Reference |
|---|---|---|---|
| NiMoSe | 124@10 mA $cm^{-2}$ | 96 | Present work |
| $Ni_{0.5}Mo_{0.5}Se$ | 1.57 V @ 10 mA $cm^{-2}$ | | [1] |
| MoeNieSe@NF | 397 mV@ 10 mA $cm^{-2}$ | 44.9 | [53] |

| | | | |
|---|---|---|---|
| NiSe | 160 | 83 | Presnt work |
| MoSe | 210.1 | 126 | Present work |

## 5.5. Conclusions

In conclusion, the electrocatalysts have been successfully synthesized by the hydrothermal method and their electrocatalytic activities have been studied. The low overpotential value of the nanoparticle is 165 mV with a lower Tafel slope of 83 mV $dec^{-1}$ and electrochemical active surface area of 9.5 $cm^{-2}$ that makes it a preferable catalysts towards oxygen evolution reaction. The hydrothermally synthesized NiMoSe nanoparticles can be used as electrocatalysts for its low cost values and ease of synthesis in the labarotary that can be useful in the water splitting reactions.

## References

[1] K. Premnath, P. Arunachalam, M. S. Amer, J. Madhavan, A. M. Al-Mayouf, Hydrothermally synthesized nickel molybdenum selenide composites as cost-effective and efficient trifunctional electrocatalysts for water splitting reactions, Int. J. of hydrogen energy 4 (2019) 22796–22805

[2] A. Sobhani, M. Salavati-Niasari, Synthesis and characterization of CdSe nanostructures by using a new selenium source: effect of hydrothermal preparation conditions, Mater Res Bull 53 (2014) 7–14.

[3] A. Sobhani, M. Salavati-Niasari, A new simple route for the preparation of nanosized copper selenides under different conditions, Ceram. Int. 40 (2014) 8173–8182.

[4] M. Salavati-Niasari, B.Shoshtari-Yeganeh, M. Bazarganipour, Facile synthesis of rod-shape nanostructures lead selenide via hydrothermal process, Superlattice Microstruct. 58 (2013) 20–30.

[5] M. Salavati-Niasari, M. Esmaeili-Zare, A. Sobhani, Synthesis and characterisation of cadmium selenide nanostructures by simple sonochemical method, Micro Nano Lett. 7 (2012) 831–834.

[6] O. Amiri, M. Salavati-Niasari, S. M. Hosseinpour-Mashkani, A. Rafiei, S. Bagheri, Cadmium selenide@ sulphide nanoparticle composites: facile precipitation preparation, characterization, and investigation of their photocatalyst activity, Mater. Sci. Semicond. Process 27 (2014) 261–266.

[7] M. Salavati-Niasari, A. Sobhani, Effect of nickel salt precursors on morphology, size, optical property and type of products (NiSe or Se) in hydrothermal method, Opt. Mater 35 (2013) 904–909.

[8] A. Sobhani, M. Salavati-Niasari, F. Davar. Shape control of nickel selenides synthesized by a simple hydrothermal reduction process, Polyhedron 31 (2012) 210–216.

[9] A. Sobhani A, M. Salavati-Niasari, Synthesis and characterization of a nickel selenide series via a hydrothermal process, Superlattice Microstruct 65 (2014) 79–90.

[10] F. Davar, M. Salavati-Niasari, Synthesis and characterization of spinel-type zinc aluminate nanoparticles by a modified sol-gel method using new precursor, J. Alloy Comp 509 (2011) 2487–2492.

[11] M. Salavati-Niasari, F. Mohandes, F. Davar, Preparation of PbO nanocrystals via decomposition of lead oxalate, Polyhedron 28 (2009) 2263–2267.

[12] A. Sobhani, F. Davar, M. Salavati-Niasari, Synthesis and characterization of hexagonal nano-sized nickel selenide by simple hydrothermal method assisted by CTAB, Appl. Surf. Sci. 257 (2011) 7982–7987.

[13] A. Sarkar, G. Sanyal, B. Chakraborty, B. Show, Phase engineering of molybdenum dichalcogenide to anion-tunable polyphasic quaternary chalcogenide (2H/1T/1T′)$MoS_xSe_yTe_z$($x + y + z = 2$) amplifies the growth of $H_2$ electrolytically, ACS Appl. Energy Mater. 6 (2023) 8017−8031.

[14] L. He, D. Zhou, Y. Lin, R. Ge, X. Hou, X. Sun, C. Zheng, Ultrarapid in situ synthesis of $Cu_2S$ nanosheet arrays on copper foam with room-temperature active iodine plasma for efficient and cost-effective oxygen evolution, ACS Catal. 8 (2018) 3859–3864.

[15] B. Liu, Y. F. Zhao, H. Q. Peng, Z. Y. Zhang, C. K. Sit, M. F. Yuen, T. R. Zhang, C. S. Lee, W. J. Zhang, Nickel Cobalt diselenide 3D mesoporous nanosheetnetworks supported on Ni foam: an all-pH highly efficient integrated electrocatalyst for hydrogen evolution, Adv. Mater. 29 (2017) 1606521 1–8.

[16] Y. Huang, X. Chong, C. Liu, Y. Liang, B. Zhang, Boosting hydrogen production by anodic oxidation of primary amines over a NiSe nanorod electrode, Angew. Chem. Int. Ed. 57 (2018) 13163–13166.

[17] W. Guo, Y. Chen, L. Wang, J. Xu, D. Zeng, D. L. Peng, Colloidal synthesis of $MoSe_2$ nanonetworks and nanoflowers with efficient electrocatalytic hydrogen-evolution activity, Electrochim. Acta 231 (2017) 69–76.

[18] Z. Yang, J. Y. Zhang, Z. Liu, Z. Li, L. Lv, X. Ao, Y. Tian, Y. Zhang, J. Jiang, C. Wang, “Cuju”-structured iron diselenide-derived oxide: a highly efficient electrocatalyst for water oxidation, ACS Appl. Mater. Interfaces 9 (2017) 40351–40359.

[19] Y. Du, G. Cheng, W. Luo, $NiSe_2/FeSe_2$ nanodendrites: a highly efficient electrocatalyst for oxygen evolution reaction, Catal. Sci. Tech. 7 (2017) 4604–4608.

[20] M. R. Gao, Z. Y. Lin, T. T. Zhuang, J. Jiang, Y. F. Xu, Y. R. Zheng, S. H. Yu, Mixed-solution synthesis of sea urchin-like NiSe nanofiber assemblies aseconomical Pt-free catalysts for electrochemical $H_2$ production, J. Mater. Chem. 22 (2012) 13662–13668.

[21] Z. Gao, J. Qi, M. Chen, W. Zhang, R. Cao, An electrodeposited NiSe for electrocatalytic hydrogen and oxygen evolution reactions in alkaline solution, Electrochim. Acta 224 (2017) 412–418.

[22] C. Tang, N. Cheng, Z. Pu, W. Xing, X. Sun, NiSe nanowire film supported on nickel foam: an efficient and stable 3D bifunctional electrode for full watersplitting, Angew. Chem. Int. Ed. 54 (2015) 9351–9355.

[23] F. Zhang, Y. Pei, Y. Ge, H. Chu, S. Craig, P. Dong, J. Cao, P.M. Ajayan, M. Ye,J. Shen, Controlled synthesis of eutectic $NiSe/Ni_3Se_2$ self-supported on Ni foam: an excellent bifunctional electrocatalyst for overall water splitting, Adv. Mater. Interfaces 5 (2018) 1701507 1–9.

[24] X. Wu, D. He, H. Zhang, H. Li, Z. Li, B. Yang, Z. Lin, L. Lei, X. Zhang, Ni0.85Se as anefficient non-noble bifunctional electrocatalyst for full water splitting, Int. J. Hydrogen Energy 41 (2016) 10688–10694.

[25] C. Cai, Y. Mi, S. Han, Q. Wang, W. Liu, X. Wu, Z. Zheng, X. Xia, L. Qiao, W. Zhou, X. Zu, Engineering ordered dendrite-like nickel selenide as electrocatalyst, Electrochim. Acta 295 (2019) 92–98.

[26] F. Wang, Y. Li, T.A. Shifa, K. Liu, F. Wang, Z. Wang, P. Xu, Q. Wang, J. He, Selenium-enriched nickel selenide nanosheets as a robust electrocatalyst for hydrogen generation, Angew. Chem. Int. Ed. 55 (2016) 6919–6924.

[27] J. Zhu, Y. Ni, Phase-controlled synthesis and the phase-dependent HER and OER performances of nickel selenide nanosheets prepared by an electrochemical deposition route, CrystEngComm 20 (2018) 3344–3352.

[28] R. Xu, R. Wu, Y. Shi, J. Zhang, B. Zhang, $Ni_3Se_2$ nanoforest/Ni foam as a hydrophilic, metallic, and self-supported bifunctional electrocatalyst for both $H_2$ and $O_2$ generations, Nanomater. Energy 24 (2016) 103–110.

[29] A. T. Swesi, J. Masud, M. Nath, Nickel selenide as a high-efficiency catalyst for oxygen evolution reaction, Energy Environ. Sci. 9 (2016) 1771–1782.

[30] M. S. Faber, M.A Lukowski, Q. Ding, N.S. Kaiser, S. Jin, Earth abundant metal pyrites ($FeS_2$, $CoS_2$, $NiS_2$, and their alloys) for highly efficient hydrogen evolution and polysulfide reduction electrocatalysis, J. Phys. Chem. C 118 (2014) 21347–21356.

[31] Q. Liu, J. Shi, J. Hu, A. M. Asiri, Y. Luo, X. Sun, $CoSe_2$ nanowires array as a 3D electrode for highly efficient electrochemical hydrogen evolution, ACS Appl. Mater. Interfaces 7 (2015) 3877–3881.

[32] C. Tsai, K. Chan, J. K. Nørskov, F. Abild-Pedersen, Rational design of $MoS_2$ catalysts: tuning the structure and activity via transition metal doping, Catal. Sci. Technol 5 (2015) 246–253.

[33] W. Lubitz, H. Ogata, O. Rudiger, E. Reijerse, Hydrogenases, Chem. Rev. 114 (2014) 4081–4148.

[34] T. Evans, D. M. Piper, S.C. Kim, S.S. Han, V. Bhat, K. H. Ohand, S. H. Lee, Ionic liquid enabled $FeS_2$ for high-energy-density lithium-ion batteries, Adv Mater 26 (2014) 7386–7392.

[35] K. Zhang, Y. Li, S. Deng, S. Shen, Y. Zhang, G. Pan, Q. Xiong, Q. Liu, X. Xia, X. Wang, J. Tu, Molybdenum selenide electrocatalysts for electrochemical hydrogen evolution reaction, ChemElectroChem 6 (2019) 3530–3548.

[36] J. Huang, H. Liu, B. Jin, M. Liu, Q. Zhang, L. Luo, S. Chu, S. Chu, R. Peng, Large-area snow-like $MoSe_2$ monolayers: synthesis, growth mechanism, and efficient electrocatalyst application, Nanotechnology 28 (2017) 275704 1–9.

[37] N. Masurkar, N. K. Thangavel, L. M. R. Arava, CVD-grown $MoSe_2$ nanoflowers with dual active sites for efficient electrochemical hydrogen evolution reaction, ACS Appl. Mater. Interfaces 10 (2018) 27771–27779.

[38] Y. Yin, Y. Zhang, T. Gao, T. Yao, X. Zhang, J. Han, X. Wang, Z. Zhang, P. Xu,P. Zhang, X. Cao, B. Song, S. Jin, Synergistic phase and disorder engineering in 1T-$MoSe_2$ nanosheets for enhanced hydrogen-evolution reaction, Adv. Mater. 29 (2017) 1700311 1–8.

[39] J. Zhang, T. Wang, P. Liu, Y. Liu, J. Ma, D. Gao, Enhanced catalytic activities of metal-phase-assisted 1T@2H-$MoSe_2$ nanosheets for hydrogen evolution, Electrochim Acta 217 (2016) 181–186.

[40] Y. Huang, F. Cui, Y. Zhao, J. Lian, J. Bao, T. Liu, H. Li, 3D hierarchical CMF/$MoSe_2$ composite foam as highly efficient electrocatalyst for hydrogen evolution, Electrochim. Acta 263 (2018) 94–101.

[41] E. Willinger, C. Massue, R. Schlögl, M. G. Willinger, Identifying key structural features of IrOx water splitting catalysts, J. Am. Chem. Soc. 139 (2017) 12093–12101.

[42] H. Over, Surface chemistry of ruthenium dioxide in heterogeneous catalysis and electrocatalysis: from fundamental to applied research, Chem. Rev. 112 (2012) 3356–3426.

[43] H. B. Gray, Powering the planet with solar fuel, Nat. Chem. 1 (2009) 7–10.

[44] L. Zhang, T. Wang, L. Sun, Y. Sun, T. Hu, K. Xu, F. Ma, Hydrothermal synthesis of 3D hierarchical $MoSe_2$/$NiSe_2$ composite nanowires on carbon fiber paper and

their enhanced electrocatalytic activity for the hydrogen evolution reaction, J. Mater. Chem. A 5 (2017) 19752–19759.

[45] L. Zhang, T. Wang, L. Sun, Y. Sun, T. Hu, K. Xu, F. Ma, Hydrothermal synthesis of 3D hierarchical $MoSe_2/NiSe_2$ composite nanowires on carbon fiber paper and their enhanced electrocatalytic activity for the hydrogen evolution reaction, J. Mater. Chem. 5 (2017) 19752–19759.

[46] X. Zhang, Y. Y. Zhang, Y. Zhang, W. J. Jiang, Q. H. Zhang, Y. G. Yang, L. Gu, J. S. Hu, L. J. Wan, Phase-Controlled synthesis of 1T-$MoSe_2$/NiSe heterostructure nanowire arrays via electronic injection for synergistically enhanced hydrogen evolution, Small 3 (2019) 1800317 1–6.

[47] X. Zhou, Y. Liu, H. Ju, B. Pan, J. Zhu, T. Ding, C. Wang, Q. Yang, Design and epitaxial growth of $MoSe_{2e}$NiSe vertical hetero nanostructures with electronic modulation for enhanced hydrogen evolution reaction, Chem. Mater. 28 (2016) 1838–1846.

[48] C. Wang, P. Zhang, J. Lei, W. Dong, J. Wang, Integrated 3D $MoSe_2$@$Ni_{0.85}$ se nanowire network with synergistic cooperation as highly efficient electrocatalysts for hydrogen evolution reaction in alkaline medium, Electrochim. Acta 246 (2017) 712–719.

[49] K. Premnath, P. Arunachalam, M. S. Amer, J. Madhavan, A. M. Al-Mayouf, Hydrothermally synthesized nickel molybdenum selenide composites as cost effective and efficient trifunctional electrocatalysts for water splitting reactions, Int. J. Hydrogen Energy 44 (2019) 22796–22805.

[50] C. Liu, K. Wang, X. Zheng, X. Liu, Q. Liang, Z. Chen, Rational design of $MoSe_2$-NiSe@carbon hetero nanostructures for efficient electrocatalytic hydrogen evolution in both acidic and alkaline media, Carbon 139 (2018) 1–9.

[51] H. Yang, Y. Huang, W. Y. Teoh, L. Jiang, W. Chen, L. Zhang, J. Yan, Molybdenum Selenide nanosheets surrounding nickel selenides submicro islands

on nickel foam as high-performance bifunctional electrocatalysts for water splitting, Electrochimica Acta 349 (2020) 136336 1–11.

[52] A. Ghosh , M. Mondal , R. N. Manna , A. Bhaumik , Targeted synthesis of a metal-free thiadiazolate based nitrogen and sulfur rich porous organic polymer for an unprecedented hydrogen evolution in the electrochemical water splitting, J. of Colloid and Interface Science 658 (2024) 415–424.

# NOTABLE ACHIEVEMENTS AND CONCLUSIONS

The thesis deals with the synthesis of electro-catalytically active nanoparticles by using various protocols in absence of any capping agent.Synthesized nanoparticles are characterized by spectroscopic analysis FTIR, microscopic (FESEM, HRTEM), XRD, EDS and XPS analysis.The electrocatalytic studies are done in these work.The CV,CA, impedence are carried out during the process.The electrocatalytic active surface area is calculated for the measurement of the surface area of the electrocatalysts.The catalytic proficiency of the synthesized nanomaterials are evaluated with respect to water splitting reaction of metal and metal-oxide nanoparticles.The experimental findings of the electrocatalytic activity of the pure metals like Ni, Cu, Mo etc are combined with sulphide and selenide molecules to form the bimetallic nanoparticles.The significance of water splitting is promising technology that confirmed water is split to generate clean pure hydrogen fuel.Hence the green fuels is to be useful for different resolutions.

## Future aspects:

Previously noted, the division of water splits into hydrogen and oxygen throughout solar energy is thoroughly investigated challenge, pivotal for addressing future energy demands. Photocatalysts activated by visible light offer significant benefits, as they circumvent the need for sophisticated energy conversion technologies typically associated with non-renewable sources like solar or wind power. Heterogeneous photocatalysis not only yields hydrogen but also produces oxygen—avaluable byproduct. However, this process faces issues such as catalyst degradation due to oxide formation during the oxygen evolution reaction. Additionally, the existing photocatalysts exhibit a low turnover frequency, warranting further exploration. The development of durable photocatalysts that can be effortlessly separated from the reaction mix and reused presents an expansive research opportunity. Investigating catalysts composed of novel or readily available transition metals remains an intriguing avenue for future study. Adjusting existing transition metal catalysts with diverse ligands opens up vast possibilities for engineering more efficient and stable catalysts, potentially surpassing current limitations. Modifying the metal composition in heterogeneous catalysts also presents the gifted opportunity to increase the performance of earlier reported electrocatalysts. The escalating global energy demand compels us to innovate superior and cleaner energy solutions, and photocatalytic water splitting stands out as an exceptionally promising direction.

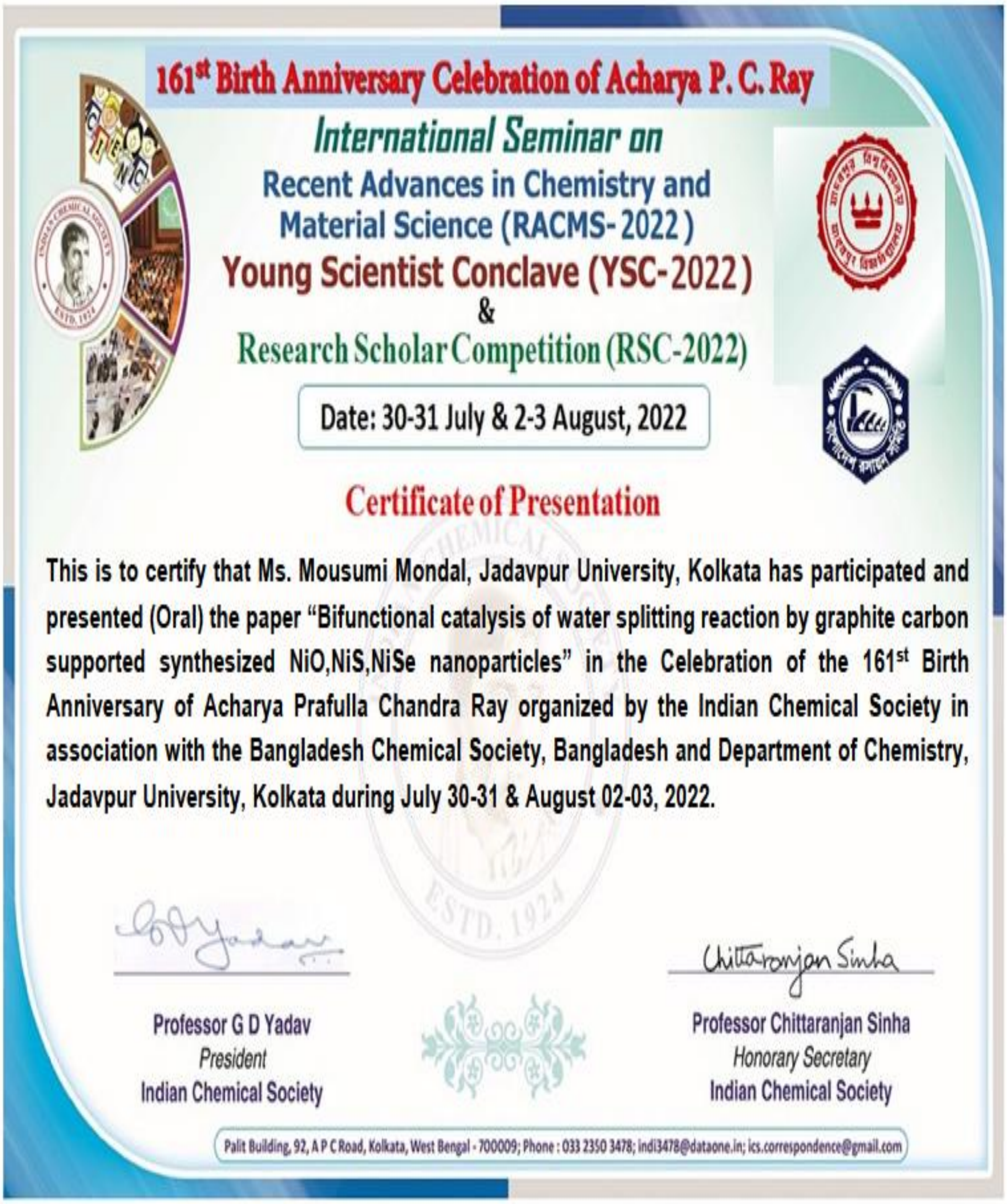

161st Birth Anniversary Celebration of Acharya P. C. Ray

International Seminar on
Recent Advances in Chemistry and
Material Science (RACMS-2022)
Young Scientist Conclave (YSC-2022)
&
Research Scholar Competition (RSC-2022)

Date: 30-31 July & 2-3 August, 2022

## Certificate of Presentation

**This is to certify that Ms. Mousumi Mondal, Jadavpur University, Kolkata has participated and presented (Oral) the paper "Bifunctional catalysis of water splitting reaction by graphite carbon supported synthesized NiO,NiS,NiSe nanoparticles" in the Celebration of the 161st Birth Anniversary of Acharya Prafulla Chandra Ray organized by the Indian Chemical Society in association with the Bangladesh Chemical Society, Bangladesh and Department of Chemistry, Jadavpur University, Kolkata during July 30-31 & August 02-03, 2022.**

Chittaranjan Sinha

Professor G D Yadav
*President*
Indian Chemical Society

Professor Chittaranjan Sinha
*Honorary Secretary*
Indian Chemical Society

Palit Building, 92, A P C Road, Kolkata, West Bengal - 700009; Phone : 033 2350 3478; indi3478@dataone.in; ics.correspondence@gmail.com

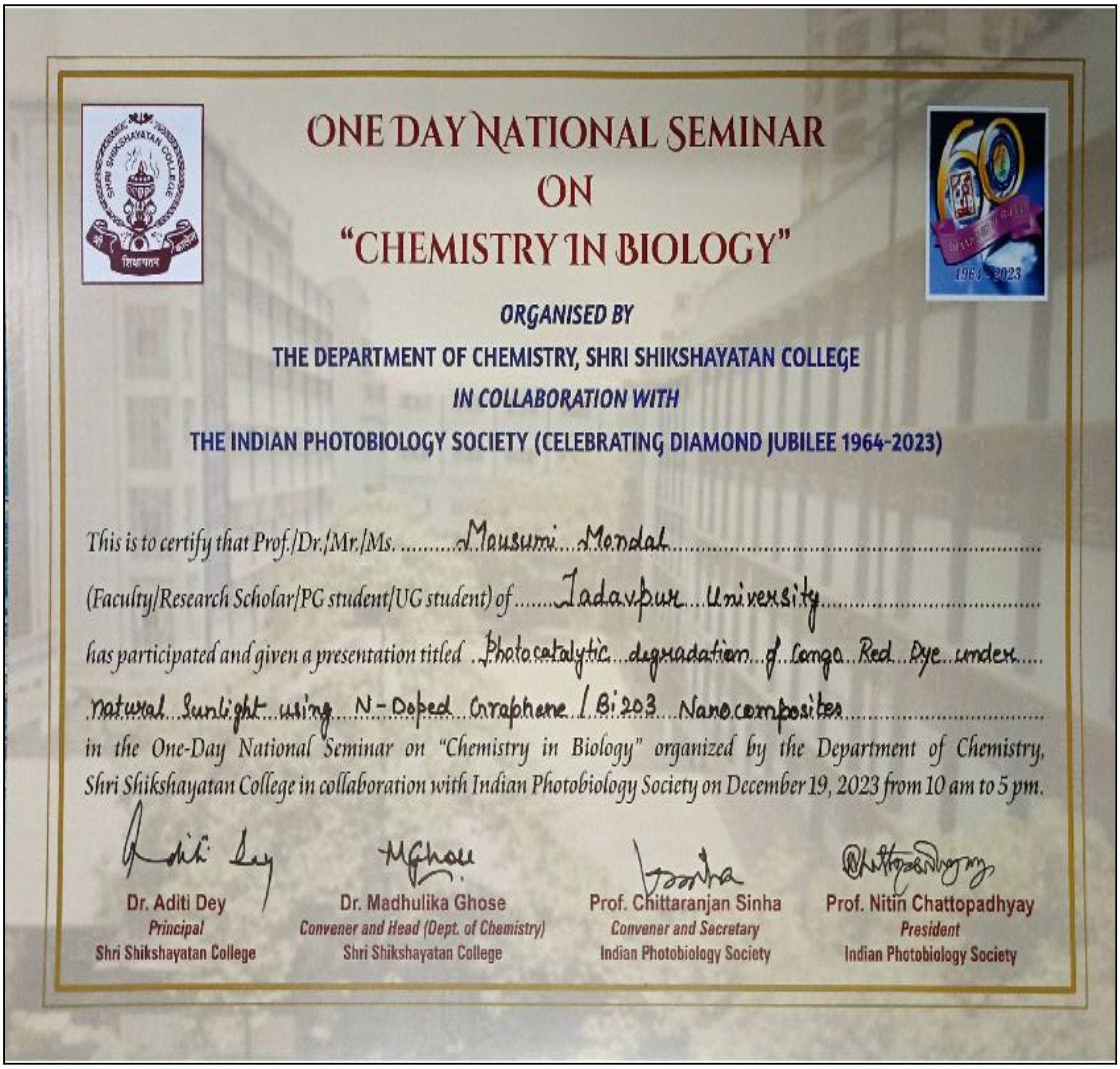

# ONE DAY NATIONAL SEMINAR
# ON
# "CHEMISTRY IN BIOLOGY"

***ORGANISED BY***

**THE DEPARTMENT OF CHEMISTRY, SHRI SHIKSHAYATAN COLLEGE**

***IN COLLABORATION WITH***

**THE INDIAN PHOTOBIOLOGY SOCIETY (CELEBRATING DIAMOND JUBILEE 1964-2023)**

*This is to certify that Prof./Dr./Mr./Ms.* Mousumi Mondal

*(Faculty/Research Scholar/PG student/UG student) of* Jadavpur University

*has participated and given a presentation titled* Photocatalytic degradation of Congo Red Dye under natural Sunlight using N-Doped Graphene / $Bi_2O_3$ Nanocomposites

*in the One-Day National Seminar on "Chemistry in Biology" organized by the Department of Chemistry, Shri Shikshayatan College in collaboration with Indian Photobiology Society on December 19, 2023 from 10 am to 5 pm.*

Aditi Dey
**Dr. Aditi Dey**
*Principal*
Shri Shikshayatan College

MGhose
**Dr. Madhulika Ghose**
*Convener and Head (Dept. of Chemistry)*
Shri Shikshayatan College

**Prof. Chittaranjan Sinha**
*Convener and Secretary*
Indian Photobiology Society

**Prof. Nitin Chattopadhyay**
*President*
Indian Photobiology Society

Energy Nexus 14 (2024) 100289

Contents lists available at ScienceDirect

Energy Nexus

journal homepage: www.elsevier.com/locate/nexus

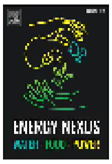

# Superiority of CuSe as a non-nobel electrocatalyst among copper chalcogens for overall water splitting reactions

Mousumi Mondal[a], Sabyasachi Maity[b], Anirban Ghosh[c], Sujit Kumar Ghosh[a], Swapan Kumar Bhattacharya[a,*]

[a] *Physical Chemistry Section, Department of Chemistry, Jadavpur University, Jadavpur, Kolkata 700032, India*
[b] *Drilling Fluids Services, 11 High, Oil and Natural Gas Commission, Mumbai- 400017, India*
[c] *School of Materials Sciences, Indian Association for the Cultivation of Science, Jadavpur, Kolkata-700032, India*

ARTICLE INFO

*Keywords:*
Copper oxide
Copper sulfide
Copper selenide
Water splitting reaction

ABSTRACT

Among the transition metals copper is one of the cheapest earth- abandoned elements which can enhance electrocatalytic activity. The Cu-based catalysts are superior for catalytic performance and stability in alkaline media for oxygen evolution reaction (OER) and exhibit high activity in acidic media for hydrogen evolution reaction (HER).Synthesized CuSe nanoparticle is found as the most efficient bifunctional electrocatalyst among the synthesized Cu chalcogenides for water splitting reaction. Electrocatalytic performance for water oxidation was investigated in alkaline solution1(M) KOH for OER and 0.5 (M) $H_2SO_4$ for HER. To achieve 10 mA/cm$^2$, it was observed an over potential (mV) of 343 for OER and 126 for HER, which are much smaller than these of CuS (385,320) and CuO (410, 345) studied. In this article, we have elucidated some essential criteria need to be specified to evaluate the water splitting performance including onset potential, overpotential, Tafel slope, turnover frequency (TOF), and stability of the copper chalcogenide nanoparticles.

## Introduction

One of the serious upsurging global problems is the energy crisis that is world facing today. Energy demand is skyrocketing in the last few decades. Sources of non-renewable energy are depleting fast and the world is looking for new handy non-traditional energy sources. Splitting of water into oxygen and hydrogen is one of the best ways to overcome the current energy crisis and reduce air pollution simultaneously. For natural photosynthesis, which converts light energy into chemical energy, this is crucial. Cu is essential for the water splitting process in the biological systems . Some of the ongoing research efforts demonstrate an eagerness to comprehend how Cu contributes to biological water splitting. In the effort to create artificial photosynthetic systems employing sustainable and noble metal-free catalysts, highly crystalline CuSe has been deployed in alkaline media as active electrodes for overall water splitting (OWS) [1].

The low abundance of these precious elements limits their wide practical application. Copper is a more abundant and cheaper metal among the transition metal elements (such as cobalt, nickel, iridium and manganese). Recently, some copper-based compounds have been researched as OER catalysts, such as oxides, hydroxides, phosphides, nitrides and selenides [2–4]. Copper selenide is an important member of first row transition metal chalcogenides [5–7], can exist in a wide range of compositions, both stoichiometric (CuSe, $Cu_2Se$, $CuSe_2$, $Cu_3Se_2$, $Cu_7Se_4$) and non-stoichiometric ($Cu_{2-x}Se$) [8,9]. Although, they are rarely formed as minerals in nature, synthetic selenides represent a remarkable group of compounds with great potential in various scientific fields (such as photovoltaics, thermoelectric, or optoelectronics) due to their extraordinary electric and thermal properties. The state-of-the-art electrocatalysts to perform water splitting (WS) mainly rely on the noble-metal-based materials ($RuO_2$ and $IrO_2$ for OER, and Pt for HER). But their high cost have prevented their practical application [10,11]. Conversely, recent studies infer that higher OER or HER catalytic activity could be achieved by a subtle choice of Earth-abundant transition-metal (TM) based catalysts, particularly the first-row TMs [12–17]. However, only a few of them have been shown to mediate efficient bifunctionality for water-splitting reactions [18,19]. The metal organic framework (MOF) can act as an efficient bifunctional electrocatalyst for HER and OER [20].

Electrochemical water splitting continues to be a frontier field of

---

[*] Corresponding author.
*E-mail address:* skbhatt7@yahoo.co.in (S.K. Bhattacharya).

https://doi.org/10.1016/j.nexus.2024.100289

study. In this respect, it is worth to point out that many transition metal nitrides, phosphides, chalcogenides, MOF, polymers and their composites, have been established to realize the comparable efficacy to substitute the state-of-the-art catalyst, Pt. In comparison, very few works have been done with $Cu^{II}$ chalcogenides as electrocatalysts [21]. In search of low overpotential material, we concentrated in this study on $Cu^{II}$ chalcogenides which may help understanding the chalcogen group, since some $Cu^{I}$ and $Cu^{III}$ compounds like $Cu_2Se$, $Cu_3N$, $Cu_3P$, etc. are already found in the literature [22–24].

## Experimental section

### *Chemicals*

Copper nitrate ($Cu(NO_3)_2$ (99.99 % Merck), sodium sulfide ($Na_2S$) (99.99 % Merck), sodium hydroxide (NaOH) (99.9 %, Sigma- Aldrich), sodium selenite ($Na_2SeO_3$) (99.99 % Merck), hydrazine hydrate ($N_2H_4$) (99 %, Sigma-Aldrich) are used without further purification. The deionized water is used throughout the study. Any other solvents are purchased from Sigma-Aldrich and used without further purification.

### *Synthesis of copper oxide, sulfide and selenide nanoparticles*

An aliquot of 2(M) copper nitrate and 1(M) sodium selenite ($Na_2SeO_3$) were mixed thoroughly and equivalent hydrazine hydrate was added in the solution. The mixture was put into the autoclave and heated for 24 h at 180 °C. Then, the mixture was cooled to room temperature. The solution was centrifuged and the product was heated at 60° C in a hot air oven. Copper nitrate and sodium sulfide ($Na_2S$) was used for synthesized copper sulfide nanoparticles. Similarly, copper nitrate and sodium hydroxide was used for synthesis of copper oxide nanoparticles in the same hydrothermal procedure.

### *Structure characterisation*

The crystal structure of synthesized nanoparticles was investigated by X-ray diffraction (XRD) study was performed using a (Bruker D8 Advance) diffractometer equipped with a CuKα radiation source ($l$ = 1.5418 Å generated at 40 kV and 40 mA.). The field emission scanning electron spectroscopy (FESEM) and energy dispersion X-ray spectroscopy (EDX) with SEI INSPECT F 50 FE-SEM was characterization technologies and composition. The chemical valence was characterized by X-ray photoelectron spectroscopy.

### *Electrochemical characterisation*

The electrocatalytic responses of catalyst were demonstrated using cyclic voltammetry (CV) and fixed potential chronoamperometric (CA) studies. The electrochemical measurements were conducted using a computer aided potentiostat/galvanostat of AUTOLAB PG STAT 12 (Eco Chemic, Netherlands). The reference electrode used in all electrochemical measurements was Ag/AgCl(KCl saturated).In all of the electrochemical studies a large pt-foil (1 cm × 1 cm) was used as counter electrode. The working electrode was a planar graphite carbon electrode having area12 × $10^{-6}$ $m^2$. The working electrode was prepared by sonication of 5 mg of catalyst dust in 1 mL ethanol for 30 mins to form an almost homogeneous mixture. 10 μL of the dispersion is then drop cast on the carbon electrode followed by drying at room temperature (25 °C). Then, 5 μL Nafion solution (1 mass %) was cast on the electrode followed by drying again cyclic voltammogram of each electrode measured in 1 M KOH solution at the scan rate of 50 mV/s for OER and 0.5 M $H_2SO_4$ solution for HER. The measurement potentials were converted to the reversible hydrogen electrode (RHE) by using Nernst equation,

$$E_{RHE} = E_{Ag/AgCl} + (0.059pH + 0.197)\,V \tag{1}$$

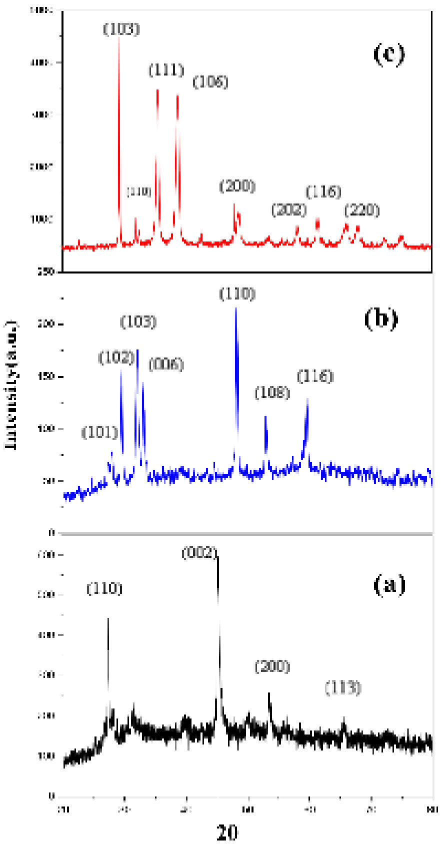

Fig. 1. XRD plots of (a) CuO, (b) CuS and (c) CuSe nanoparticles. The 2θ values along the x-axis have been expressed in degrees.

The value of overpotential (η) was calculated by the equation,

$$\eta = E_{RHE} - 1.23V \tag{2}$$

The electrochemical kinetics of the catalysts towards water splitting reaction the overpotential η with was evoluted by Tafel equation,

$$\eta = b\log j + a \tag{3}$$

where j is the current density, b is Tafel slope and a is constant.

The electrochemical active surface area (ECSA) was calculated from double layer capacitane, $C_{dl}$ by cyclic voltammograms measured as various scan rates 10, 20,40,50,80,100 mV $s^{-1}$ in the potential range in the non-Faradic region. The $C_{dl}$ was evoluted from the average value of cathodic and anodic slopes. The turn over frequency was calculated from CV and CA plots.

## Results and discussion

### *XRD analysis*

Powder X-Ray Diffractometer (XRD) was used to analyze the crystal structure of synthesized sample. Powder X-Ray Diffraction (PXRD)

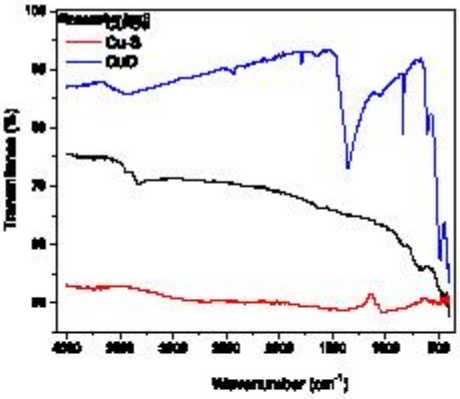

Fig. 2. FTIR spectroscopy of CuO, CuS and CuSe nanoparticles.

experiment of the prepared powdered sample was accomplished using a (Bruker D8 Advance) diffractometer along with a CuK$_\alpha$ radiation source (λ–1.5418 Å generated at 40 kV and 40 mA) Cupper selenide nanoparticles contain 27.31 (103), 31.23(110), 45.06 (111), 46.95(106), 50.14(200),53.35 (202),56.12(116), 72.84(220) planes. The mean size of the nanoparticle was designed from the peak width at half maximum is 18.4 nm by the Debye Scherrer equation. Copper sulfide nanoparticles contains 28.1(101), 29.01(102), 31.50(103), 32.01(006),49.01 (110),53.1(108),60.1(116) planes JCPDS No.06–0464 and half maxima is 17.23 nm. Copper oxide nanoparticles contains 29.1 (110), 45.5(002), 55.5(200), 68.9(113) planes JCPDS No.89-2531 and half maxima is 16.10 nm.

### *FTIR analysis*

CuO nanoparticles bands at around 601 cm$^{-1}$ and 487 cm$^{-1}$ for vibrations confirm the formation of Cu-O bonds. The sharp peak observed at 601 cm$^{-1}$ characteristics of Cu-O bond formation. A broad peak at 3433 cm$^{-1}$ for O—H stretching arises due to moisture content [25]. For CuS nanoparticles, 3435 cm$^{-1}$ vibration mode of water OH group indicating the presence of small amount of water absorbed on the particle 1631 cm-1 for OH bending [26]. CuSe two major peaks were observed at 1609 cm$^{-1}$ and 3471 cm$^{-1}$. The peak at 1609 cm$^{-1}$ may be attributed to the presence of Cu$^{2+}$ ion in the present system. The peak at around 3471 cm$^{-1}$ may corresponds to N—H stretching vibration band which can be attributed to the interaction of $N_2H_4$ with copper ions [27].

### *FESEM and TEM analysis*

The FE-SEM, and TEM observation of the morphology of CuSe nanoparticles is shown in Fig. 3. Here, we are obtaining nanoscale images and chemical data using HR-transmission electron microscopes (S/TEM) in conjunction with energy dispersive X-ray spectroscopy (EDX), providing crucial insights into the configuration and potential functions of deployed Cu-catalyst. The contrast of TEM image arises from the interference in the image plane of the electron wave itself.

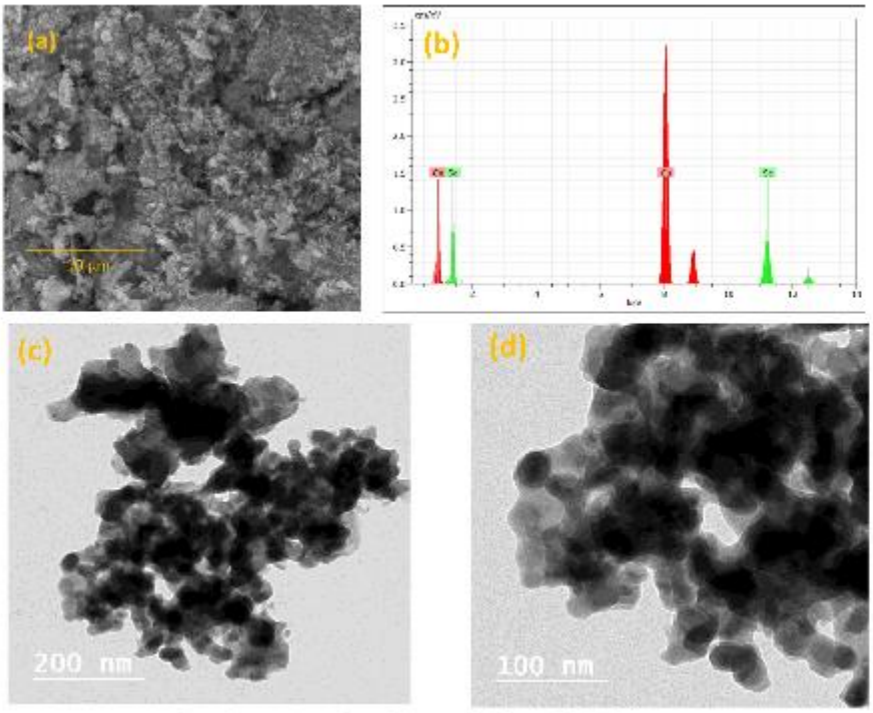

Fig. 3. a) FESEM image of CuSe; (b) EDX graph of CuSe and (c & d) TEM images.

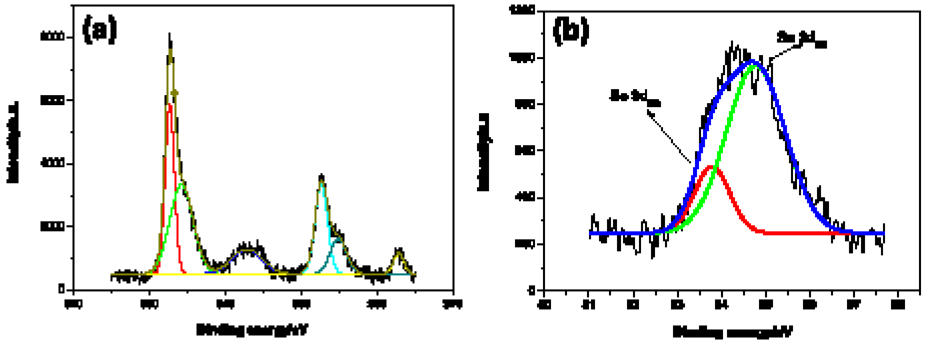

Fig. 4. XPS analysis of CuSe nanoparticles.

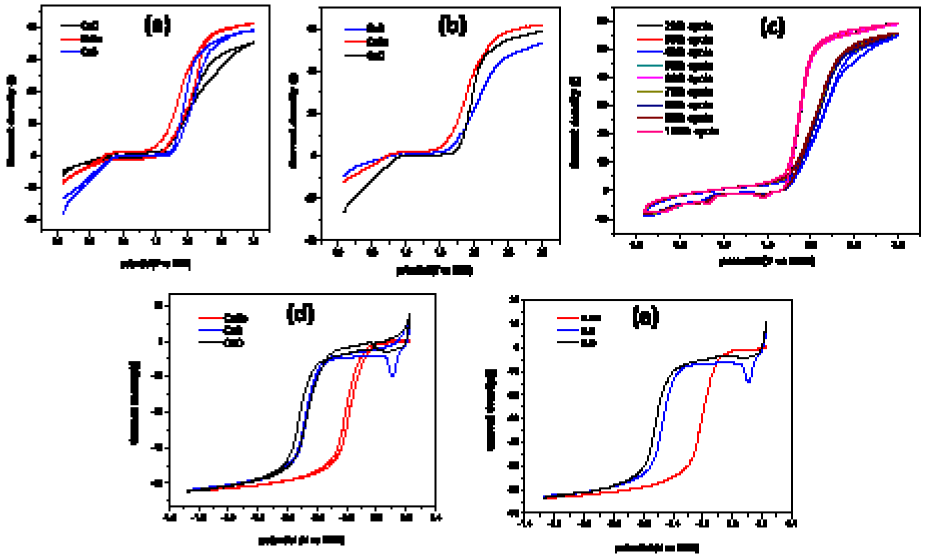

Fig. 5. Cyclic voltammogram and LSV diagram in 1 (M) KOH solution for OER (a & b),100th cycle© and 0.5 (M) $H_2SO_4$ solution for HER (d & e).

*XPS analysis*

In this study, we also employed XPS to analyze the surface chemistry of our catalyst samples. The purpose of this experiment was to determine the elemental composition and chemical state of the atoms within our sample. Using an x-ray beam, the surface atoms of our solid copper chalcogen catalysts samples being excited and measured the kinetic energy and the number of electrons that escaped from the top 0 to 10 nanometers of the sample. On the generated spectra, the position of a peak on the x-axis indicated the elemental and chemical composition while the y-axis recorded the intensity of surface material how much of a particular element can be found at the surface. Peaks from the XPS spectra gave relative number of electrons with a specific binding energy. Our results showed that our sample contained. In the high-resolution XPS, the Cu2p envelope consisted of two peaks corresponding to Cu2p3/2 and Cu2p1/2 at the binding energies of 932.1 eV and 952.2 eV, respectively. The Se3d envelope recorded with the powder sample showed an overlapped spin-orbit component with two maxima for 3d5/2 and 3d3/2 peaks at 53.8 and 54.5 eV ($D = 0.7$ eV). These energy values (after deconvolution) are consistent with the presence of Se II, as shown for reported CuSe materials. Moreover, a weak loss feature at 56.1 eV and a weak peak corresponding to Se IV arising from surface passivation at 58.3 eV, as observed in other metal selenides.

*Electrochemical results*

The electrochemical performances are studied in 1.0 M KOH and 0.5 M $H_2SO_4$ (Fig. 5) solutions at the scan rate of 50 mV $s^{-1}$ for OER and HER respectively. These exhibit shoulders before oxygen evolution and corresponding small peaks in the reverse scan plausibly due to Cu/$Cu^{+2}$ and reverse transition respectively. The oxidation state of chalcogens seems to be much more stable in the scan range. The onset potential of CuSe, CuS and CuO catalysts for OER follows the order: CuSe< CuS< CuO as presented in the Table 1, indicating the reverse order of catalytic

**Table 1**
Cyclic voltammetry and chronoamperometry data of oxygen and hydrogen evolution reactions.

| Compound | Turnover Frequency($hr^{-1}$) | | | |
|---|---|---|---|---|
| | CV | | CA | |
| | OER | HER | OER | HER |
| CuO | 0.76 | 0.59 | 0.51 | 0.49 |
| CuS | 0.33 | 1.81 | 0.54 | 0.77 |
| CuSe | 1.4 | 7.18 | 1.20 | 5.47 |

capability of them near equilibrium region. The over potential (mV) at the bench mark current density, 10 mA/cm$^2$ are 343, 385 and 410 for these synthesized materials respectively revealing superiority of CuSe over others in catalytic property. During activation process of the CuSe based electrode by repeated cyclic voltammetry, it is found that the overpotential decreases with increase of catalytic cycle. In the first 100 cycles the overpotential decreases by about 120 mV. It is expected that there might be some compositional/morphological change of the catalyst at least at the surface of the electrode which is responsible for such positive effect.

The reason behind such trend/ change might be due to the formation of a thin layer of $Cu(OH)_2$which acts as electro post catalyst in alkali as suggested elsewhere [1]. The $Cu(OH)_2$ layer is thin over CuSe, since, since the latter is enough stable and found in nature as selenide materials [28,29]. The trend of greater catalytic capability of CuSe over CuS and CuO is also found at much higher current density. The order of overpotential @10 mAcm$^{-2}$ is found to be CuSe<CuS<CuO,(343,385,410 mV) but that for 50 mA cm$^{-2}$ is CuSe<CuO<CuS,(768,823,943 mV) implying that CuO is a better catalyst over CuS at higher potentials/ current density. This indicates a large change of catalytic activity of CuO based electrode at higher potential in comparison to CuS, which might be due to the greater formation of $Cu(OH)_2$ or CuOOH on the surface of CuO based electrode at higher potential [20,21].

To assess the constancy in catalytic activity and long term stability of catalyst, chronoamperometric (CA) measurement were carried out at a potential of −0.4 V for 1200 second in a solution of 0.5 (M) $H_2SO_4$and 0.8 V in 1 (M) KOH.

Turn over frequency (TOF) is an integral property of an ideal catalyst. Turn over frequency for both HER and OER is calculated by assuming 100 % faradic efficiency for catalyst as,

$$\mathrm{TOF} = I/nFm = JA/nFm\ldots\ldots \qquad (V)$$

where $I$ = current (A), $J$ = average current density (A cm$^{-2}$), $A$ = geometrical surface area = 0.12 cm$^2$, $n$ = no of electron transferred = 4 (for OER)/ 2 (for HER), $F$ = 96,485 C, $m$ = moles of catalyst per active site [30–31].

The onset potential of hydrogen evolution reaction (HER) on CuSe, CuS and CuO are 108,136,142 mV vs RHE. The overpotentials at current density 10 mA/cm$^2$for the reaction are 126, 320 and 345 mV respectively. The electronegativity of Se is greater than Cu.Thus Cu is slightly + ve and Se is –ve in CuSe molecule. So for OER Cu center acts as a $OH^-$ adsorption center to initiate the reaction. CuSe $+OH^- \rightarrow HO—CuSe + e$ (M).The intermediate HO….CuSe subsequently causes OER. On the other hand, Se acts as a center for adsorption of $H^+$ accordingly to the reaction CuSe + $H_2O \rightarrow$CuSe….$H$ +$OH^-$. The intermediate CuSe…..H subsequently undergoes HER. These are obtained from the detail experimental kinetic measurements and theoretical studies on the energy and stability of the involved intermediates of the reactions. According to periodic table down the group the size of the elements increased so the bond length is increased and bond energy is decreased. Cu…Se is thermally broken easily than CuS and CuO; so CuSe shows better water splitting reaction (bond lengths of CuSe, CuS and CuO are 2.51,2.24,1.98 Å). The reason behind such change might be due to the formation of a thin layer of $Cu(OH)_2$ (electro part catalysis) is alkali as suggested elsewhere. The formation of $Cu(OH)_2$ layer is thin over CuSe since the latter is enough stable and found in nature at higher potential. This indicates a large change in catalytic activity of CuO based electrode in comparison to CuS which might be due to the formation of $Cu(OH)_2$ or CuOOH at higher potential [32,33]. Table 3 compares the efficacy of our synthesized compounds with some others used as electrocatalysts in reference to HER and OER. It is found that the study on $Cu^{II}$ compounds is few and the overpotetial and tafel slopes using the synthesized $Cu^{II}$ chalcogenides are comparable with these of others.

OER Mechanism

$$CuX + OH^- \rightarrow CuXOH + e^- \ldots\ldots\ldots \qquad (R1)$$

$$CuXOH + OH^- \rightarrow CuXO + H_2O + e^- \ldots\ldots\ldots \qquad (R2)$$

$$CuXO + CuXO \rightarrow 2CuX + O_2 \ldots\ldots\ldots\ldots\ldots \qquad (R3)$$

$$2CuCOH + 4OH^- \rightarrow 2CuOOH + 2H_2X + O_2 \ldots\ldots \qquad (R4)$$

$$CuXOH + CuOOH \rightarrow CuX + O_2 + H_2O \ldots\ldots\ldots\ldots \qquad (R5)$$

HER possess through three distinct route by $2e^-$ transfer mechanism in acidic medium which can be expressed as,

Volmer step:

$$H_3O^+ + {}^* + e^- \rightarrow H^* + H_2O \ldots\ldots\ldots \qquad (R'1)$$

Heyrovsky step:

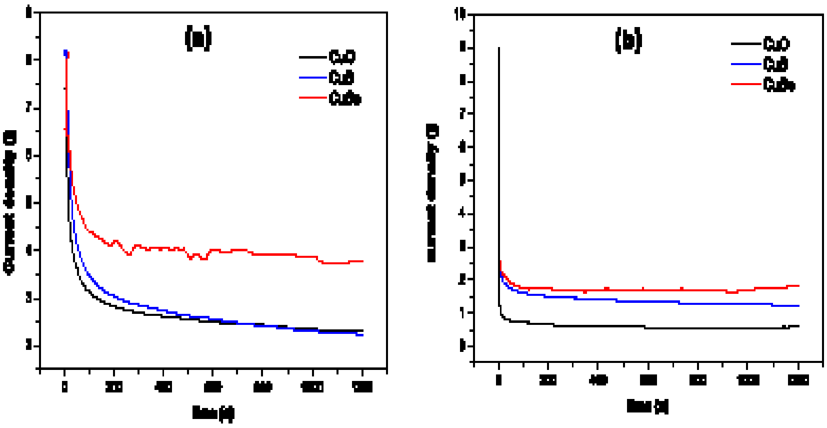

Fig. 6. Chronoamperometry plot of 1.0 (M) KOH and 0.5 (M) $H_2SO_4$ solution.

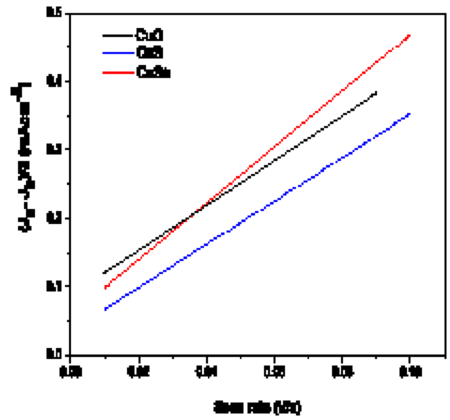

Fig. 7. $C_{dl}$ plots CuO, CuS and CuSe electrocatalysts.

$H_3O^+ + H^* + e^- \rightarrow H_2 + H_2O + {}^*$ ....... (R'2)

Tafel step:

$H^* + H^* \rightarrow H_2 + 2^*$ ........ (R'3)

Electrochemical active surface area

The $C_{dl}$ values for CuSe, CuS and CuO electrocatalysts are 4.12, 2.27 and 2.18 $mFcm^{-2}$, respectively. From the Randles equivalence circuit model, *Rs*, series resistance, is calculated at the intersection of the real axis (*X*-axis) in the high-frequency region. *Rs* represents the ohmic resistance andionic resistance at the electrode and electrolyte interface. However, the charge transfer resistance (*R*ct) was found fromthe lower-frequency region of the Nyquist plot [34].

To study the reaction kinetics electrochemical impedence spectroscopy (EIS) measured

OER involves a four electron transfer process, higher potentials than the theoretical potential (> 1.23 V vs RHE) are required to surmount the overall energy barrier in each electron transfer step [3,35]. Overpotential (η) is one of the most crucial parameters that affect the OER/HER performance of the electrocatalysts which is usually measured at a specific current density of 10 mA/cm$^2$.

$\eta = bXlog(j) + a$

Low overpotential shines as advantages of good OER electrocatalysts. Because the high overpotential (η) lead to more energy consumption reducing energy conversion efficiencies. It should be noted that it is highly suggested that Here in the following Table 1 the loading mass and turnover frequency are reported while comparing the OER/HER activities of electrocatalysts as overpotential is strongly influenced by the loading mass of electrocatalysts.

Tafel slope (η) is another crucial parameter that reflects the kinetics of OER and HER. According to the Tafel equation, the Tafel slope is the rate of augmentation of overpotential (η) in relation to current density (j). A diminished Tafel slope implies a rapid escalation in the current density with the increment of overpotential, which signifies swift OER and HER kinetics of the electrocatalysts. The Tafel slopes (mVdec$^{-1}$) found for OER are 166,131,94 for CuO, CuS and CuSe respectively. The experimental Tafel slopes (mV dec$^{-1}$) for HER on CuO, CuS and CuSe are 124,110,83.9 respectively. The Tafel slopes for HER indicate that the Tafel-Heyrovsky mechanism is followed for all the materials.

## Conclusions

Electrocatalytic water splitting is an emerging and challenging area of chemistry that has received limited attention until the last two decades. To explore the potential of powdered catalysts for water splitting reaction, especially those based on earth abundant metals, we synthesized Cu based nanoparticles via a hydrothermal approach and evaluated their electrocatalytic performance for both oxygen evolution reaction (OER) and hydrogen evolution reaction (HER). Powdered catalysts offer advantages for large-scale application of water splitting due to their high turnover numbers and low overpotential. We also investigated other copper chalcogenides such as copper oxide and copper sulphides (which were prepared under similar conditions by the same method) and demonstrated that CuSe exhibited superior catalytic activity for both OER and HER compared to the other copper chalcogenides. This indicates that the activity and electronic structure of electrocatalysts for water electrolysis can be modulated by varying the chalcogen element in the same group. The present study provides a new opportunity to design and fabricate novel catalysts from noble-metal-free and earth-abundant sources, and to disseminate valuable

**Table 2**
Electrochemical impedance spectroscopy data.

| Electrocatalyst | Electrolyte | $R_s$ (Ω) | $R_{ct}$ (Ω) | $C_{dl}$ (μF) |
|---|---|---|---|---|
| CuO | 1 (M) KOH | 71.82 | 2198 | 4.197 |
| | 0.5 (M) $H_2SO_4$ | 56.78 | 2325 | 5.98 |
| CuS | 1 (M) KOH | 44.04 | 1157 | 1.83 |
| | 0.5 (M) $H_2SO_4$ | 53.9 | 776.3 | 1.33 |
| CuSe | 1 (M) KOH | 42 | 1137 | 1.56 |
| | 0.5 (M) $H_2SO_4$ | 52.08 | 285 | 1.26 |

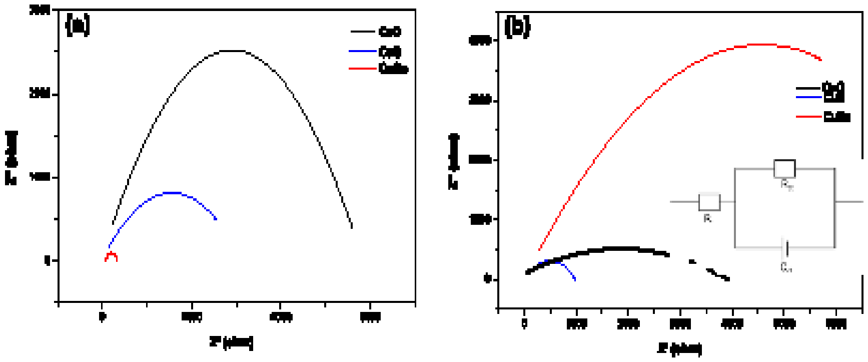

Fig. 8. Nyquist plot of (a) OER in KOH medium and (b) HER in $H_2SO_4$ medium.

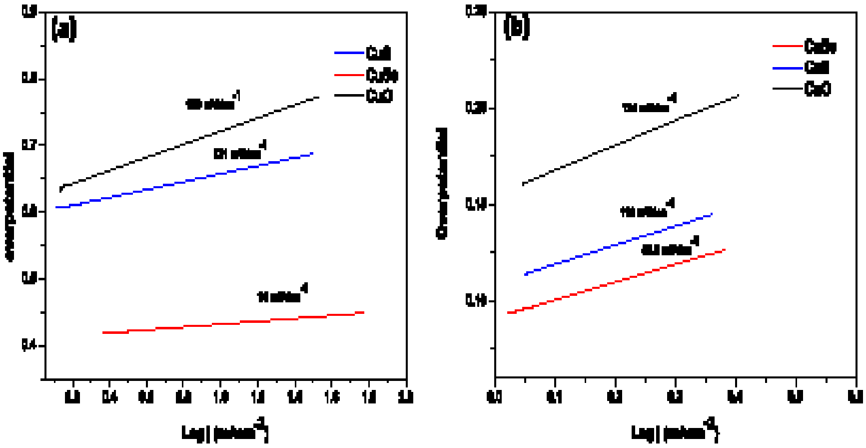

Fig. 9. (a) OER and (b) HER Tafel plots for CuO, CuS and CuSe nanoparticles.

**Table 3**
Comparative account of electrochemical performance of copper chalcogenides with similar materials.

| Electrocatalyst | Electrolyte | Reaction | Overpotential (η) /@ 10 mA/cm$^2$ (mV) | Tafel slope / (mV/dec) | Reference |
|---|---|---|---|---|---|
| CuO | 1 (M) KOH | OER | 410 | 188 | Present work |
| | 0.5 (M) $H_2SO_4$ | HER | 345 | 124 | Present work |
| CuS | 1 (M) KOH | OER | 385 | 131 | Present work |
| | 0.5 (M) $H_2SO_4$ | HER | 320 | 110 | Present work |
| CuSe | 1 (M) KOH | OER | 343 | 94 | Present work |
| | 0.5 (M) $H_2SO_4$ | HER | 126 | 83.9 | Present work |
| CuSe film | 1(M) KOH | OER | 270 | | [29] |
| Cu3P/CuO core/shell nanorod arrays | 1 (M) KOH | OER | 315 | | [33] |
| Cu2S branch arrays | 1 M KOH | OER | 284 | | [3] |
| CuO nanoparticles | 1 M NaOH | OER | 290 | | [35] |

information and knowledge to the scientific community interested in electrocatalytic water splitting. Fig. 1, 2, 4, 6–9, Tables 1–3.

## CRediT authorship contribution statement

**Mousumi Mondal:** Writing – original draft, Visualization, Software, Resources, Methodology, Formal analysis, Data curation, Conceptualization. **Sabyasachi Maity:** Methodology. **Anirban Ghosh:** Methodology. **Sujit Kumar Ghosh:** Supervision. **Swapan Kumar Bhattacharya:** Supervision.

## Declaration of competing interest

The authors declare that they have no known competing financial interestsor personal relationships that could have appeared to influence the work reported in this paper.

## Data availability

No data was used for the research described in the article.

## Acknowledgments

The authors gratefully acknowledge Jadavpur University for financial support, providing laboratory and other facilities. The authors wish to thank Prof. Arup Gayen, Jadavpur University for XRD analysis.

## References

[1] B. Chakraborty, R. Beltr-Suito, V. Hlukhyy, J. Schmidt, P.W. Menezes, M. Driess, Crystalline copper selenide as a reliable non-noble electro(pre)catalyst for overall water splitting, ChemSusChem 13 (2020) 3222–3229.

[2] W.Zhang G.Jia, G. Fan, Z. Li, D. Fu, W. Hao, C. Yuan, Z. Zou, Three-dimensional hierarchical architectures derived from surface-mounted metal e organic framework membranes for enhanced electrocatalysis, Angew. Chem. Int. Ed. 56 (2017) 13781–13785.

[3] T.N. Huan, G. Rousse, S. Zanna, I.T. Lucas, X. Xu, N. Menguy, V. Mougel, M. Fontecave, A dendritic nanostructured copper oxide electrocatalyst for the oxygen evolution reaction, Angew. Chem. Int. Ed. 56 (2017) 4792–4796.

[4] L. Bie, X. Luo, Q. He, D. He, Y. Liu, P. Jiang, Hierarchical Cu/Cu(OH)$_2$ nanorod arrays grown on electrode for enzyme-free glucose sensing, RSC Adv. 6 (2016) 95740–95746.

[5] M.D. Khan, M.A. Malik, N. Revaprasadu, Progress in selenium based metal-organic precursors for main group and transition metal selenide thin films and nanomaterials, Coord. Chem. Rev. 388 (2019) 24–47.

[6] R.A. Hussain, I. Hussain, Fabrication and applications of nickel selenide, J. Solid State Chem. 277 (2019) 316–328.

[7] R.A. Hussain, I. Hussain, Copper selenide thin films from growth to applications, Solid State Sci. 100 (2020) 106101.

[8] E. Andrade, V.M. Garci, P.K. Nair, M.T.S. Nair, E.P. Zavala, L. Huerta, M.F. Rocha, Ion beam analysis of copper selenide thin films prepared by chemical bath deposition, Nucl. Instrum. Methods Phys. Res. B 161–163 (2000) 635–640.

[9] V.M. Garci, P.K. Nair, M.T.S. Nair, Copper selenide thin films by chemical bath deposition, J. Cryst. Growth 203 (1999) 113–124.

[10] P. Chakadola, M.Prashanth W, Zheng Min, O. Steven, D. Matthias, In-situ formation of nanostructured core-shell Cu$_3$N-CuO to promote alkaline water electrolysis, ACS Energy Lett. 4 (2019) 747–754.

[11] D. Thanh, H. Tuan, T. Lam, L. Doan, N. Hoon, J. Hee, Pt nanodots monolayer modified mesoporous Cu@Cu$_x$O nanowires for improved overall water splitting reactivity, Nano Energy 59 (2019) 216–228.

[12] S. Zhao, J. Huang, Y. Liu, J. Shen, H. Wang, X. Yang, Y. Zhu, C. Li, Multimetallic NieMo/Cu nanowires as nonprecious and efficient full water splitting catalyst, J. Mater. Chem. A 5 (2017) 4207–4214.

[13] J. Theerthagiria, S.J. Leea, A.P. Murthy, J. Madhavanb, M.Y. Choia, Fundamental aspects and recent advances in transition metal nitrides as electrocatalysts for

hydrogen evolution reaction, A review, Curr. Opin. Solid State Mater. Sci. 24 (2020) 100805.
[14] Y. Yiseul, J. Theerthagiri, J. Seong, G. Muthusamy, M. Ashokkumar, Y.C. Myong, Integrated technique of pulsed laser irradiation and sonochemical processes for the production of highly surface-active NiPd spheres, Chem. Eng. J. 411 (2021) 128486.
[15] Y. Yiseul, J.L. Seong, J. Theerthagiri, S. Fonseca, L.M.C. Pinto, G. Maia, M.Y. Choi, Reconciling of experimental and theoretical insights on the electroactive behavior of C/Ni nanoparticles with AuPt alloys for hydrogen evolution efficiency and Non-enzymatic sensor, Chem. Eng. J. 435 (2022) 134790.
[16] S.N. Shreyanka, J. Theerthagiri, S.J. Lee, Yu. Yiseul, M.Y. Choi, Multiscale design of 3D metal–organic frameworks (M-BTC, M: cu, Co, Ni) via PLAL enabling bifunctional electrocatalysts for robust overall water splitting, Chem. Eng. J. 446 (2022) 137045.
[17] J. Theerthagiri, K. Karuppasamy, S.J. Lee, R. Shwetharani, H.S. Kim, S.K.K. Pasha, M. Ashokkumar, M.Y. Choi, Fundamentals and comprehensive insights on pulsed laser synthesis of advanced materials for diverse photo- and electrocatalytic applications Light, Sci. Appl. 11 (2022) 250.
[18] S. Chatterjee, S. Shaymal, M. Mukherjee, D. Halder, S. Chongdar, A. Paul, A. Bhaumik, Metal-Thiolate framework for electrochemical and photoelectrochemical hydrogen generation, ChemSusChem 15 (2022) e202200114.
[19] S. Zhao, J. Huang, Y. Liu, J. Shen, H. Wang, X. Yang, Y. Zhu, C. Li, Multimetallic NieMo/Cu nanowires as nonprecious and efficient full water splitting catalyst, J. Mater. Chem. A 5 (2017) 4207–4214.
[20] Y. Hou, M. Qiu, T. Zhang, X. Zhuang, C. Kim, C. Yuan, C. Ternary Yuan, Ternary porous cobalt phosphoselenide Nanosheets an efficient electrocatalyst for electrocatalytic and photoelectrochemical water splitting, Adv. Mater. 29 (2017) 1701589.
[21] K.K. Bera, M. Chakraborty, S.B. Chowdhury, A. Ray, S. Das, S.K. Bhattacharya, Significantly improved and synergistic effect of Pt-ZnO-Bi$_2$O$_3$ ternary hetero-junctions toward anode-catalytic oxidation of methanol in alkali, Electrochim. Acta 322 (2019) 134775.
[22] W. Shi, J. Lian, Facile synthesis of copper selenide with fluffy intersected-nanosheets decorating nanotubes structure for efficient oxygen evolution reaction international, J. Hydrogen Energy 44 (2019) 22983-22990.
[23] A. Sajeev, A.M. Paul, R. Nivetha, K. Gothandapani, T.S. Gopal, G. Jacob, M. Muthuramamoorty, S. Pandiaraj, A. Alodhayb, S.Y. Kim, Q.V. Le, P.L. Show, S.K. Jeong, A.N. Grace, Development of Cu$_3$N electrocatalyst for hydrogen evolution reaction in alkaline medium, Sci. Rep. 12 (2022) 2004.
[24] W. Shuting, Q. Kun, J. Zhao, C. Jiashu, W. Zheng, H. Chen, X. Cui, One-Step synthesis of a self-supported copper phosphide nanobush for overall water splitting, ACS Omega 1 (2016) 1367–1373.
[25] A. Radhakrishnan, B. Beena, Structural and optical absorption analysis of CuO nanoparticles, Indian J. Adv. Chem. Sci. 2 (2014) 158–161.
[26] S. Riyaz, A. Parveen, A. Azam, Microstructural and optical properties of CuS nanoparticles prepared by sol-gel route, Perspect. Sci. 8 (2016) 632–635.
[27] N.N. Krishnan, S. Vijayakumar, P. Gnanadurai, K.C.Preetha R.Shalini, Structural and optical characterization of copper selenide (Cu$_{2-x}$Se) nanoparticles, J. Nanosci. Techonol. 4 (2) (2018) 345–347.
[28] J. Masud, W.P.R. Liyanage, X. Cao, A. Saxena, M. Nath, Copper selenides as high-efficiency electrocatalysts for oxygen evolution reaction, ACS Appl. Energy Mater. 1 (2018) 4075–4083.
[29] R.A. Hussain, I. Hussain, Copper selenide thin films from growth to applications, Solid State Sci. 100 (2020) 106101.
[30] S.L. Goes, M.N. Mayer, J.E. Nutting, L.E. Hoober-Burkhardt, S.S. Stahl, M. Rafiee, Deriving the turnover frequency of aminoxyl-catalyzed alcohol oxidation by chronoamperometry, an introduction to organic electrocatalysis, Chem. Educ. 98 (2) (2021) 600–606.
[31] H. Rahaman, S. Kundu, S.K. Ghosh, Size-Selective silver-induced evolution of Mn$_3$O$_4$-Ag nanocomposites for effective ethanol sensing, Chem. Select 2 (2017) 6991–6999.
[32] C. Wei, Z.J. Xu, The comprehensive understanding of 10mA cm$^{-2}$ as an evolution parameter for electrochemical water splitting, Small Methods 2 (2018) 1800168.
[33] J. Du, F. Li, Y. Wang, Y. Zhu, L. Sun, Cu$_3$P/CuO coreshell nanorod arrays as high-performance electrocatalysts for water oxidation, ChemElectroChem 5 (2018) 2064-2068.
[34] A. Ghosh, S. Shyamal, A. Palui, R.N. Manna, S. Mondal, M. Jana, A. Ghosh, A. Bhaumik, Photoelectrochemical water oxidation over novel semiconducting zinc-based metal– thiolate framework, ACS Appl. Mater. Interfaces 14 (33) (2022) 37699-37708.
[35] S. Deng, Y. Shen, D. Xie, Y. Lu, X. Yu, L. Yang, X. Wang, X. Xia, J. Tu, Directional construction of Cu$_2$S branch arrays for advanced oxygen evolution reaction, J. Energy Chem 39 (2019) 61–67.

# List of publications:

1. Mousumi Mondal , Sabyasachi Maity , Anirban Ghosh , Sujit Kumar Ghosh , Swapan Kumar Bhattacharya ,* Superiority of CuSe as a non-nobel electrocatalyst among copper chalcogens for overall water splitting reactions Energy Nexus 14 (2024) 100289

2. Anirban Ghosh , Mousumi Mondal , Rabindra Nath Manna , Asim Bhaumik ,* Targeted synthesis of a metal-free thiadiazolate based nitrogen and sulfur rich porous organic polymer for an unprecedented hydrogen evolution in the electrochemical water splitting Journal of Colloid and Interface Science 658 (2024) 415–424.

3. Kamal Kanti Bera, Malay Chakraborty,Shyamal Kanti Bera, Anupam Chowdhury,Mahima Ranjan Das, Mousumi Mondal and Swapan Kumar Bhattacharya *Synergistic photo-enhanced electrocatalysis of Pt–ZnO–$Bi_2O_3$ heterojunction for methanol oxidation under visible light illumination,*Energy Adv., 2022,*1, 908.

4. Kamal Kanti Bera, Malay Chakraborty, Mousumi Mondal, SenjutiBanik,Swapan Kumar Bhattacharya∗Synthesis of α-β $Bi_2O_3$ heterojunction photocatalyst and evaluation of reaction mechanism for degradation of RhB dye under natural sunlight,Ceramics International 46 (2020) 7667–7680

5. Mousumi Mondal , Anirban Ghosh , Sujit Kumar Ghosh , Swapan Kumar Bhattacharya ,* Bifunctional catalysis on water splitting reaction by graphitic carbon supported NiO, NiS and NiSe nanoparticles(Communicated)